Hydromagnetic Transport of particles in viscous fluids

By

Muhammad Muddassar Maskeen

Reg No. 27-FBAS/PHDMA/S13

Department of Mathematics and Statistics
Faculty of Basic and Applied Sciences
International Islamic University, Islamabad
Pakistan
2020

Hydromagnetic Transport of particles in viscous fluids

By

Muhammad Muddassar Maskeen

Supervised by

Dr. Ahmed Zeeshan

Co-supervised by

Dr. Hafiz Obaid Ullah Mehmood

Department of Mathematics and Statistics
Faculty of Basic and Applied Sciences
International Islamic University, Islamabad
Pakistan
2020

Hydromagnetic Transport of particles in viscous fluids

By

Muhammad Muddassar Maskeen

A thesis

submitted in the partial fulfillment of the

requirements for the degree of

DOCTOR OF PHILOSOPHY

IN

MATHEMATICS

Supervised by

Dr. Ahmed Zeeshan

Co-supervised by

Dr. Hafiz Obaid Ullah Mehmood

Department of Mathematics and Statistics
Faculty of Basic and Applied Sciences
International Islamic University, Islamabad
Pakistan
2020

Dedication

This thesis is dedicated

to

My Respected Parents

My Teachers

My Family

My Wife

My Children.

Acknowledgements

My deepest gratitude goes to Allah almighty who has provided all that was needed to complete my doctorate. Throughout this entire study, He took care of everything that would have stopped me in my tracks and strengthened me even through my most difficult times. I offer salute to the Holy Prophet Hazrat Muhammad (S.A.W), who has lightened the life of all mankind with his guidance. He is a source of knowledge and blessings for the entire creations. His teachings make us to ponder and to explore this world with direction of Islam. There are a number of people who have helped me during the PhD. There is not enough space, nor time, to acknowledge everyone to the extent they deserve. I hope people understand the brevity of this part. First of all, I would like to thank my supervisor, **Dr. Ahmed Zeeshan**, for the privilege of starting my research career. It was a great pleasure to work and discuss with him. Thanks for supporting and encouraging me through these years. Secondly, I would like to express my deep appreciation to my co-supervisor, **Dr. Hafiz Obaid Ullah Mehmood**, for helpful discussions, valuable suggestions, and support during research work. I extend my gratitude to my respected teachers Dr. Nasir Ali, Dr. Tariq Javed, Prof. Dr. Muhammad Sajid T.I, Dr. Ahmer Mehmood, Dr. Rahmat Ellahi, and Mr. Niaz Ahmed for encouragement and support. I am also thankful to my friends Dr. Nasir Shahzad, Dr. Mohsan Hassan, Dr. Khurram Javed, Dr. Afzaal Ali, Dr. Aqib Majeed, Dr. Nouman Ejaz, Muhammad Shahid Nadeem, Muhammad Bilal Arain, Amad-ur-Rehman, Zeeshan Pervaiz, Dr. Muhammad Usman, Engr. Nouman Riaz, Prof. Awais Latif, Engr. Waqas Hassan, Nasir Islam, Mudasir Ijaz, Qaiser Nazir, Atif Asghar, Engr. Tahir Javed, Raja Nasir Ali, Syed Nazim Abbas, Sohail Akhtar, and others who always helped me during my studies in all respects. My utmost regard also goes to my parents, who painstakingly laid the foundation for my education giving it all it takes. I will forever be grateful to my loving wife who has given everything possible and even given up important things to make sure i achieve this feat. I can’t find the words that express my gratitude. I also from the depth of my heart appreciate my children who even at such tender ages have had to endure so much stress and discomfort just for me. This page can’t tell it all.

Muhammad Muddassar Maskeen

Preface

Since the beginning of history, humans have applied the knowledge of each era to discover new worlds, and in turn explorations have contributed to the development of science, helping us to understand nature and to develop new technologies. Modern advancements in nanotechnology have led to the development of a new innovative class of heat transfer fluids called "Nanofluids" formed by dispersing nanoparticles (1-100nm) in base fluids. The materials which are usually used as nanoparticles comprise chemically stable metals, metal oxides, oxide ceramics, metal carbides, metal nitrides, carbon in various forms. The novel and modern concept of nanofluids offers fascinating heat transfer features as compared to conventional heat transfer fluids like oil, water, ethylene glycol etc. There are significant studies on the enhanced heat transfer properties of nanofluids specifically on thermal conductivity and convective heat transfer. Nanofluids have a wide range of engineering and industrial applications because nanofluids possess enhanced thermophysical properties like thermal conductivity, thermal diffusivity, viscosity and convective heat transfer. Nanofluids can be used for cooling of automobile engines, welding equipment, high power microwave tubes and high power laser diode arrays. Also, nanofluids have extensive applications in industries, ranging from transportation to energy production and in electronics systems like microprocessors, Micro-Electro-Mechanical Systems and in the field of biotechnology. Recently, nanofluids gained increasing response from engineers and researchers due to the potential of nanofluid technology and their focus on specific industrial applications.

Multiphase flow is the simultaneous flow of numerous phases. The research of multiphase flow is very essential in energy related industries and applications. The very basic case of multiphase flow is two-phase flow. It can be categorized into solid-liquid, liquid-liquid, gas-solid and gas-liquid flows. Examples of solid-liquid flow include flow of corpuscles in the plasma, flow of mud, flow of liquid with suspended solids like slurries, motion of liquid in aquifers. The flow of two immiscible liquids like oil and water, which is very important in oil recovery processes, is an example of liquid-liquid flow. The injection of water into the oil flowing in the pipeline reduces the resistance to flow and the pressure gradient. Thus, there is no need for large pumping units. Immiscible liquid-liquid flow has other industrial applications such as

dispersive flows, liquid extraction processes, and co-extrusion flows. Examples of gas-solid flow include fluidized bed, and transport of powdered cement, grains, metal powders, ores, coal, and so on using pneumatic conveying.

The title of current dissertation is **"Hydromagnetic Transport of particles in viscous fluids".** This dissertation is focused on the transport of single material nanoparticles, hybrid nanoparticles and solid particles in viscous fluids. For mathematical formulation of nanofluids Buongiorno's model, Tiwari-Das model and two fluid models have been incorporated. Flow is considered through several realistic configurations namely: the stretching cylinder, concentric cylinders and inclined plane under the impact of magnetic field. Boundary conditions exert a set of additional constraints to the flow problem on specified boundaries particularly isothermal, Convective surface and prescribed heat and mass flux boundary conditions. Several flow and heat transfer characteristics like thermal radiation, viscous dissipation, joule heating, and porosity are considered. Runge-Kutta-Fehlberg fourth-fifth order (RKF45) numerical scheme along with shooting algorithm and "Bvph 2.0" homotopy based Mathematica package are employed to solve system of non-linear ordinary differential equations. Results are illustrated for sundry parameters like magnetic parameter, radiation parameter, Electric parameter, Biot number, Prandtl number, Eckert number, convection parameter, curvature parameter, chemical dimension, fractal dimension, radius of gyration, porosity parameter, local inertia coefficient, thermophoretic parameter, Brownian motion parameter, Schmidt parameter, chemical reaction parameter, activation energy parameter, Casson fluid parameter, and volume fraction of nanoparticle via graphs and in tabular form.

The current thesis has been organized into ten chapters.

Chapter 1 discusses research background, motivation, objectives, outlines, and methodology. Chapter 2 is concern about literature review, governing equations and important terminologies. Chapter 3 focuses on the impact of thermal radiation and convective heating on hydromagnetic transport of Alumina nanoparticles in ethylene glycol base fluid. This study is published in **Advances in Mechanical Engineering,** 9 (2017) 1-8. Chapter 4 examines the convective-radiative heat transfer and flow analysis of hydromagnetic copper-alumina/water hybrid nanofluid flow with joule heating and viscous dissipations. This study is published in **Journal of Thermal**

Analysis and Calorimetry, 138 (2019) 1127–36. Chapter 5 investigates the flow of iron nanoparticles aggregation in water base fluid. The influences of mixed convection and Joule heating are also account for. This analysis is published in the **Indian Journal of Physics,** 93 (2019) 53-59. Chapter 6 focuses on nanofluid flow past a stretching cylinder embedded in non-Darcian Forchheimer porous media. This study is published in **Neural Computing and Applications,** 30 (2018) 3479-89. Chapter 7 investigates the influence of chemical reaction and Arrhenius activation energy on hydromagnetic Non-Newtonian nanofluid. This study is submitted in well-known **HEC recognized journal** for possible publication. Chapter 8 converses the hydromagnetic solid-liquid pulsatile flow through annulus in a porous media. This research is published in the **Journal of Visualization,** 21 (2018) 407-19. Chapter 9 examines the impact of thermal radiation and MHD on boundary layer dusty gas flow. This research is published in **Results in Physics,** 7 (2017) 1932-39. Chapter 10 provides the chapter wise conclusion of research performed throughout this thesis.

Contents

List of Symbols

English Symbols

A	A constant having unit of pressure gradient	k_r^2	Binary Chemical reaction
E_a	Arrhenius activation energy	h_s	Mass transfer coefficient
e	Aspect ratio of ellipsoid	h_f	Heat transfer coefficient
x, r	Axial and radial coordinates	Q_m	Mass flux
D_B	Brownian coefficient	N_c	Number of backbone's particles
Nb	Brownian motion parameter	N_{int}	Number of cluster's particles
l	Characteristics length	u , v	Velocity components
a	Characteristics radius	Nu	Nusselt number
d_l	Chemical dimensions	r_p	Particle radius
p^*	Cluster spanning chain ratio	N	Particles number density
f	Dimensionless stream function	k_1	Permeability of porous medium
f'	Dimensionless velocity	K^*	Porosity parameter
Ec	Eckert number	Pr	Prandtl number
c_p	Effective heat capacity	p	Pressure
E_1	Electrical field parameter	Rd	Radiation parameter
E_0	Electrical field strength	Q_r	Radiative heat flux
n	Fitted rate constant	E_A	Activation energy parameter
R	Fluid particle interaction parameter	Bj	Diffusion Biot number
T	Fluid temperature	a^*	Radius of primary particle
d_f	Fractal dimensions	Re	Reynolds number
M_{11}, M_{33}	Geometrical factors	Sc	Schmidt parameter
Gr	Grashof number	Sh	Sherwood number
g	Gravitational acceleration	C_f	Skin friction coefficient
R_g	Gyration radius	c	Stretching rate
Q_w	Heat flux at wall	D_T	Thermophoretic coefficient
Q_0	Heat Sink	Nt	Thermophoretic parameter
A_k	Kapitza radius	C	Nanoparticles concentration
S	Stokes Drag coefficient	r^*	Nanoparticles ratio
Bi	Thermal Biot number		

Greek Symbols

χ	Aspect ratio
κ	Boltzman constant
β_2	Casson fluid parameter
β_3	Chemical reaction parameter
γ	Curvature parameter
ρ	Density
ε	Dimensionless small quantity
θ	Dimensionless temperature
$\tilde{\alpha}$	Dust parameter
μ	Dynamic viscosity
ω	Frequency of oscillation
β_1	Frequency parameter
ψ	Inclination of magnetic field
υ	Kinematic viscosity
σ	Magnetic permeability
λ	Mixed convection parameter
ϕ	Nanoparticles volume fraction
α	Plane inclination
ϑ	Ratio of densities of particle to fluid
δ	Ratio of specific heat of particle to fluid
τ	Shear stress
η,ξ	Similarity variables
σ^*	Stefan Boltzman constant
α^*	Suction parameter
$\hat{\delta}$	Temperature difference parameter
$\overline{\alpha}$	Thermal diffusivity
τ_T	Thermal equilibrium time
β	Thermal expansion coefficient
τ_v	Velocity relaxation time
$\tilde{\tau}$	Ratio of heat capacities of fluid to particle

Subscript Symbols

a	Aggregation
∞	Ambient
c	Backbone particles
f	Base fluid
int	Cluster
nc	Dead ends particles
1	First unsteady part
hnf	Hybrid Nanofluid
max	Maximum
nf	Nanofluid
p	Nanoparticles
2	Second unsteady part
0	Steady part
w	Wall

Chapter 1

Introduction

1.1 Research Background

In an enormous array of circumstances in nature and industry, fluid transports particulate materials. The transport phenomenon of particles through fluid flows has, from the historic times, been the object of scientific, engineering and industrial importance due to its widespread applications. In some conditions, these particles are purely carried by the flow: they follow the fluid elements. For instance, the uniform distribution of nanosize particle in pure fluid has the same motion as like the fluid particles while analyzing nanofluid. Choi [1] was the founder who gave the clue of nanofluids. These fluids consist of nanometer sized particles (1-100 nm) dispersed in carrier fluid. Nanoparticles are normally made of metal oxides, metals, metal carbides, metal nitrides or non-metals (Carbon nanotubes, graphite). While the conventional fluid is commonly a conducting fluid like water, engine oil, ethylene glycol and kerosene oil. There are two approaches in literature to investigate the transport of nanoparticles within fluid; namely, Tiwari and Das [2] model in which thermophysical characteristics of conventional fluid are improved within the correlation of effective viscosity and thermal conductivity. Second one is Buongiorno's model [3], in which the transport of nanoparticles is determined by solving the coupled momentum and concentration equations. Nanofluids have widespread technical, engineering, scientific and industrial applications in the fields of paper production, spinning of fibers, domestic refrigerator, cooling, cancer therapy, polymer industry, solar water heater and magnetic cell separation etc. Various experimental and theoretical explorations have been reported to nanofluids and many references within [4-7].

The nanofluid flow becomes more complex when one considers more than one distinct nanoparticles. This category of working heat transfer fluids is termed as Hybrid nanofluid. The hybrid nanomaterials are mainly classified in the following three types [8]:

(i) Metal Nanomaterials
(Al_2O_3/Ni, Mg/CNT, MgO/Fe, Al_2O_3/Fe, Al_2O_3/Cr, and Al_2O_3/Cu).

(ii) Ceramic Nanomaterials
(Al_2O_3/TiO_2, SiO_2/Al_2O_3, CNT/Fe_3O_4, SiO_2/Ni and Al_2O_3/SiC).

(iii) Polymer Nanomaterials
(Polymer/CNT, thermoplastic/layered silicates polymer, polymer/hydroxides and polyester/TiO_2).

Suresh et al. [9] manufactured copper-alumina nanocomposites powder by employing thermochemical method and then prepared copper-alumina/water hybrid nanofluid by two step method. The obtained results illustrate that there is significant improvement in thermal conductivity of hybrid nanofluid as compared to deionized water. Also, viscosity measurements indicate that copper-alumina/water hybrid nanofluid work as Newtonian fluid and the viscosity of hybrid fluid is higher as compare to alumina/water nanofluid. Further, Suresh et al. [10 and 11] studied the heat transfer and pressure drop features of copper-alumina/water hybrid nanofluid. Some very recent theoretical and experimental investigations have been reported related to hybrid nanofluids [12-18].

The transport characteristics of nanofluid have also been significantly influenced by the aggregations of nanoparticles. Aggregation occurs when two or more particles collide and adhere. Gregory [19] reflected the mechanism of particle aggregation and forms of collides along with the aggregation procedure in detail. It is well established that aggregates can be taken as fractal objects (Meakin [20], Jullien and Botet [21]). According to fractal morphology of aggregates in colloids, a fractal aggregate is inserted within sphere and is comprised of few approximately linear chains, which span the complete aggregate and side chains. The momentous role of backbone in the rheology of colloids is because of its configuration which can transfer elastic forces between aggregates.

Water and air comprises impurities like dust particles and foreign bodies. In this case, the particles do not follow the flow and have their own, complex dynamics. A number of factors like density differences between the particles and the carrier fluid, particle size, shape, intrinsic particle activity are responsible to this situation. In last few decades, the topic of hydromagnetic two phase flows has achieved considerable response of researchers and scientists because of its widespread

applications in technical and manufacturing fields. For examples the entertainment of particles in dust bursts, solid rocket exhaust nozzles, crystal growth, fluidized beds, ablation cooling, conveying of powdered materials, nuclear reactors with solid-gas feeds, petroleum industry, refinement of crude oil in the fields, granular materials transport in pipes, aircraft and turbine machines operation, movement of gas-particle mixtures in power generators and erosion of soil etc. Saffman [22] was a pioneer by proposing a mathematical model for particle-gas flow in 1962. Marble [23] extended the pioneering work, which considered the dynamics of gas encompassing dust particles. It is examined that for gas-particle flow, the particles cloud was established by four similarity parameters, each has simple physical consequence.

Michael and Miller [24] used previous formulation and offered solutions for two diverse cases on the motion of dusty gas. The two cases of induced motion in the dusty gas are considered when plane moves parallel to it, first is simple harmonic motion and second is impulsive motion from rest with uniform velocity. In first case the variations in phase velocity and the decay of oscillatory waves are noticed as functions of the mass concentration of dust. In second case some velocity distributions are calculated and shown that the shear layer thickness is decreased at large times. In another study Michael and Norey [25] presented the solutions for problem of dusty gas confined between two concentric cylinders which initiate rotation impulsively from rest. They supposed that relaxation time of dust particles is small and results are achieved by taking ratio of time scale. Rao [26] investigated the laminar flow of an unsteady viscous fluid with uniform dispersion of dust particles under the impact of exponential varying pressure gradient. They found that both the fluid and dust particles near to cylinder axis move with larger velocity but velocity of dust particles is higher than fluid. If the masses of dust particles are small, their influence on the fluid flow is reduced.

Numerous efforts related to particle suspension flows have been reported in last few decades. Prominent contribution is due to the studies [27-31] on the steady two-phase suspension flow. This type of fluid-particle flows are rather challenging to investigate as system of partial differential equations needs to tackle simultaneously. To overcome this challenge, some author’s employed the Blasius series expansion, momentum integral method and finite-difference method to obtain approximate

solutions. Recently, Kumar and Sarma [32] investigated the fluid-particle suspension flow due to stretching sheet.

In recent years, there have been several studies in which magnetic field plays a key role and have attracted the response of scientists and engineers because of its abundant applications in many fields like petroleum industries, crystal growth, liquid-metal cooling of nuclear reactors, magnetic behaviour of plasmas in fusion reactors, electromagnetic casting, boundary layer control in aerodynamics, ship propulsion, jet printers, etc. A magnetic field is strongly linked to the understanding of physical properties which take place in magnetohydrodynamic. Also, the magnetic field is extensively related with the flow, heat and mass transfer features during several physical situations.

1.2 Research Motivation and Objectives

Motivated by aforementioned studies, the extant research is concerned about hydromagnetic transport of particles in viscous fluids. The major portion of thesis emphasizes on the hydromagnetic transport of particles (nanoparticles or solid particles) dispersed in carrier fluid. Flow through various non-uniform configurations namely: stretching cylinder, concentric cylinders and inclined plane have been considered in the current research. Further, the influences of thermal radiation, mixed convection, joule heating, viscous dissipation, pulsatile pressure gradient, convective heating, electric field, chemical reaction and Arrhenius activation energy are given due attention. To have a better insight of the fluid particle suspensions, as suggested by the literature, Tiwari and Das model [2], Buongiorno's model [3] and two fluid model have been utilized in the present research.

Keeping in mind the aforementioned facts, the current thesis aims:

- To examine the impact of thermal radiation, convective heating and non-uniform electric field on hydromagnetic transport of Alumina nanoparticles suspended in ethylene glycol base fluid.
- To investigate convective-radiative flow of hydromagnetic copper-alumina/water hybrid nanofluid under influences of joule heating and viscous dissipation.
- To explore the flow of iron nanoparticles aggregation suspended in water base fluid under the impact of transverse magnetic field, mixed convection and Joule heating.

- To analyze the MHD nanofluid flow in non-Darcy Forchheimer porous medium along with the prescribed heat and mass flux conditions.
- To examine hydromagnetic non-Newtonian nanofluid flow along with influences of chemical reaction, Arrhenius activation energy and convective boundary conditions.
- To analyzed hydromagnetic solid-liquid pulsatile flow through concentric cylinders embedded in porous media along with the influence of joule heating.
- To inspect the boundary layer dusty gas flow over an inclined plane under the impact of thermal radiation, MHD and viscous dissipation.

The present research has immense applications in several industrial, scientific and engineering regimes. Mathematical models formulated and results obtained for significant flow characteristics provide a bench mark for the validation of classical and experimental studies in the future research. Further this research brings a novel contribution in the literature for the researchers working in this area.

1.3 Research Methodology

The higher order nonlinear coupled differential equations associated with nonlinear boundary conditions are tough to attempt by an exact or may be semi analytical solution techniques that's why few numerical methods are necessary to be developed, nevertheless the significance of analytical and semi analytical solutions are still very essential because they offer a standard for testing the precision of approximate solutions. There are so many numerical and analytical techniques available in the literature. Two of them are utilized in current research, which is discussed as follows:

1.3.1 Runge-Kutta-Fehlberg Method (RKF45)

For better precision in solution process of an initial value problem, one have to tackle the problem twice by taking step sizes of h and $h/2$ and match the results at mesh points equivalent to greater step size. But it needs large number of of calculations for the lesser step size and requisite to be reiterated if these are not in good agreement. One way to overcome this situation is the Runge-Kutta-Fehlberg method [33-34]. If the suitable step size h is being taken then this technique can determine. Each step needs the six values given as follows:

$$w_1 = hf\left(t_n, y_n\right), \tag{1.1}$$

$$w_2 = hf\left(t_n + \frac{1}{4}h, y_n + \frac{1}{4}w_1\right), \tag{1.2}$$

$$w_3 = hf\left(t_n + \frac{3}{8}h, y_n + \frac{3}{32}w_1 + \frac{9}{32}w_2\right), \tag{1.3}$$

$$w_4 = hf\left(t_n + \frac{12}{13}h, y_n + \frac{1932}{2197}w_1 - \frac{7200}{2197}w_2 + \frac{7296}{2197}w_3\right), \tag{1.4}$$

$$w_5 = hf\left(t_n + h, y_n + \frac{439}{216}w_1 - 8w_2 + \frac{3860}{513}w_3 - \frac{845}{4104}w_4\right), \tag{1.5}$$

$$w_6 = hf\left(t_n + \frac{1}{2}h, y_n + \frac{8}{27}w_1 + 2w_2 - \frac{3544}{2565}w_3 + \frac{1859}{4104}w_4 - \frac{11}{40}w_5\right). \tag{1.6}$$

The solution of an IVP can be approximated by Runge-Kutta method of fourth order:

$$y_{n+1} = y_n + \frac{25}{216}w_1 + \frac{1408}{2565}w_3 + \frac{2197}{4101}w_4 - \frac{1}{5}w_5. \tag{1.7}$$

Here the values w_1, w_3, w_4, w_5 are used and w_2 is not utilized. An improved solution can be approximated by using RK method of fifth order:

$$z_{n+1} = z_n + \frac{16}{135}w_1 + \frac{6665}{12825}w_3 + \frac{28561}{56430}w_4 - \frac{9}{50}w_5 + \frac{2}{55}w_6. \tag{1.8}$$

We choose $\Delta\eta = 0.001$ as step size and 10^{-6} as the convergence criterion conditions. Two diverse estimations for solution are evaluated and matched at each step. If these calculations are in good agreement, then they are accepted. If two calculations are not in good agreement up to the required precision, then step size will be minimized. If calculations are match to further significant digits as requisite, then the step size will be enlarged. When we incorporate the algorithm in computing software, it will amend the missing initial derivative until convergence is succeeded. The current technique is well-known because of high accuracy and robustness. We can calculate the optimal step size by multiplying the current step size by scalar s^*. The formula for s^* is given as follows:

$$s^* = \left(\frac{tolh}{2\left|z_{n+1} - y_{n+1}\right|}\right)^{\frac{1}{4}} \approx 0.84\left(\frac{tolh}{\left|z_{n+1} - y_{n+1}\right|}\right)^{\frac{1}{4}}. \tag{1.9}$$

1.3.2 Bvph 2.0 Package

Liao [35] was the pioneer who contributed the idea of homotopy [36] to acquire analytic approximations of nonlinear differential equations $N\left[u(\mathbf{r})\right]=0$ by constructing one-parameter family of equations (called the zeroth-order deformation):

$$(1-w)\pounds\left[\Omega(\mathbf{r};w)-u_0(\mathbf{r})\right]=wN\left[\Omega(\mathbf{r};w)\right], \tag{1.10}$$

Here $u(\mathbf{r})$ is function of independent variable $\mathbf{r}=\{r_1,r_2,r_3,...,r_n\}$, $u_0(\mathbf{r})$ is an initial guess, $w\in[0,1]$ the embedding parameter, N is non-linear differential operator and $\pounds$ is auxiliary linear operator. Taylor series of $\Omega(\mathbf{r};w)$ w.r.t the embedding parameter w may be expressed as:

$$\Omega(\mathbf{r};w)=u_o(\mathbf{r})+\sum_{l=1}^{\infty}u_l(\mathbf{r})w^l, \tag{1.11}$$

here

$$u_l(\mathbf{r})=\frac{1}{l!}\frac{\partial^l\Omega(\mathbf{r};w)}{\partial w^l}\bigg|_{w=0}. \tag{1.12}$$

The liability in above scheme is that the Taylor series could be diverged at $w=1$. To resolve this issue, Liao [37] introduced a nonzero auxiliary parameter $\hbar$, which is now termed as convergence-control parameter.

$$(1-w)\pounds\left[\Omega(\mathbf{r};w)-u_0(\mathbf{r})\right]=w\hbar N\left[\Omega(\mathbf{r};w)\right]. \tag{1.13}$$

Note the solution $\Omega(\mathbf{r};w)$ of Eq. (1.13) depends on the embedding parameter w and convergence-control parameter $\hbar$. In Eq. (1.12) the term $u_l(\mathbf{r})$ also depends on $\hbar$ and therefore the convergence region for Taylor series defined in Eq. (1.11) is influenced by $\hbar$. Thus, the auxiliary parameter $\hbar$ offers an appropriate mode to confirm the convergence of Taylor series Eq. (1.11) at $w=1$. For $w=0$ and $w=1$, we have

$$\Omega(\mathbf{r};0)=u_o(\mathbf{r}),\ \Omega(\mathbf{r};1)=u(\mathbf{r}), \tag{1.14}$$

where $u(\mathbf{r})$ signifies the solution of differential equation and we can express it as:

$$u(\mathbf{r}) = u_o(\mathbf{r}) + \sum_{l=1}^{\infty} u_l(\mathbf{r}). \tag{1.15}$$

Further in 2013, Liao [38] established a HAM based Mathematica package "Bvph 2.0" that can easily handle systems of non-linear ordinary differential equations. It can tackle several categories of ordinary differential equations systems like coupled in finite interval, coupled in semi-infinite interval, with an unknown parameter to be found, and coupled along with algebraic property at infinity. For ease, this package prerequisites to put all governing differential equations, appropriate initial guesses, boundary conditions and auxiliary linear operators for under investigation problems. To run this package, requires defining of all inputs accurately excluding the convergence-control parameters. We can achieve ideal convergence-control parameters by reducing squared residual error. For accuracy, results of some problems solved by this package may be compared to analytical and numerical methods.

1.4 Thesis Outlines

The present thesis comprises of ten chapters starting from this preliminary chapter, which addresses the research background, motivation, objectives, thesis outlines and research methodology. Further, chapter 2 presents a detailed literature review, governing equations and dimensionless numbers related to problems studied in this dissertation. These problems are investigated and presented in next seven chapters (chapter 3 to 9). Chapter 10 provides the comprehensive chapter wise conclusion of entire research performed in the thesis.

Chapter 3 studies electromagnetohydrodynamic transport of Al_2O_3 nanoparticles in ethylene glycol base fluid over convectively heated stretching cylinder. The influences of sundry parameters like magnetic parameter, electric field parameter, radiation parameter and Biot number have been analyzed on flow and thermal profiles through graphs.

Chapter 4 investigates enhancement in heat transfer of hydromagnetic alumina-copper/water hybrid nanofluid flow past over stretching cylinder. The sundry parameters have an influence on velocity, temperature, thermophysical properties, skin friction coefficient and heat transfer rate. The results are presented via graphs and tables. A comparative analysis of hybrid nanofluid versus single material nanofluid is also made and observed that hybrid nanofluid have greater ability of enhancement of

thermal conductivity and heat transfer characteristics in comparison with carrier fluid and nanofluid.

Chapter 5 explores the hydromagnetic transport of iron nanoparticles aggregates dispersed in water base fluid. The impact of emerging parameters like chemical dimension, fractal dimension and radius of gyration on flow and temperature distributions are reflected through graphs and discussed in details. The correlations for Nusselt number and skin friction coefficient for nanoparticles concentration are calculated numerically and displayed in tabular form.

Chapter 6 analyzes the hydromagnetic nanofluid flow past a stretching cylinder embedded in non-Darcy Forchheimer porous media. The impact of numerous emerging parameters on the flow distribution, thermal distribution, concentration distribution, heat transfer rate, Sherwood number and skin friction coefficient are presented via graphs and tables.

Chapter 7 investigated the hydromagnetic transport of non-Newtonian nanofluid over permeable stretching cylinder along with binary chemical reaction and Arrhenius activation energy using convective boundary conditions. The influences of magnetic parameter, Casson fluid parameter, chemical reaction parameter, activation energy parameter and suction parameter on the velocity, temperature and concentration profiles are reflected via graphs. Numerical values of skin friction coefficient, Nusselt number and Sherwood number are estimated and depicted in tabular form.

Chapter 8 examines the hydromagnetic solid-liquid pulsatile flow through concentric cylinders in porous medium with the influence of joule heating. The influence of magnetic and porosity parameters on velocity and temperature distribution are displayed graphically and briefly nattered.

Chapter 9 emphasizes the hydromagnetic transport of dust particles in gas flow over an inclined plane by incorporating the thermal radiation impact. The influences of magnetic parameter, thermal radiation parameter and gas-particle interaction parameter on flow and temperature distributions of both phases are depicted graphically.

Chapter 10 demonstrates the comprehensive chapter wise conclusion of entire research executed in the thesis.

Chapter 2

Literature Review and Governing Equations

The current chapter provides a comprehensive literature review, basic governing laws and their corresponding governing equations, dimensionless entities and some basic terminologies pertaining to the flow problems investigated in this research.

2.1 Literature Review

The detailed literature review relating to the flow problems studied in this thesis is presented in this section. Further, this section is divided into two sub sections namely nanofluid flows and particulate flows.

2.1.1 Nanofluid Flows

Scientists have been quite active in the search of novel approaches to increase heat dissipation of various cooling devices. The energy proficient heat transfer fluids are essential for high performance cooling, but low thermal conductivity of ordinary liquids is the main issue. This concern can be fixed through the inclusion of solid nanoparticles into ordinary base liquids. Immersion of metal particles in conventional fluid significantly improves the thermal performance of these fluids. Nanofluids have widespread cooling applications like electronic cooling, transformer cooling, lubrication, vehicle cooling and many others. Further the magneto nanofluids are very suitable in the medical applications like safer surgery, cancer therapy, wound treatments, etc. It is well established fact that nanofluids thermal conductivity is extensively greater than corresponding conventional fluids [39-40]. Numerous parameters like particle shape, particle size, volume fraction, PH, aggregation and thermal properties of particles and fluid are liable for thermal conductivity enhancement. In spite of the unique features and prospective of nanofluids, these quite special fluids are still at their early phases and a significant amount of research remains to be explored. Numerous theoretical and experimental investigations are reported to nanofluids and many references within [41-45].

Turkyilmazoglu [46] studies the nanofluid flow due to rotating disk. In this research water-based nanofluids comprising volume fraction of (Al_2O_3, Ag, Cu,

CuO, TiO_2) nanoparticles are examined. The comparative analysis depicts that boundary layer thickness of flow over rotating disk can be reduced by the addition of nanoparticles Cu, CuO and Ag, but it grows in case of Al_2O_3 and TiO_2. The maximum and minimum values of shear stress occur for Ag and Al_2O_3 respectively. An increase in nanoparticles volume fraction leads to more heat generation and hence enhances the thermal layer thickness. The nanofluid comprising copper nanoparticles has greatest heat transfer rate, but TiO_2 nanoparticles have lowest heat transfer rate. Sheikholeslami et al. [47] inspected impact of magnetic field on copper water nanofluid by applying control volume finite element method. There finding shows that heat transfer rate is an increasing function of nanoparticle volume fraction, inclination angle and Rayleigh number but decreasing function of Hartmann number. Mabood et al. [48] investigated numerical analysis of hydromagnetic boundary layer flow and heat transfer because of nonlinear stretching sheet. They establish that by enhancing magnetic parameter the Sherwood number and Nusselt number declines, whereas the coefficient of skin friction enhances.

Rashidi et al. [49] focused on hydromagnetic nanofluid flow over rotating disk in porous media for three varieties of nanoparticles Cu, CuO, Al_2O_3. Hussain et al. [50] explored the problem of hydromagnetic third grade nanofluid flow with the influences of thermal radiation and viscous dissipation. Their results illustrate that the temperature field and thermal boundary layer thickness are enhanced by increasing thermal radiation parameter and Eckert number. They also noted that the temperature increases quickly for enhancing thermal radiation parameter as compare to Eckert number. Also, the temperature is enhanced by up-surging Brownian motion parameter but the nanoparticles concentration is reduced. Makinde and Aziz [51] investigated the boundary layer nanofluid past a stretching sheet with convective heating boundary condition. By fixing other parameters, the local concentration of nanoparticles enhances by enhancing Biot number, whereas the reverse trend can be seen verses increasing Lewis number. Mustafa et al. [52] examined the heat transfer of nanofluid flow over an exponentially stretched surface with convective heating boundary conditions. They observed that by increasing Brownian motion and thermophoretic parameters the temperature distribution enhances while the thermal boundary layer decreases.

Transport phenomenon in porous medium arises in several fields of science, technology and engineering having widespread applications in diverse fields. In the

last several years both theoretical and experimental investigations on fluid flow in porous medium has been investigated. Porous media flow generally involves three scales: the pore scale, the domain scale, and the descriptive elementary volume scale. In the classical studies, porous media flow is modeled by some semi empirical models, due to complex structure of porous medium based on volume averaging at the representative elementary volume scale. Various famous models have been communicated in literature like Darcy, Forchheimer-extended Darcy model and Brinkman-extended Darcy. Non-Darcy influence on natural convection in porous media has gained vital response as a consequence of experiments performed with various combinations of solids and fluids [53-55].

Very recent, nanofluid flow due to porous media (Non-Darcy/Darcy) has grabbed the response of researchers, scientists and engineers. Numerous researchers have worked related to this topic and many references therein [56-62]. Rashidi et al. [63] performed entropy generation analysis of hydromagnetic nanofluid flow due to porous rotating disk. Umavathi et al. [64] examined nanofluid through a vertical rectangular duct packed in porous matrix. They employed Darcy-Forchheimer-Brinkman model to represent the fluid transportation through the porous medium. A mathematical model describing unsteady hydromagnetic mixed convection boundary layer nanofluid flow over an exponential stretching sheet entrenched in an isotropic, homogenous porous media was developed by Beg et al. [65]. The obtained result shows that nanofluid temperature and thermal boundary layer thickness are raised with raising thermophoretic, Brownian parameter and viscosity ratio parameter, whereas the reverse trend is observed by increasing Prandtl number. Ibanez et al. [66] studied flow of nanofluid in porous micro-channel with collective influence of magnetic field and convective boundary condition on thermal boundary layer and global entropy generation. Ellahi et al. [67] performed analysis of MHD flows of third order fluid in saturated porous space. Shirvan et al. [68] discussed numerical simulation and sensitivity analysis of turbulent fluid flow in double pipe heat exchanger embedded in porous media.

When two or more diverse categories of nanoparticles are distributed in conventional fluid then this type of nanofluid is entitled as ‘‘Hybrid Nanofluid”. The word hybrid can be considered as merging of two or more dissimilar nanoparticles (size less than 100nm). The main reason of merging nanomaterial in carrier fluid is

the enhancements of thermal conductivity in carrier fluids. The principle perspective of employing hybrid nanofluid is the choice of proper combination of nanoparticles, positive features can be enhanced and problems can be resolved. This new kind of nanofluids has various reliable applications e.g. lubrication, micro fluidics, manufacturing, transportation, medical, defense, naval structures and generator cooling etc. When nanosize particles are distributed properly, hybrid nanoparticles offer incredible benefits having extraordinary high effective thermal conductivity.

Recently, various experimental and numerical works are published relating to hybrid nanofluid. Momin [69] achieved an experimental research on mixed convection copper-alumina/water hybrid nanofluid flow over an inclined tube. They perceived that dilute alumina–copper/water hybrid nanofluid of 0.1% volume fraction exhibit slightly higher friction factor as equated to clean water. The average rise in friction factor of 0.1% alumina–copper/water hybrid nanofluids is 16.97% as equated to water. Which exposes that dilute alumina–copper/water hybrid nanofluids will cause additional drawback in pumping power as equated to alumina/water nanofluid. Askari et al. [70] have done an experimental investigation of Fe_3O_4/Graphene hybrid nanofluid heat transfer features. The key outcomes indicate that thermal conductivity is enhanced by 14% to 32% for a mass fraction of 1% for Fe_3O_4/Graphene nanofluid at 20 to 40°C. Furthermore, an enhancement of 8.5% and 14.5% in heat transfer coefficient were observed in comparison to conventional fluid, for Fe_3O_4 and Fe_3O_4/Graphene nanofluids at Reynolds number of 4248. It is concluded from all these results that stable and cost effective Fe_3O_4/Graphene nanofluid have very promising heat transfer applications. Mehryan et al. [71] examined free convection of copper-alumina/water hybrid nanofluid flow through differentially heated porous cavity. They incorporated two kinds of porous media, aluminum metal foam and glass ball for the porous matrix. In case of aluminum foam (high thermal conductivity), Nusselt number is independent of porosity, whereas in case of glass balls (low thermal conductivity), the Nusselt number is dependent on porosity. The heat transfer rate reduces very rapid for hybrid nanofluid as compared to a single material nanofluid.

Shahsavar et al. [72] reported the concept of heat transfer and entropy generation optimization for CNT-Fe_3O_4/water non-Newtonian hybrid nanofluid flow through an annulus region. They found that by enhancing CNT concentration from

0.1% to 1.1% at 0.9% fixed concentration of Fe_3O_4 enhances the average convective heat transfer rate of inner and outer walls by 11.18% and 11.11%, respectively. Besides, it leads to 70.35% and 62.75% boost in the global frictional and total entropy generation rates, respectively, and 9.04% and 44.11% drop in the global thermal entropy generation rate and global Bejan number, respectively. Also, enhancing Fe_3O_4 concentration from 0.6% to 0.9% at fixed concentration of carbon nanotubes 1.1% boosts the average convective heat transfer coefficient of inner and outer walls by 10.74% and 10.77%, respectively. Labib et al. [73] inspected hydrodynamic and thermal performance of laminar forced convection nanofluid flow by employing two phase mixture model. They considered two particular types of nanofluids, Al_2O_3/Ethylene glycol and Al_2O_3/water, the impact of using base fluids on convective heat transfer performance has been evaluated. The achieved outcomes have clearly illustrates that heat transfer coefficient improvement seems to be more noticeable in case Ethylene Glycol as conventional fluid than water. After that, inclusion of Al_2O_3 nanoparticles into CNT/water nanofluids to synthesize hybrid nanofluid, which have an ability to enhance convective heat transfer. Because CNTs nanofluid depicts higher shear thinning performance which causes the boundary layer thinner. Some recent efforts regarding hybrid nanofluids are reported and a few reference within [74-76].

A number of processes of interest in chemistry, physics, and biology small particles come together to form aggregates. Aggregation of colloidal particles can have a noticeable influence on the properties of suspensions. In many cases aggregation (often coagulation or flocculation) is brought more deliberately in order to enhance solid liquid separation processes, as in water treatment, mineral process, paper making and other fields. Particles transport can be brought about by Brownian diffusion, by fluid motion, or by differential sedimentation. Attachment depends on inter particle forces or colloid interactions; these are of crucial importance in determining whether aggregation can occur and the strength of aggregates. Evans et al. [77] examined thermal conductivity enhancements of nanofluid and nanocomposites due to aggregation and interfacial thermal resistance. Improvement in thermal conductivity because of aggregation is due to chemical dimension and the radius of gyration. They suggested a mathematical model which explains aggregation kinetics and the influence of system chemistry. By considering the influence of interfacial thermal resistance in homogenization model, they presented that an

improvement in thermal conductivity will be reduced, though it can be restricted by huge aggregate sizes. Kendall and Kosseva [78] discussed nanoparticles aggregation under the impact of magnetic field. They found that there is no major impact by imposition of magnetic fields to the dispersed nanoparticles. Therefore, the iron hydroxide FeO(OH) particles seemed non-magnetic at first look. On the other hand, a rise in size and concentration is caused by applying magnetic field to the metastable aggregates. Mendelev and Ivanov [79] addresses about ferrofluid aggregation. They observed that the flexible chain orientation reaction to magnetic field is low as compared to the rigid rod like chains.

Song et al. [80] established an aggregation base rheological model to explore the fragmentation and coagulation of magnetic nanoparticles suspended in nanofluids. They discussed the variations of particle distribution and the particle suspension viscosity of different particle sizes versus the Brownian motion and shear deformation. They noticed that Brownian motion dominates the coagulation process of nanoscale particles, while shear deformation is significant for suspension comprising micro particles. The influence of growing solid volume fraction was established to be same as decreasing shear rate. The increasing fractal dimension creates larger particle sizes and fluctuate geometry standard deviation. By the increase of solid volume fraction, viscosity of magnetic nanofluids becomes greater and by increasing shear rate, viscosity decreased. Wang et al. [81] suggested mathematical model for the estimation of effective thermal conductivity of liquid with dispersion of non-metallic nanoparticles. The suggested fractal model expects well the behavior of effective thermal conductivity with dilute suspension of nanoparticles and matched positively with experimental results for 50nm size CuO particles.

Nkurikiyimfura et al. [82] examined the impact of chain like magnetic nanoparticle aggregates on thermal conductivity of magnetic nanofluids via suggested model of thermal conductivity. The anisotropic characteristic of thermal conductivity ratio was anticipated based on field induced chain-like magnetic nanoparticles aggregates in magnetic nanofluids. Philip et al. [83] observed improvement in thermal conductivity of magnetite based nanofluid because of chainlike patterns. Highest improvement noticed in the thermal conductivity is 300% at particle load of 6.3% of volume fraction. The rise in thermal conductivity is to endorse effective conduction of heat through chainlike patterns prepared in nanofluid. These results are reliable with theoretical insight of enhanced thermal conductivity in nanofluid comprising fractal

aggregates. Gharagozloo and Goodson [84] examined temperature reliant aggregation and diffusion in nanofluids. They utilized parallel plate experiments, Monte Carlo simulations, infrared microscopy, and rate equations for particle and heat transport to splits the influences of particle aggregation and diffusion. The simulation illustrates concentration distributions due to thermal diffusion producing changes in aggregation, thermal conductivity and viscosity. The aggregation causes an unfavorable nanofluid and an optimum diameter of nanoparticle is computed to reduce settling, aggregation and thermal diffusion.

2.1.2 Particulate Flows

This type of flows particularly, the inclusion of solid particles in carrier fluid is a research topic of scientific, industrial and engineering interest due to its significant practical applications like solid rocket exhaust nozzles, crystal growth, blast waves, fluidized beds, ablation cooling, conveying of powdered materials, nuclear reactors, petroleum industry, environmental pollution, centrifugal separation of particles, crude oil purification and physiological flows. Further applications including dust particles in boundary layers, soil salvation due to natural winds, lunar surface erosion due to landing vehicle exhaust and dust entertainment in cloud during nuclear blast. Chakrabarti [85] examined the boundary layer dusty gas flow. Asmolov and Manuilovich [86] have examined the stability of boundary layer dusty gas flow on flat plate. Datta and Mishra [87] have considered boundary layer dusty fluid flow over semi-infinite flat plate. Numerous researchers found the analytical and numerical solutions of dusty fluids [88-89].

Khabazi and Sadeghy [90] numerically investigated the peristaltic flow of circular rigid particles dispersed in viscoplastic fluid in a planar two-dimensional channel using LBM and SPM methods. Their numerical results expose that fluid's yield stress has an influence on the peristaltic transport of solid particles. For the case of single particle suspended in a viscoplastic fluid, which follows the Bingham model as its constitutive equation, they establish that there exists a threshold wave number below which the yield stress slows down the particles transport but above which it has an accelerating influence. A fluid yield stress is also predicted to lower the average velocity of an initially centered single particle at any given confinement ratio. For the setups of two-particle and four-particle, their numerical outcomes show that the initial

positioning of the particles in the channel has a pivotal part in their eventual fate. Gad [91] investigated the collaboration of purely periodic mean flow with peristaltic induced flow. The influence of Hall parameter, Hartmann number and the various included parameters in the problem are evaluated numerically. Their findings exposes that the phase shift increases with increasing the wave number, Reynolds number, Hartmann number and particles concentration but decreases with increasing Hall parameter. Also the reversal flow at the boundary upsurges with increasing the wave number, Reynolds number, Hartmann number and particles concentration but decreases with increasing Hall parameter. Gireesha et al. [92] examined the hydromagnetic boundary layer flow and heat transfer of an electrically conducting dusty fluid due to an unsteady stretching surface embedded in non-Darcy porous media. There finding reveals that, by the inclusion of fine dust particles in pure fluid decreases the thickness of thermal boundary layer. Due to this capability the dusty fluids are preferred to use in technical and scientific applications.

Fu et al. [93] established a two-dimensional numerical scheme to investigate simulation of polygonal particles falling in viscous incompressible fluids. The dynamics of two regular polygonal and circular particles falling in fluids were compared. Finally, by the simulation of sixteen particles moving in a viscous incompressible fluid, they established that their method can handle multiple polygonal particles moving in fluids. The numerical outcomes reflected that the particle shape affects not only the drag forces but also the modes of collision between particles when particles move in viscous incompressible fluids. Polygonal particles can stack up more easily than circular particles in the vertical direction on the surface of the wall below in the fluid domain, while circular particles can more easily slide along their contact line.

Agaliotis and Bernal [94] investigated the drag forces acting on non-spherical shaped particles translating normal to a surface in polymer melt. Drag forces on a particle moving towards a wall in Stokes regime varies as a function of surface distance. Drag forces are affected by the shape of the particles, distance to the wall and mainly the shape of channel between particle and wall. Hence, spherical particles flowing near a convex wall are the particles most prone to sedimentation among the different particles considered. Abbas and Hasnain [95] investigated two phase magneto convection flow of magnetite particles in kerosene nanofluid flow in

horizontal porous annulus under magnetic field. They found that by enhancing magnetic parameter, porosity parameter and volume fraction reduces the fluid velocity while increase in ratio of viscosities as well as pressure give rise to the fluid velocity. The temperature distributions are enhanced by enhancing ratio of thermal conductivities, Eckert number. Bhatti and Zeeshan [96] evaluated the variable magnetic field and endoscopy influence on peristaltic pumping of non-Newtonian particle-fluid suspension. The role of numerous physical parameters is discussed for pressure rise and friction forces. It is found that pressure rise increases via magnetic field. When the fluid illustrates non-Newtonian behavior, then pressure rise also reduces. Moreover, the existence of particles in a fluid tends to resist the pressure.

Saito [97] developed a numerical code for simulating unsteady dusty gas flow by incorporating rarefaction and shock waves. Flow distributions for both phases behind the steady shock wave are evaluated by solving the steady conservation equations. The numerical results achieved for one-dimensional case is authenticated with pseudo-stationary solutions and good agreement between the approaches authenticate the numerical approach. The pseudo-stationary shock distributions can be utilized as an initial condition of unsteady multidimensional simulations. Ramadan and Chamkha [98] studied free convective particulate suspension over an infinite, inclined, permeable and isothermal plate with magnetic field. The particle phase density distribution was supposed to be uniform across the flow domain. The outcomes depict that the particle phase viscosity enhanced the buoyancy effects due to the particle-particle heat conduction across the domain. The generalized impact of magnetic field and heat absorbing fluid is found to damp the flow and thermal profiles. The coefficients of friction for both phases were found to decrease with increase in magnetic field and fluid heat absorption effects.

Chamkha [99] performed numerical simulations of MHD boundary layer flow of particulate suspension comprising finite particles concentration over non-isothermal semi-infinite flat plate with erratic features by employing modified dusty gas model. The displacement thicknesses, skin friction coefficients, wall particle-phase tangential velocity and wall heat transfer coefficient are shown via graphs against several parametric situations. The outcomes specify that the existence of external magnetic field causes displacement thickness of both phases to decreases while skin friction coefficients and wall heat transfer rate enhances over the whole

domain. Palani and Ganeson [100] investigated heat transfer impact on dusty gas flow through a semi-infinite isothermal inclined plate. The Crank Nicolson approach is attempted for solving the dimensionless form of governing flow problem. Impact of sundry parameters on velocity and temperature profiles of both phases, skin friction coefficient and heat transfer rate are represented through graphs. The consequences depicts that the flow profile of dusty gas falls by decreasing inclination angle to the horizontal, while gas velocity reduces by increasing mass concentration of dust particles.

Khare and Singh [101] examined the hydromagnetic non-Newtonian dusty fluid flowing between two parallel inclined plates influenced by gravitational force. The results clearly depicts that by rising magnetic field and velocities of both phases increases at start and taking a maximum value, it starts reducing for inclination of the plates. Also, the results have been attained for numerous inclinations of the plates at fixed magnetic field. Further, these results may be valid in such flows which occur in the industries related to oil, gases, and molten metals flowing through inclined tubes. Ramesh et al. [102] studied momentum and heat transfer features of hydromagnetic dusty fluid flow over an inclined stretching sheet along with non-uniform heat source/sink. Suitable similarity transforms are utilized to reduce the governed flow problem into non-dimensional form and after that solved by Runge-Kutta-Fehlberg fourth-fifth-order numerical scheme in Maple software. They noticed that when fluid particle interaction parameter rises then pure fluid velocity declines while dust particles velocity rises. Further it is observed that velocity distributions decreases as Chandrasekhar number and inclination angle increases. Thermal boundary layer thickness falls down by enhancing Grashof number while increases by increasing inclination. Siddiqa et al. [103] evaluated numerical consequences of two-phase compressible, natural convection flow of dusty gas along vertical wavy surface. Impact of various emerging parameters on skin friction coefficient, heat transfer rate, velocity and temperature distributions are plotted for both phases. From this analysis, it is perceived that mass concentration parameter and the dust parameter extensively promotes the heat transfer rate whereas the compressibility parameters and power index has prominent impact in reducing the skin friction within the boundary layer region.

Gireesha et al. [104] inspected the phenomenon of two phase hydromagnetic boundary layer flow and heat transfer on non-isothermal stretching sheet. The results clearly depict the reduction in momentum and thermal boundary layer thickness with increase in dust particle mass concentration parameter. Also, rate of heat transfer is greater for dusty viscous fluid as equated to pure fluid. Velocity of fluid phase declines for increasing fluid-particle interaction parameter but particle phase velocity enhances. The temperature distribution of both phases and its thermal boundary layer thickness are increasing function of magnetic and porosity parameter and decreasing function of dust particles mass concentration parameter. The rate of heat transfer declines for increase in magnetic and radiation parameter. Thus in order to ease the cooling process magnetic and radiation parameter should be at its minimum. Sheikholeslami et al. [105] examined the impact of thermal radiation on hydromagnetic heat transfer of nanofluid flow via two phase model. They reached at a point that thermal boundary layer thickness declines while rate of heat transfer upsurges by increasing radiation parameter. In another research, Sheikholeslami et al. [106] examined thermal analysis of ferrofluid flow in semi annulus enclosure. Their outcomes indicate that by the increasing of magnetic field strength and radiation parameter the nusselt number increases.

2.2 Governing Equations

Governing equations considered in the present dissertation are of two folds: the first one describes the nanofluid flows while the second one governs the particulate flows. These governing equations are discussed in two sub-sections.

2.2.1 Nanofluid Model

Basic governing laws for the nanofluid flow are same as they are for conventional fluid, which are laws of mass, momentum and energy conservation. However, concern of nanofluid does amend these laws to some level. As we aim to employed the two renowned nanofluid models, Tiwari and Das model [2] and Buongiorno model [3]. Accordingly, the amendment in governing laws will be revealed as for these two models.

2.2.1.1 Law of Mass Conservation

Law of mass conservation for fluid flow is generally identified as continuity equation, mathematically it can be expressed as below:

$$\frac{1}{\rho}\frac{D\rho}{Dt}+\nabla.\mathbf{V}=0, \tag{2.1}$$

Eq. (2.1) is valid for conventional fluid and nanofluid. In above equation, $\frac{D}{Dt}$ represents the material derivative and is formulated as:

$$\frac{D(\ )}{Dt}=\frac{\partial(\ )}{\partial t}+\mathbf{V}\cdot\nabla(\ ), \tag{2.2}$$

Where $\mathbf{V}.\nabla$ indicates convective derivative. Eulerian approach is used for the derivation of Eq. (2.1). A fixed control volume is employed, and variations in fluid are noted as the fluid flow through the control volume. In Lagrangian perspective, the deviations in properties of fluid element are noted by an observer moving with fluid element. Eulerian perspective is generally employed in fluid mechanics. In cylindrical coordinate system the Eq. (2.2) can be written as follows:

$$\frac{D\rho}{Dt}=\frac{\partial\rho}{\partial t}+\frac{1}{r}\frac{\partial(r\rho u)}{\partial r}+\frac{1}{r}\frac{\partial(\rho v)}{\partial\theta}+\frac{\partial(\rho w)}{\partial z}, \tag{2.3}$$

For an incompressible flow

$$\frac{D\rho}{Dt}=0, \tag{2.4}$$

Eq. (2.1) reduces to the below written form:

$$\nabla\cdot\mathbf{V}=0, \tag{2.5}$$

or

$$\frac{1}{r}\frac{\partial(ru)}{\partial r}+\frac{1}{r}\frac{\partial v}{\partial r}+\frac{\partial w}{\partial r}=0. \tag{2.6}$$

2.2.1.2 Law of Momentum Conservation

Law of momentum conservation for an incompressible viscous fluid is communicated as:

$$\rho\left[\frac{\partial \mathbf{V}}{\partial t}+\left(\mathbf{V}.\nabla\right)\mathbf{V}\right]=-\nabla p+\mu\nabla^{2}\mathbf{V}+\mathbf{F}, \tag{2.7}$$

Eq. (2.7) is valid for pure fluid and nanofluid. In above equation $\mathbf{F}$ represents the body forces and the flow problems investigated in thesis the body forces are: force due to magnetic field $\mathbf{F}_M$, force due to external electric field $\mathbf{F}_E$, force due to porous media (Darcy/non-Darcy) $\mathbf{F}_P$, buoyancy force due to convection $\mathbf{F}_B$ and force due to drag $\mathbf{F}_D$.

$$\mathbf{F}=\mathbf{F}_M+\mathbf{F}_E+\mathbf{F}_B+\mathbf{F}_P+\mathbf{F}_D. \tag{2.8}$$

Buoyancy force $\mathbf{F}_B$ is defined as the force acting against the gravity direction that affects all elements immersed in fluid. When an element is put in a liquid, the element weight pushes down on the liquid while an upward buoyancy force pushes upward on the element, acting against gravity. Mathematically the buoyancy force can be formulated as follows:

$$\mathbf{F}_B=\rho g V_s. \tag{2.9}$$

In which V_s is the submerged volume of objects and g is acceleration due to gravity.

Drag force F_D is defined as force of viscosity on a small sphere moving through a viscous fluid and can be expressed as:

$$\mathbf{F}_D=6\pi\mu r v. \tag{2.10}$$

Here r signifies radius of spherical element and v signifies the flow velocity relative to the element.

2.2.1.3 Law of Energy Conservation

The energy conservation law for viscous incompressible nanofluid in the existence of dissipation energy and heat source/sink is given as below:

$$\rho c_p \left[\frac{\partial T}{\partial t} + \mathbf{V}.\nabla T \right] = -\nabla.\mathrm{Q} + Q_0 + \Phi. \tag{2.11}$$

In Eq. (2.11) Φ denotes the dissipation in energy, Q is energy flux, which is sum of conduction heat flux $\left(k\nabla T\right)$ and radiative heat flux Q_r and Q_0 is the heat source/sink. Mathematically, energy flux can be illustrated as:

$$\mathrm{Q} = -k\nabla T + Q_r, \tag{2.12}$$

and

$$\nabla.\mathrm{Q} = -\nabla.\left(k\nabla T\right) + \nabla.\mathrm{Q}_r. \tag{2.13}$$

In current thesis the viscous dissipation and Ohmic dissipation are considered.

$$\Phi = \Phi_{viscous} + \Phi_{ohmic}, \tag{2.14}$$

where

$$\Phi_{viscous} = \mu\left(\frac{\partial u}{\partial r}\right)^2, \tag{2.15}$$

and

$$\Phi_{ohmic} = \sigma\left(uB_0 - E_0\right)^2, \tag{2.16}$$

putting Eq. (2.15) and Eq. (2.16) in Eq. (2.14), we got following form:

$$\Phi = \mu\left(\frac{\partial u}{\partial r}\right)^2 + \sigma\left(uB_0 - E_0\right)^2. \tag{2.17}$$

The internal heat source/sink consider in current research is formulated as:

$$Q_0 = \frac{kU_0^2}{\nu^2}[A(T_w - T_\infty)e^{-\eta} + B(T - T_\infty)]. \tag{2.18}$$

Where A and B are parameters representing heat generation or absorption. When $A<0, B<0$ then heat absorption (sink) and when $A>0, B>0$ then heat generation (source). The form of energy equation for the nanofluid is found to be:

$$\left(\rho c_p\right)_f \left[\frac{\partial T}{\partial t}+\mathbf{V}.\nabla T\right]=k_f\nabla^2 T+\left(\rho c_p\right)_p\left[D_B\nabla C.\nabla T+D_T\frac{\nabla T.\nabla T}{T_\infty}\right] -\nabla.\mathrm{Q}_r+Q_0+\Phi. \tag{2.19}$$

2.2.1.4 Law of Concentration Conservation

Mass transfer explains the transport of mass (constituents, species) from one position to another position. In majority of cases, the mass exchange of species happens along with chemical reactions. Mathematical form of concentration conservation of nanoparticles along with chemical reaction and Arrhenius activation energy is expressed as below:

$$\frac{\partial C}{\partial t}+\mathbf{V}.\nabla C=-\frac{1}{\rho_p}\nabla\cdot\mathbf{j}_p-k_r^2\left(\frac{T}{T_\infty}\right)^n e^{\frac{-E_a}{\kappa T}}\left(C-C_\infty\right), \tag{2.20}$$

In above equation $k_r^2\left(\frac{T}{T_\infty}\right)^n e^{\frac{-E_a}{\kappa T}}$ is the modified Arrhenius function and $\mathbf{j}_p$ represents diffusion mass flux for the nanoparticles, which is summation of two terms Brownian diffusion and thermophoretic diffusion. Mathematically

$$\mathbf{j}_p=\mathbf{j}_{p,B}+\mathbf{j}_{p,T},$$
$$\mathbf{j}_p=-\rho_p D_B\nabla C-\rho_p D_T\frac{\nabla T}{T_\infty}. \tag{2.21}$$

The coefficient of Brownian diffusion via by Einstein–Stokes equation is given by:

$$D_B=\frac{k_B T}{3\pi\mu d_p}, \tag{2.22}$$

The mathematical form of thermophoretic velocity $\mathbf{V}_T$ can be written as follows:

$$\mathbf{V}_T = -\tilde{\beta}\frac{\mu}{\rho}\frac{\nabla T}{T_\infty}, \tag{2.23}$$

here $\tilde{\beta}$ is the proportionality factor, which can be formulated as follows:

$$\tilde{\beta} = 0.26\frac{k_f}{2k_f + k_p}, \tag{2.24}$$

hence the flux due to thermophoretic diffusion is expressed as below:

$$\mathbf{j}_{p,T} = \rho_p C\mathbf{V}_T = -\rho_p D_T \frac{\nabla T}{T_\infty}, \tag{2.25}$$

the correlation for thermophoretic diffusion coefficient is written as:

$$D_T = \tilde{\beta}\frac{\mu}{\rho}C, \tag{2.26}$$

using Eq. (2.21) in Eq. (2.20) then the conservation equation can be expressed as follows:

$$\frac{\partial C}{\partial t} + \mathbf{V}.\nabla C = D_B\nabla^2 C + \frac{D_T}{T_\infty}\nabla^2 T - k_r^2\left(\frac{T}{T_\infty}\right)^n e^{\frac{-E_a}{\kappa T}}\left(C - C_\infty\right). \tag{2.27}$$

2.2.2 Two Fluid Model

This model deals base fluid and solid particles as two distinct continua that occupy the identical volume. Both the continua are developed by their separate conservation equations. The relation of both the continua is shown by source terms, which are added in governing equations. For instance, the momentum equation comprises an extra force that signifies the drag applied by the particles on the carrying fluid. Also, the mass and energy conservation equations contains terms that symbolize the sublimation/evaporation of particles and the energy transfer from the particles to the fluid, respectively. These terms are essential to model, and normally empirical equations are employed for their modeling purpose. The comprehensive form of equations of two fluid model [107] can be expressed as follows:

Law of mass conservation for fluid and particle phases:

$$\frac{\partial}{\partial t}\left[(1-\varphi)\rho_f\right]+\frac{\partial}{\partial x_j}\left[(1-\varphi)\rho_f u_j\right]=J, \tag{2.28}$$

$$\frac{\partial}{\partial t}\left[\varphi\rho_s\right]+\frac{\partial}{\partial x_j}\left[\varphi v_j\right]=-J. \tag{2.29}$$

Law of momentum conservation for fluid and particle phases:

$$\frac{\partial}{\partial t}\left[(1-\varphi)\rho_f u_i\right]+\frac{\partial}{\partial x_j}\left[(1-\varphi)\rho_f u_j u_i\right]=(1-\varphi)\left[\rho_f g_i-\frac{\partial p_i}{\partial x_i}+\mu_f\frac{\partial^2 u_i}{\partial x_j\partial x_j}\right]+ F_i+Jv_i, \tag{2.30}$$

$$\frac{\partial}{\partial t}\left[\varphi\rho_s v_i\right]+\frac{\partial}{\partial x_j}\left[\varphi\rho_s v_j v_i\right]=(1-\varphi)\left[\rho_s g_i-\frac{\partial(p+p_c)}{\partial x_i}+\mu_s\frac{\partial^2 v_i}{\partial x_j\partial x_j}\right]-F_i-Jv_i. \tag{2.31}$$

Law of energy conservation for fluid and particle phases:

$$\frac{\partial}{\partial t}\left[(1-\varphi)\rho_f c_f T_f\right]+\frac{\partial}{\partial x_j}\left[(1-\varphi)\rho_f c_f T_f u_j\right]=(1-\varphi)\left[k_f\frac{\partial^2 T_f}{\partial x_j\partial x_j}\right]+q, \tag{2.32}$$

$$\frac{\partial}{\partial t}\left(\varphi\rho_s c_s T_s\right)+\frac{\partial}{\partial x_j}\left(\varphi\rho_s c_s T_s v_j\right)=\varphi k_s\frac{\partial^2 T_s}{\partial x_j\partial x_j}-q. \tag{2.33}$$

The mass source term J appearing in Eq. (2.28) and Eq. (2.29) characterizes the mass transferred to the base fluid from the particles due to chemical reactions, evaporation, and sublimation. In momentum equation the similar term multiplied by the particle velocity seems to characterize the momentum transferred as an outcome of this mass exchange between the phases. Also, the force term F_i appearing in the momentum equation is signifying the hydrodynamic force between particles and fluid like drag and lift force. In energy equation, the heat source term q denotes the entire enthalpy transfer per unit volume from the particles to the carrier fluid and contains the latent heat of evaporation or sublimation. The pressure term p_c characterizes the particle collisions and can be ignored if collisions are not important.

2.3 Porosity

A substance comprising of solid matrix along with an interconnected void is called as porous medium. We assumed that the solid matrix may be rigid or it goes through slight deformation. Mostly porous medium is measured by its porosity but some time

by other characteristics likes permeability, electrical conductivity and tensile strength. Porosity of a porous media is described as ratio between void volume and total volume. After an experimental investigation Henry Darcy defined mathematical form of porosity known as Darcy's law. Mathematically, it can be expressed as:

$$\mathbf{V} = -\frac{k_1}{\mu}\nabla p, \tag{2.34}$$

after modifying the above expression, we obtained the following relation:

$$\nabla p = -\frac{\mu}{k_1}\mathbf{V}, \tag{2.35}$$

as Darcy law is not enough for the illustration of high flow rate in porous medium because of low Reynolds number based on mean diameter of pore. It is well established fact, when the Reynolds number rise to critical value, then Eq. (2.35) is not effective anymore. To cover this gap, Forchheimer [54] suggested a nonlinear correction of Darcy's law as follows:

$$\nabla p = -\frac{\mu}{k_1}\mathbf{V} - \rho F\,|\mathbf{V}|\mathbf{V}, \tag{2.36}$$

Eq. (2.36) can be called as non-Darcy Forchheimer modification. Therefore

$$\mathbf{F}_p = -\frac{\mu}{k_1}\mathbf{V} - \rho F\,|\mathbf{V}|\mathbf{V}. \tag{2.37}$$

2.4 Magnetohydrodynamics

The term magnetohydrodynamic (MHD) derives from three words "magneto" signifies magnetic field, "hydro" signifies liquid and "dynamics" signifies motion. In nature and industrial processes, we noticed that the magnetic fields impelling the performance of fluid flows. Magnetic fields are utilized in metallurgical industry for stir, levitate, pump and heat liquid metals. The earth's magnetic field, defending the surface from harmful radiations. We use magnetohydrodynamics for all cases, where magnetic field is coupled with velocity field, in case of an electrically conducting and non-magnetic fluid. The fundamental equations that oversee magnetohydrodynamic are the mix of Navier Stokes and Maxwell's equations. Within the sight of magnetohydrodynamics, we can express the momentum equation as:

$$\rho\left(\frac{\partial \mathbf{V}}{\partial t}+\mathbf{V}.\nabla\mathbf{V}\right)=\nabla\cdot\tau+\mathbf{J}\times\mathbf{B}, \tag{2.38}$$

In Eq. (2.38), the term $\mathbf{J}\times\mathbf{B}$ signifies Lorentz force and can be expressed as:

$$\mathbf{J}\times\mathbf{B}=\frac{(\mathbf{B}\cdot\nabla)\mathbf{B}}{\mu_0}-\nabla\left(\frac{B_0^2}{2\mu_0}\right). \tag{2.39}$$

Maxwell's equations are illustrated by the following expressions.

$$\nabla\cdot\mathbf{B}=0, \tag{2.40}$$

Lorentz force $$\mathbf{F}_L=\mathbf{J}\times\mathbf{B}\ , \tag{2.41}$$

Ohm's law $$\mathbf{J}=\sigma(\mathbf{E}+\mathbf{V}\times\mathbf{B}), \tag{2.42}$$

Faraday's Law $$\nabla\times\mathbf{E}=-\frac{\partial\mathbf{B}}{\partial t}, \tag{2.43}$$

Ampere's Law $$\nabla\times\mathbf{B}=\mu_0\mathbf{J}\ , \tag{2.44}$$

Charge conservation $$\nabla\cdot\mathbf{J}=0. \tag{2.45}$$

2.5 Non-dimensional Parameters

In fluid mechanics, non-dimensional numbers are useful for determining the flow features of fluid. Some important dimensionless numbers arising in the current flow problems are discussed as below:

i. Prandtl Number

The ratio of momentum diffusivity to thermal diffusivity is termed as Prandtl number after German physicist L. Prandtl (1875-1953). Mathematically, it can be written as:

$$Pr=\frac{\nu}{\tilde{\alpha}}. \tag{2.46}$$

ii. Eckert Number

It deliberates the correlation between flows kinetic energy and boundary layer enthalpy difference. Eckert number characterizes heat dissipation and entitled after Ernst R. G. Eckert (1904-2004). Mathematically it is formulated as:

$$Ec = \frac{u_w^2}{c_p \Delta T}. \tag{2.47}$$

iii. Reynolds Number

The ratio of inertial forces to viscous forces is called Reynolds number and is named after Osborne Reynolds (1842–1912). Mathematically it can be defined as:

$$Re = \frac{UL}{\nu}. \tag{2.48}$$

iv. Lewis Number

The ratio of thermal diffusivity to mass diffusivity is known as Lewis number after Warren K. Lewis (1882–1975). Mathematically, it is formulated as:

$$Le = \frac{\ddot{\alpha}}{D_B}. \tag{2.49}$$

v. Schmidt Number

It is ratio of momentum diffusivity to mass diffusivity. It is termed after German engineer Ernst Heinrich Wilhelm Schmidt (1892–1975). Mathematically, it can be expressed as:

$$Sc = PrLe = \frac{\nu}{D_B}. \tag{2.50}$$

vi. Sherwood Number

The ratio of convective mass transfer to rate of diffusive mass transport is called Sherwood number. It is entitled after Thomas Kilgore Sherwood and is formulated as:

$$Sh = \frac{hx}{D_B}. \tag{2.51}$$

vii. Biot Number

The ratio of internal diffusion resistance to external convection resistance is known as Biot number. It is named after J. B. Biot. Mathematically it is formulated as:

$$Bi = \frac{hL}{k}. \tag{2.52}$$

viii. Nusselt Number

The ratio of convective to conductive heat transfer through the boundary is termed as Nusselt number. Mathematically, it can be written as:

$$Nu = \frac{hL}{k}. \tag{2.53}$$

ix. Skin Friction Coefficient

The ratio of skin shear stress to dynamic pressure of free stream is called skin friction coefficient. Mathematically, it can be stated in the subsequent form:

$$C_f = \frac{2\tau_w}{\rho u_w^2}. \tag{2.54}$$

x. Grashof Number

The ratio of buoyancy to viscous forces is known as Grashof number. It is used frequently in natural or mixed convection flows. Mathematically, it is formulated as,

$$Gr = \frac{g\beta\Delta TL^3}{\nu^2}. \tag{2.55}$$

xi. Magnetic Parameter

The ratio between electromagnetic to viscous forces is termed as magnetic parameter. Mathematically, it can be written as below:

$$M = B_0 L\sqrt{\frac{\sigma}{\mu}}. \tag{2.56}$$

Chapter 3

Electromagnetohydrodynamics Transport of Al_2O_3 Nanoparticles in Ethylene Glycol over a Convectively Heated Stretching Cylinder

3.1 Introduction

In this chapter, the transport of Al_2O_3 nanoparticles in ethylene glycol conventional fluid over linearly stretching cylinder is investigated. The current research employs a convective surface boundary condition for heat transfer exploration. Flux model proposed by Rosseland [104] is employed to examine effects of thermal radiation. The governing flow problem is comprise of highly nonlinear ordinary differential equations. Appropriate similarity transformations are used to reduce the equations in similar form, which are tackled by Runge-Kutta-Fehlberg fourth-fifth order (RKF45) numerical scheme with shooting algorithm. The impact of numerous emerging parameters on velocity and temperature distributions are argued in all aspects and reflected through the graphs.

3.2 Geometry of Problem

An incompressible, steady, boundary layer flow of conducting viscous ethylene glycol base fluid with alumina Al_2O_3 nanoparticles over linear stretching cylinder is deliberated. The *x*-axis and *r*-axis are considered along the cylinder axis and along with the radial directions respectively. The magnetic field $\mathbf{B} = (0, B_0, 0)$ and electric field $\mathbf{E} = (0, 0, -E_0)$ are applied to interpret the flow region. To generate flow, the elastic cylinder is stretched linearly with wall velocity. The schematic overview and coordinate system are presented in figure. 3.1.

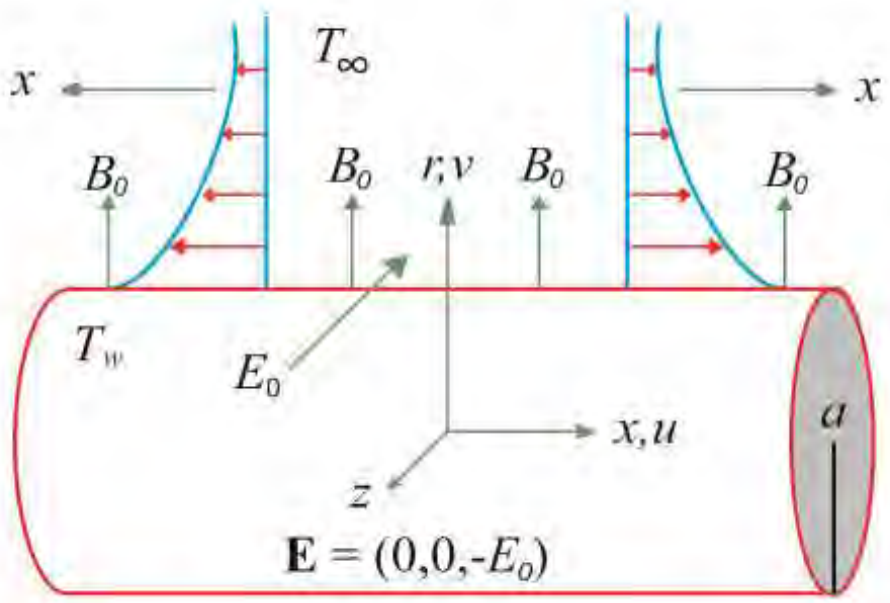

Figure 3.1: Flow schematic, coordinates and geometrical variables.

3.3 Mathematical Formulation

From Maxwell's equations: $\nabla \cdot \mathbf{B} = 0$ and $\nabla \times \mathbf{E} = \mathbf{0}$. In case of weak magnetic field, the magnetic and electric fields may follow Ohm's law. The induced magnetic field is ignored due to its lesser value. The bottom boundary of cylinder is heated convectively by a liquid of temperature T_f. Under the above mentioned physical assumptions, governing equations are described as follows:

$$\frac{\partial (ru)}{\partial x} + \frac{\partial (rv)}{\partial r} = 0, \tag{3.1}$$

$$\rho_{nf}\left(u\frac{\partial u}{\partial x} + v\frac{\partial u}{\partial r}\right) = \frac{\mu_{nf}}{r}\frac{\partial}{\partial r}\left(r\frac{\partial u}{\partial r}\right) + \sigma\left(E_0 B_0 - B_0^2 u\right), \tag{3.2}$$

$$\left(\rho c_p\right)_{nf}\left(u\frac{\partial T}{\partial x} + v\frac{\partial T}{\partial r}\right) = \frac{k_{nf}}{r}\frac{\partial}{\partial r}\left(r\frac{\partial T}{\partial r}\right) + \mu_{nf}\left(\frac{\partial u}{\partial r}\right)^2 + \sigma\left(uB_0 - E_0\right)^2 - \frac{\partial Q_r}{\partial r}. \tag{3.3}$$

The applicable boundary conditions are as follows:

$$u = 2cx,\ v = 0,\ k_f\frac{\partial T}{\partial r} = -h\left(T_f - T\right) \text{ at } r = a, \tag{3.4}$$

$$u \to 0,\ T \to T_\infty \qquad \text{as } r \to \infty. \tag{3.5}$$

The radiation heat flux model suggested by Roseland [104] is given as follows:

$$Q_r = -\frac{4\sigma^*}{3k^*}\frac{\partial T^4}{\partial r}, \tag{3.6}$$

by the Taylor series expansion of T^4 about T_∞ and omitting greater order terms:

$$T^4 \cong 4T_\infty^3 T - 3T_\infty^4, \tag{3.7}$$

$$\frac{\partial Q_r}{\partial r} = -\frac{16\sigma^* T_\infty^3}{3k^*}\frac{\partial^2 T}{\partial r^2}. \tag{3.8}$$

The physical characteristics of alumina nanoparticles and ethylene glycol base fluid are illustrated in below table.

Table 3.1: Thermophysical Properties of Ethylene glycol and Al_2O_3

Physical properties	Ethylene glycol	Al_2O_3
$\rho\ (kgm^{-3})$	1110	3980
$c_p\ (Jkg^{-1}K^{-1})$	2400	840
$k\ (Wm^{-1}K^{-1})$	0.26	33

The correlations for nanofluid density ρ_{nf} and heat capacitance $\left(\rho c_p\right)_{nf}$ are given as:

$$\rho_{nf} = (1-\varphi)\rho_f + \varphi\rho_p,\ \left(\rho c_p\right)_{nf} = (1-\varphi)\left(\rho c_p\right)_f + \varphi\left(\rho c_p\right)_p. \tag{3.9}$$

The correlations for effective dynamic viscosity and thermal conductivity of nanofluid offered by Brinkman [108] are given by:

$$\frac{\mu_{nf}}{\mu_f} = \frac{1}{(1-\varphi)^{2.5}}\ ,\quad \frac{k_{nf}}{k_f} = \frac{k_p + 2k_f + 2\varphi(k_p - k_f)}{k_p + 2k_f - \varphi(k_p - k_f)}. \tag{3.10}$$

To transform the boundary value problem in self-similar form, the following similarity transformations are utilized:

$$\eta = \left(\frac{r}{a}\right)^2,\ u = 2cxf'(\eta),\ v = -\frac{ca}{\sqrt{\eta}}f(\eta),\ \theta = \frac{T - T_\infty}{T_w - T_\infty}, \tag{3.11}$$

using similarity transformation Eq. (3.11) in Eq. (3.1) to Eq. (3.5), the problem in non-dimensional form can be presented as:

$$A_1\left(\eta f''' + f''\right) + A_2 Re\left(ff'' - f'^2\right) + M\left(E_1 - f'\right) = 0, \tag{3.12}$$

$$A_3\left(\theta'+\eta\theta''\right)+Rd\eta\theta''+A_4RePr\theta' f+A_1\eta EcPrf''^2+MPrEc\left(f'-E_1\right)^2=0, \qquad (3.13)$$

the corresponding set of boundary conditions is:

$$f(1)=0,\ f'(1)=1,\ \theta'(1)=-Bi\left\{1-\theta(1)\right\}, \qquad (3.14)$$

$$f'(\infty)\to 0,\ \theta(\infty)\to 0. \qquad (3.15)$$

Here prime represents the derivative with respect to η. The constant terms and various emerging parameters appearing in Eq. (3.12) to Eq. (3.15) are formulated as follows:

$$\left.\begin{aligned} &A_1=\frac{1}{(1-\varphi)^{2.5}},\ A_2=(1-\varphi)+\varphi\frac{\rho_p}{\rho_f},\ A_3=\frac{k_p+2k_f+2\varphi(k_p-k_f)}{k_p+2k_f-\varphi(k_p-k_f)},\\ &A_4=(1-\varphi)+\varphi\frac{(\rho c_p)_p}{(\rho c_p)_f},\ Re=\frac{ca^2}{2\nu},\ M=\frac{\sigma B_0^2a^2}{4\mu_f},\ Pr=\frac{\mu_f(c_p)_f}{k_f},\\ &Ec=\frac{u_w^2}{c_p(T_w-T_\infty)},\ E_1=\frac{E_0}{B_0u_w},\ Rd=\frac{16\sigma^*T_\infty^3}{3k^*k_f},\ Bi=\frac{ha}{2k}. \end{aligned}\right\}. \qquad (3.16)$$

3.3.1 Physical Parameters of Interest

The physical parameters of scientific and engineering importance are the skin friction coefficient and Nusselt number. Mathematically, they are formulated as follows:

$$C_f=\frac{2\tau_w}{\rho_f u_w^2},\ Nu=\frac{aQ_w}{k_f(T_w-T_\infty)}, \qquad (3.17)$$

$$\text{where}\quad \tau_w=\mu_f\left(\frac{\partial u}{\partial r}\right)_{r=a},\ Q_w=-\left[\left(k_f+\frac{16\sigma^*T_\infty^3}{3k^*}\right)\frac{\partial T}{\partial r}\right]_{r=a}, \qquad (3.18)$$

Using similarity transforms defined in Eq. (3.11), the subsequent dimensionless form is given as follows:

$$C_f\left(\frac{Re}{a}\right)=f''(1),\ Nu=-2(1+Rd)\theta'(1). \qquad (3.19)$$

3.4 Solution Procedure

In current study, the resulting flow phenomenon is described by system of nonlinear coupled ordinary differential equations Eq. (3.12) and Eq. (3.13) subject to boundary

conditions Eq. (3.14) and Eq. (3.15). The governing system of equations is first converted into set of first order ordinary differential equations. By supposing

$$f = F_1,\ f' = F_2,\ f'' = F_3,\ \theta = F_4,\ \theta' = F_5, \tag{3.20}$$

the system of five simultaneous 1st order equations can be described as below:

$$\begin{bmatrix} F_1' \\ F_2' \\ F_3' \\ F_4' \\ F_5' \end{bmatrix} = \begin{bmatrix} F_2 \\ F_3 \\ -\frac{1}{A_1\eta}\left\{A_1F_3 + A_2Re\left(F_1F_3 - F_2^2\right) + M\left(E_1 - F_2\right)\right\} \\ F_5 \\ -\frac{1}{(A_3 + Rd)\eta}\left\{\begin{matrix} A_3F_5 + A_4RePrF_1F_5 + A_1\eta PrEcF_3^2 + \\ MPrEc\left(F_2 - E_1\right)^2 \end{matrix}\right\} \end{bmatrix}, \tag{3.21}$$

The boundary conditions are written follows:

$$F_1 = 0, F_2 = 1, F_5 = -Bi\left(1 - F_4\right) \quad \text{at} \quad \eta = 1. \tag{3.22}$$

Since $F_3(1)$ and $F_4(1)$ are missing, so we may start with the initial values of $F_3(1) = g_{10}$ and $F_4(1) = g_{20}$. Let γ_1 and γ_2 are accurate $F_3(1)$ and $F_4(1)$ accordingly. Assuming F_3 and F_4 at $\eta = \eta_\infty$ by $F_3(g_{10}, g_{20}, \eta_\infty)$ and $F_4(g_{10}, g_{20}, \eta_\infty)$. Since F_3 and F_4 at $\eta = \eta_\infty$ are clearly function of γ_1 and γ_2 , they are expanded in Taylor series about $\gamma_1 - g_{10}$ and $\gamma_2 - g_{20}$ respectively. After solving the system of Taylor series expansions for $\delta\gamma_1 = \gamma_1 - g_{10}$ and $\delta\gamma_2 = \gamma_2 - g_{20}$, we obtained the new estimates $g_{11} = g_{10} + \delta g_{10}$ and $g_{21} = g_{20} + \delta g_{20}$. Next, the complete procedure is reiterated with $F_1(1)$, $F_2(1)$, g_{11}, g_{21}, $F_5(1)$ are initial conditions. With the latest estimates of γ_1, γ_2 the whole procedure is reiterated up to prescribed boundary conditions are satisfied. Finally $g_{1n} = g_{1(n-1)} + \delta g_{1(n-1)}$ and $g_{2n} = g_{2(n-1)} + \delta g_{2(n-1)}$ for $n = 1, 2, 3, \ldots$ are achieved, which appeared to be the most preferred approximate initial values of $F_3(1)$ and $F_4(1)$. By this technique, when all missing conditions are obtained, then the resulting system of five first order equations are handled by Runge-Kutta-Fehlberg (RKF45) numerical scheme and the simulation error is chosen to be 10^{-5}.

The choice of η_∞ varies from 2 to 10 subject to the involving parameters so that no numerical oscillations would occur.

3.5 Illustration of Results

For authenticity of results, we have validated the obtained results with already published in literature and found that they are in better agreement as revealed in table 3.2.

Table 3.2: Validation of results for Nusselt number $-\theta'(1)$, at fixed $Re = 10, Rd = \varphi = E_1 = M = Ec = 0, Bi \to \infty$

Pr	Wang[109]	Ishak [110]	Pandey [111]	Present
0.7	1.568	1.5683	1.58679	1.5962
2	3.035	3.0360	3.03534	3.0259
7	6.160	6.1592	6.15590	6.1198
10	10.77	7.4668	7.46230	7.4088

Role of various involving parameters like magnetic parameter, Eckert number, electric field parameter, radiation parameter and Biot number on flow and heat transfer features has been portrayed through graphs. For evaluation of results, the values of some parameters are fixed as *Pr = 135*, *Re = 7.0.*

Figures 3.2 and 3.3 represent variations of momentum and thermal boundary layer versus magnetic parameter. Figure 3.2 displays that the momentum boundary layer thickness drops by rising magnetic number. Figure 3.3 shows that the temperature profiles are enhanced as magnetic parameter grows stronger because of the fact that magnetic field produces a Lorentz force which resists the flow, so the temperature increases. Figures 3.4 and 3.5 describe the impact of electric parameter on flow and temperature distributions. From figure 3.4, we examined that impact of electric parameter on the velocity is more expressively away from the stretching surface and prominent throughout the boundary layer. This figure exposes that the effect of electric parameter is to move the flow patterns away from the stretched boundary. Transferring of streamlines away from the stretching sheet is more prominent. Figure 3.5 represents the influence of electric field parameter on

temperature profiles. We note that the temperature distribution rises with increasing values of the electric parameter. Figure 3.6 exhibits the impact of radiation parameter on temperature distributions. We concluded that the temperature is directly proportional to thermal radiation parameter. A special case $Rd = 0$ relates to the flow investigation without thermal radiation.

Figure 3.7 represents the variation in thermal boundary layer profiles for several values of Eckert number. From figure, we examined that the temperature profiles increases by raising the Eckert number. If $Ec = 0$ relates to the flow without viscous dissipation as well as Ohmic dissipation. Figure 3.8 highlights the deviations of skin friction coefficient versus electric field parameter for numerous values of magnetic number. This figure shows that the skin friction coefficient rises as we increase electric parameter and magnetic number. Figure 3.9 illustrates the impact of Biot number on Nusselt number for numerous values of electric parameter. Nusselt number demonstrates increasing behavior with the increase of Biot number and electric parameter. Figure 3.10 shows the behavior of Nusselt number with radiation number for various values of electric parameter. From figure, we notice that Nusselt number rises by growing radiation number but by growing electric parameter the Nusselt number drops.

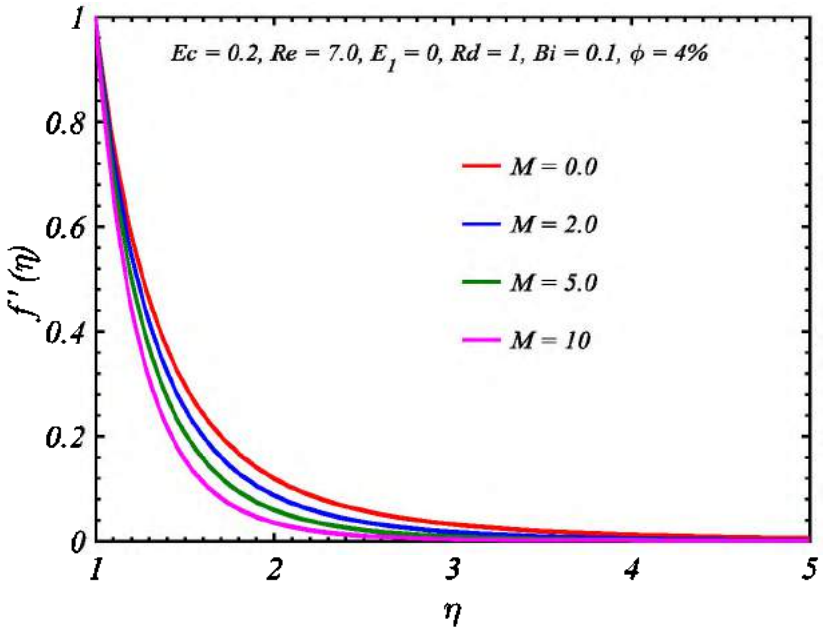

Figure 3.2: Velocity distribution $f'(\eta)$ versus magnetic parameter *M*.

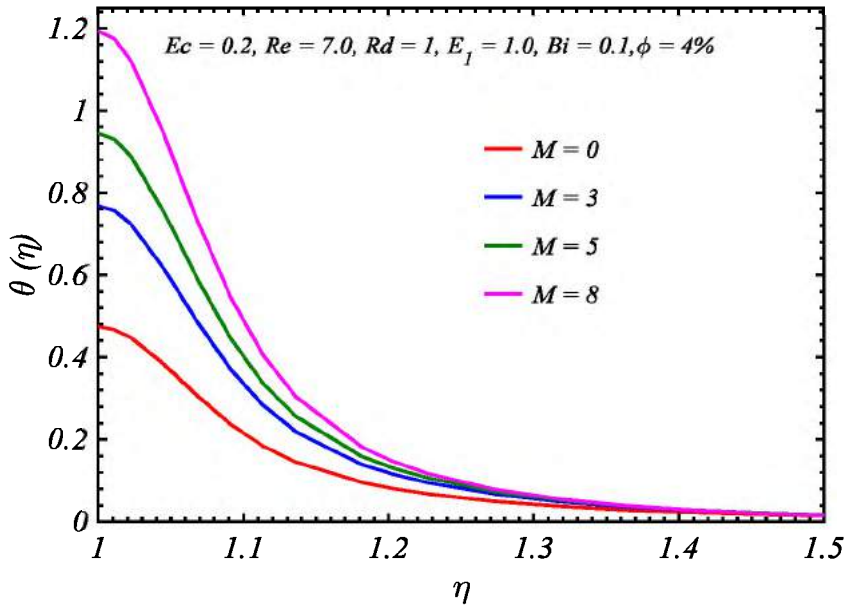

Figure 3.3: Temperature distribution $\theta(\eta)$ versus magnetic parameter M.

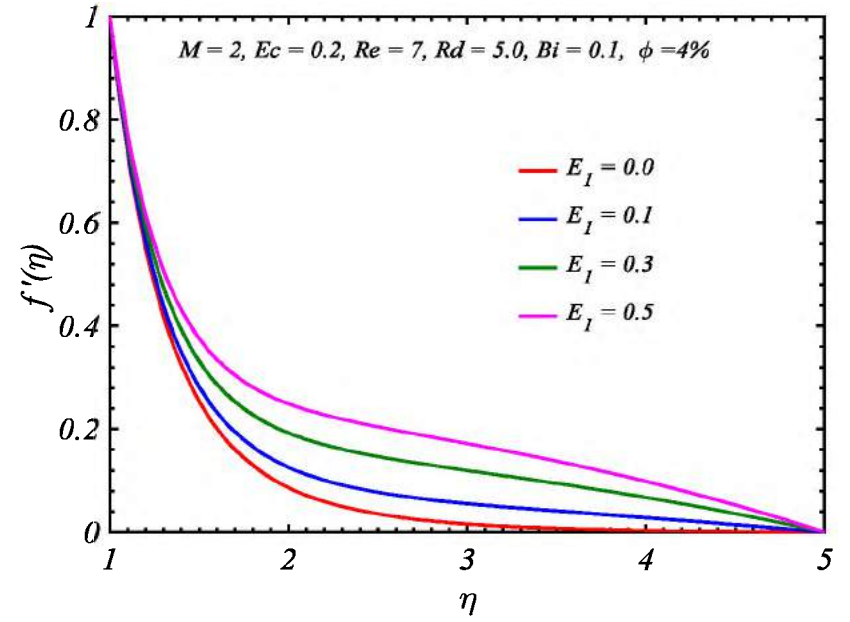

Figure 3.4: Velocity distribution $f'(\eta)$ versus electric parameter E_1.

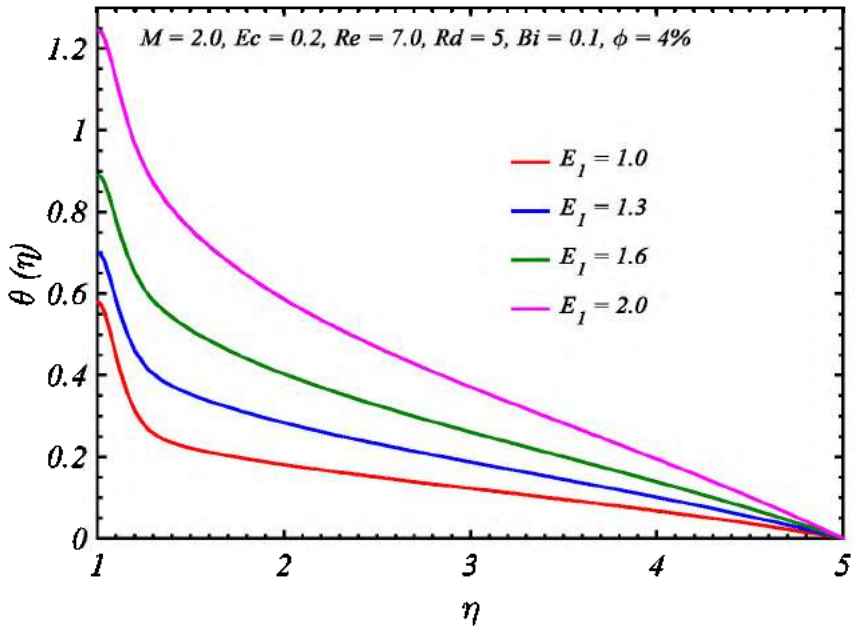

Figure 3.5: Temperature distribution $\theta(\eta)$ versus electric parameter E_1.

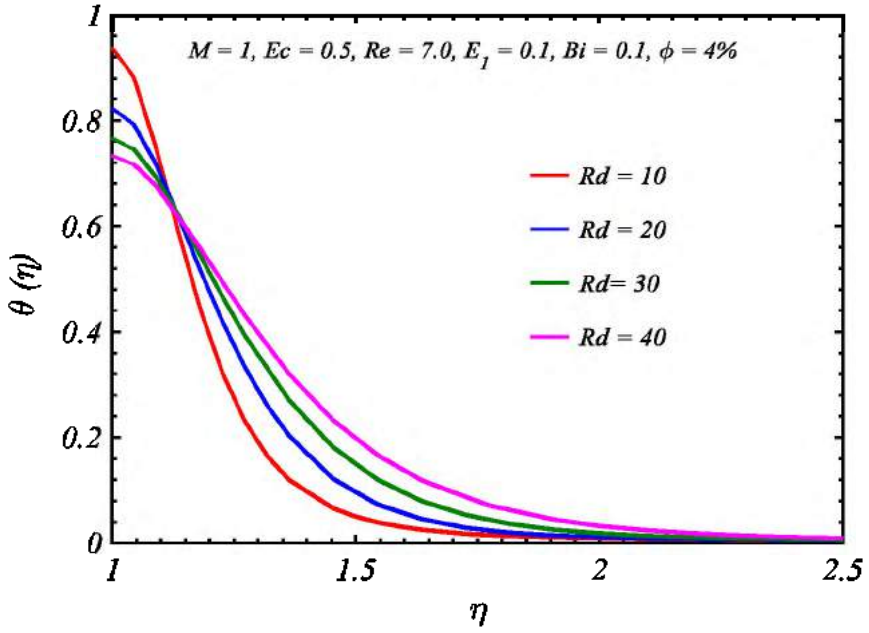

Figure 3.6: Temperature distribution $\theta(\eta)$ versus radiation parameter Rd.

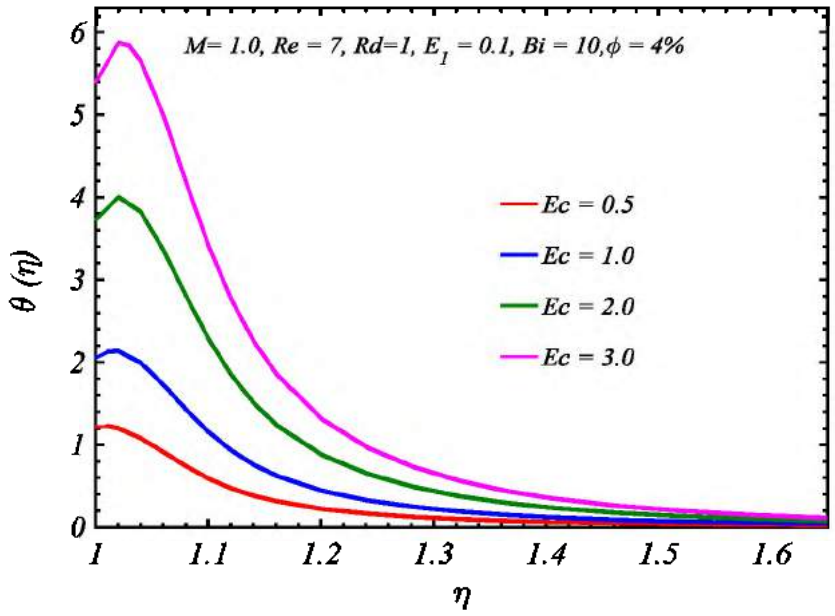

Figure 3.7: Temperature distribution $\theta(\eta)$ versus Eckert number Ec.

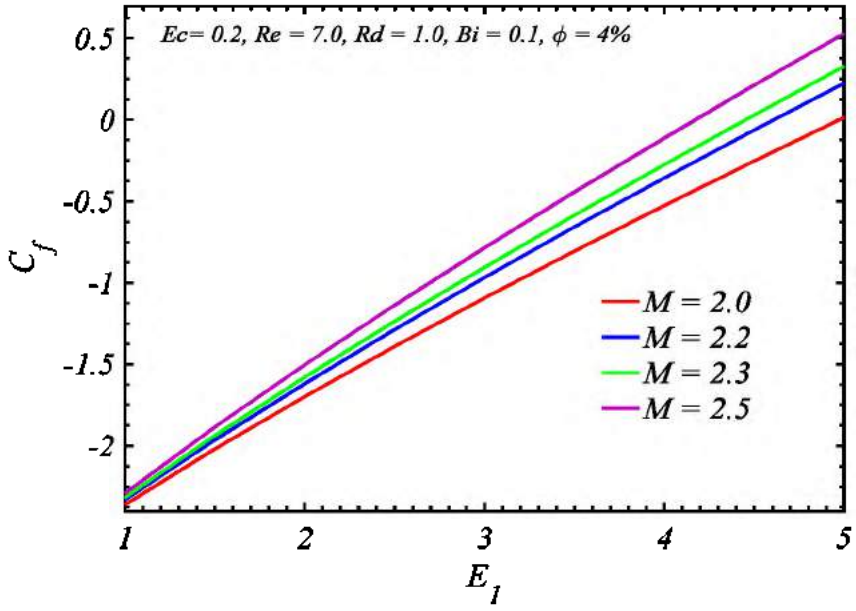

Figure 3.8: Skin friction coefficient versus electric parameter E_1.

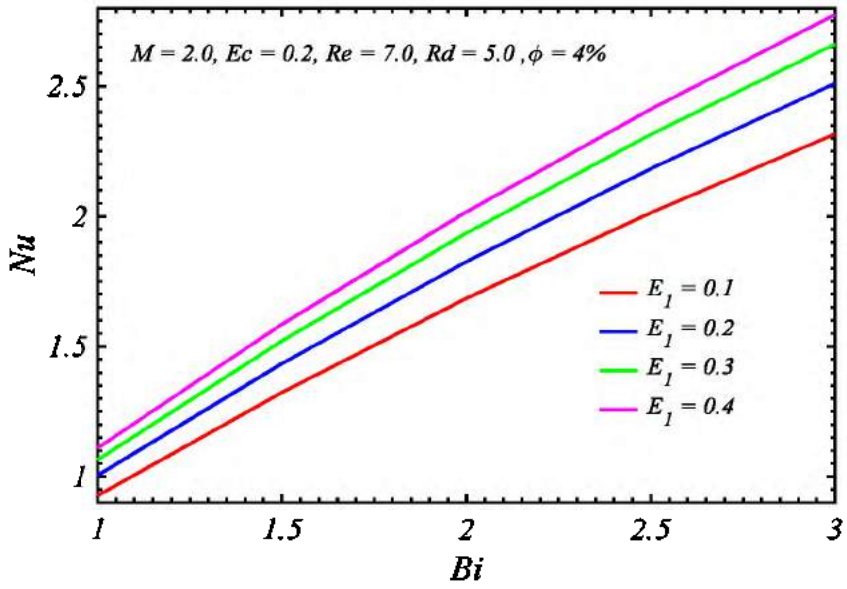

Figure 3.9: Nusselt number Nu versus Biot number Bi .

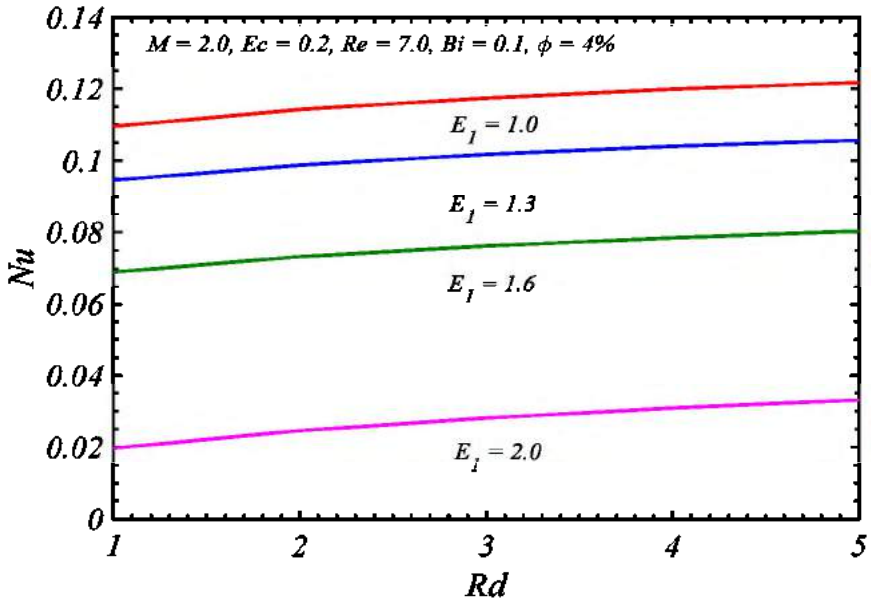

Figure 3.10: Nusselt number Nu versus electric parameter E_1. .

Chapter 4

Heat Transfer Enhancement in Hydromagnetic Alumina-Copper/Water Hybrid Nanofluid Flow over a Stretching Cylinder

4.1 Introduction

In current chapter flow and heat transfer features of alumina-copper/water (Al_2O_3-Cu/H_2O) hybrid nanofluid over stretching cylinder are explored under the impact of Lorentz force and thermal radiation. Roseland's flux model is employed for the impact of thermal radiation. Governing flow problem comprises of nonlinear partial differential equations which are converted into ordinary differential equations via appropriate similarity transforms, Boussinesq's and boundary layer approximations. Results for velocity, temperature, heat transfer rate and skin friction coefficient under influence of embedding parameters, are displayed and discussed through tables and graphs. A comparative analysis of hybrid nanofluid with base fluid and single material nanofluid is also made and found that hybrid nanofluid is extra effective in heat transfer than conventional fluid and single nanoparticle based nanofluid.

4.2 Geometry of Problem

We consider an incompressible, boundary layer and steady state flow of alumina-copper/water (Al_2O_3-Cu/H_2O) hybrid nanofluid. The physical model of stretching cylinder is employed. In flow schematic (x, r) coordinates are used to represent axial and radial directions. The externally applied magnetic field $\mathbf{B} = B_0 \hat{j}$ in the transverse direction is taken. The influences of mixed convection, thermal radiation, joule dissipation and viscous dissipation are also considered. The flow is initiated due to stretching of elastic cylinder in axial direction. The flow schematic, coordinates and geometrical variables are shown in figure. 4.1.

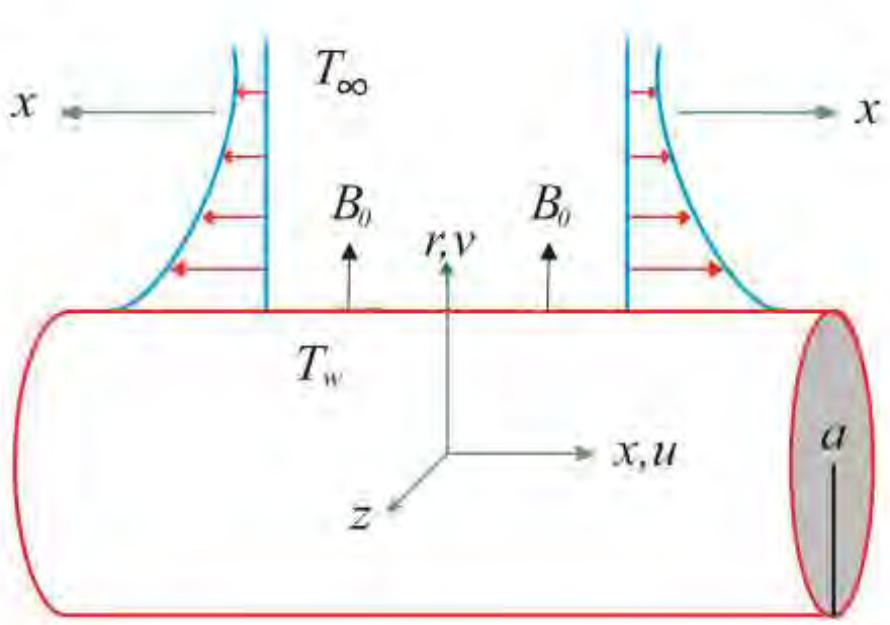

Figure 4.1: Flow schematic, coordinates and geometrical variables.

4.3 Mathematical Formulation

Under these physical suppositions, the laws of conservation of mass, momentum and energy under boundary layer approximations can be stated in the following forms:

$$\frac{\partial(ru)}{\partial x}+\frac{\partial(rv)}{\partial r}=0, \tag{4.1}$$

$$\rho_{hnf}\left(u\frac{\partial u}{\partial x}+v\frac{\partial u}{\partial r}\right)=\frac{\mu_{hnf}}{r}\frac{\partial}{\partial r}\left(r\frac{\partial u}{\partial r}\right)-\sigma B_0^2u+\left(\rho\beta\right)_{hnf}g\left(T-T_\infty\right), \tag{4.2}$$

$$\left(\rho c_p\right)_{hnf}\left(u\frac{\partial T}{\partial x}+v\frac{\partial T}{\partial r}\right)=\frac{k_{hnf}}{r}\frac{\partial}{\partial r}\left(r\frac{\partial T}{\partial r}\right)-\frac{\partial Q_r}{\partial r}+\mu_{hnf}\left(\frac{\partial u}{\partial r}\right)^2+\sigma B_0^2u^2, \tag{4.3}$$

associated with the following related boundary conditions:

$$\text{At}\quad r=a\quad u=cx,\ v=0,\ T=T_w, \tag{4.4}$$

$$\text{At}\quad r\to\infty\ u=0,\ \ T=T_\infty. \tag{4.5}$$

The Rosseland flux model [104] for the study of thermal radiation is as follows:

$$Q_r=-\frac{4\sigma^*}{3k^*}\frac{\partial T^4}{\partial r}, \tag{4.6}$$

Applying Taylor series to expand T^4 about T_∞ and omitting greater order terms, we obtained below forms:

$$T^4\cong 4T_\infty^3T-3T_\infty^4, \tag{4.7}$$

$$\frac{\partial Q_r}{\partial r} = -\frac{16\sigma^* T_\infty^3}{3k^*}\frac{\partial^2 T}{\partial r^2}. \tag{4.8}$$

For conversion of problem in dimensionless form, the subsequent similarity transforms are employed:

$$\eta = \frac{r^2 - a^2}{2a}\sqrt{\frac{c}{\nu}},\ u = cxf'(\eta),\ v = -\frac{a}{r}\sqrt{c\nu}\, f(\eta),\ \theta(\eta) = \frac{T - T_\infty}{T_w - T_\infty}, \tag{4.9}$$

using Eq. (4.9) in Eq. (4.1) to Eq. (4.5), the governing system of equations in dimensionless form is written as follows:

$$A_1\left(\left(1+2\eta\gamma\right) f''' + 2\gamma f''\right) + A_2\left(ff'' - f'^2\right) - Mf' + A_3\lambda\theta = 0, \tag{4.10}$$

$$\begin{aligned}\left(A_4 + Rd\right)\left(1+2\eta\gamma\right)\theta'' + \left(2A_4 + Rd\right)\gamma\theta' + EcPr\left\{Mf'^2 + A_1\left(1+2\eta\gamma\right) f''^2\right\} \\ + A_5 Prf\theta' = 0,\end{aligned} \tag{4.11}$$

$$f(0) = 0,\quad f'(0) = 1,\quad \theta(0) = 1, \tag{4.12}$$

$$f'(\infty) = 0,\quad \theta(\infty) = 0, \tag{4.13}$$

Various dimensionless parameters are arising in governing Eq. (4.10) to Eq. (4.11) like $\lambda = \frac{Gr}{Re_x^{\,2}}$ the convection parameter, $Re_x = \frac{cx^2}{\nu}$ the local Reynolds number, $Gr = \frac{g\tilde{\beta}\left(T_w - T_\infty\right)x^3}{\nu^2}$ the Grashof number, $Ec = \frac{u_w^2}{c_p\left(T_w - T_\infty\right)}$ the Eckert number, $M = \frac{\sigma B_0^2 a^2}{\mu_f}$ the magnetic parameter, $\gamma = \sqrt{\frac{\nu}{ca^2}}$ the curvature parameter, $Pr = \frac{\mu_f\left(c_p\right)_f}{k_f}$ the Prandtl number and $Rd = \frac{16\sigma^* T_\infty^3}{3k^* k_f}$ the radiation parameter.

The constant terms arising in above dimensionless equations are expressed as follows:

$$A_1 = \frac{\mu_{hnf}}{\mu_{bf}}, A_2 = \frac{\rho_{hnf}}{\rho_{bf}}, A_3 = \frac{\left(\rho\beta\right)_{hnf}}{\left(\rho\beta\right)_{bf}}, A_4 = \frac{k_{hnf}}{k_{bf}}, A_5 = \frac{\left(\rho c_p\right)_{hnf}}{\left(\rho c_p\right)_{bf}} \tag{4.14}$$

4.3.1 Hybrid Nanofluid Correlations

The correlations for effective density ρ_{hnf}, heat capacity $\left(c_p\right)_{hnf}$, thermal expansion coefficient β_{hnf}, thermal conductivity k_{hnf} and viscosity μ_{hnf} of hybrid-nanofluid appearing in the resulting equations are defined as:

$$\rho_{hnf} = \left(1-\varphi_{p2}\right)\left\{\left(1-\varphi_{p1}\right)\rho_f + \varphi_{p1}\rho_{p1}\right\} + \varphi_{p2}\rho_{p2}, \tag{4.15}$$

$$\mu_{hnf} = \mu_f \left(1-\varphi_{p1}\right)^{-2.5}\left(1-\varphi_{p2}\right)^{-2.5}, \tag{4.16}$$

$$\left(\rho c_p\right)_{hnf} = \left(1-\varphi_{p2}\right)\left\{\left(1-\varphi_{p1}\right)\left(\rho c_p\right)_f + \varphi_{p1}\left(\rho c_p\right)_{p1}\right\} + \varphi_{p2}\left(\rho c_p\right)_{p2}, \tag{4.17}$$

$$\left(\rho\beta\right)_{hnf} = \left(1-\varphi_{p2}\right)\left\{\left(1-\varphi_{p1}\right)\left(\rho\beta\right)_f + \varphi_{p1}\left(\rho\beta\right)_{p1}\right\} + \varphi_{p2}\left(\rho\beta\right)_{p2}, \tag{4.18}$$

$$\frac{k_{hnf}}{k_{bf}} = \frac{k_{p2} + \left(n-1\right)k_{bf} - \varphi_{p2}\left(n-1\right)\left(k_{bf}-k_{p2}\right)}{k_{p2} + \left(n-1\right)k_{bf} + \varphi_{p2}\left(k_{bf}-k_{p2}\right)}, \tag{4.19}$$

$$\frac{k_{bf}}{k_f} = \frac{\left(n-1\right)k_f + k_{p1} - \varphi_{p1}\left(n-1\right)\left(k_f-k_{p1}\right)}{\left(n-1\right)k_f + k_{p1} + \varphi_{p1}\left(k_f-k_{p1}\right)}. \tag{4.20}$$

Here the subscripts $p1$ and $p2$ are signifying Alumina (Al_2O_3) and copper (Cu) nanoparticles. Also φ is entire volume fraction, which is sum of volume fractions of two distinct nanoparticles (alumina and copper) suspended in carrier fluid to develop hybrid nanofluid. Mathematically it can be expressed as follows:

$$\varphi = \varphi_{p1} + \varphi_{p2}. \tag{4.21}$$

4.3.2 Physical Parameters of Interest

The essential physical quantities of practical and contemporary significance are the Nusselt number *Nu* and coefficient of skin friction C_f. The mathematical expressions can be expressed as follows:

$$C_f = \frac{2\tau_w}{\rho_{bf}u_w^2}, \text{ where } \tau_w = \mu_{hnf}\left(\frac{\partial u}{\partial r}\right)_{r=a}, \tag{4.22}$$

$$Nu = \frac{aQ_w}{k_{bf}\left(T_w - T_\infty\right)}, \text{ where } Q_w = -k_{hnf}\left(\frac{\partial T}{\partial r}\right)_{r=a}. \tag{4.23}$$

The dimensionless forms of Eq. (4.22) and Eq. (4.23) via similarity transformations defined in Eq. (4.9) are expressed as follows:

$$C_f\left(Re_x\right)^{0.5}=\frac{\mu_{hnf}}{\mu_{bf}}f''(0),\ Nu\left(Re_x\right)^{-0.5}=-2\left(\frac{k_{hnf}}{k_{bf}}\right)\theta'(0). \tag{4.24}$$

The thermophysical properties of nanoparticles and base fluid are defined in table 4.1.

Table 4.1: Physical properties of Water(H_2O), Alumina(Al_2O_3) and Copper(Cu)

	Physical property				
Water, Alumina and Copper particles	$\beta\times10^{-5}$ (K^{-1})	c_p $(Jkg^{-1}K^{-1})$	ρ (kgm^{-3})	k $(Wm^{-1}K^{-1})$	$\mu\times10^{-3}$ $(kgm^{-1}s^{-1})$
Alumina Al_2O_3	0.85	765	3970	40	-
Copper Cu	1.67	385	8933	400	-
Water H_2O	21	4179	997.1	0.613	0.894

4.4 Solution Procedure

The governing system ordinary differential equations Eq. (4.10) and Eq. (4.11) with appropriate set of boundary conditions is handled by a numerical integration technique Runge-Kutta-Fehlberg fourth-fifth order (RKF45) invoking shooting process. In this method, at first the resulting problem along with associated boundary conditions is transformed into system of 1st order equations. Let us assume

$$f=F_1,\ f'=F_2,\ f''=F_3,\ \theta=F_4,\ \theta'=F_5, \tag{4.25}$$

$$\begin{bmatrix}F_1'\\F_2'\\F_3'\\F_4'\\F_5'\end{bmatrix}=\begin{bmatrix}F_2\\F_3\\\dfrac{-1}{A_1\left(1+2\gamma\eta\right)}\left\{2A_1\gamma F_3+A_2\left(F_1F_3-F_2^{\,2}\right)+A_3\lambda F_4-MF_2\right\}\\F_5\\\dfrac{-1}{\left(A_4+Rd\right)\left(1+2\gamma\eta\right)}\left\{\begin{matrix}(2A_4+Rd)\gamma F_5+A_5PrF_1F_5+\\PrEc\left(A_1\left(1+2\gamma\eta\right)F_3^2+MF_2^2\right)\end{matrix}\right\}\end{bmatrix}, \tag{4.26}$$

$$F_1=0,\ F_2=1,\ F_3=s_3,\ F_4=1,\ F_5=s_5 \quad \text{at} \quad \eta=0. \tag{4.27}$$

Here the missing initial conditions are $F_3\left(0\right)=s_3$ and $F_5\left(0\right)=s_5$. Initially, the applicable initial guesses are picked which satisfies the boundary conditions. For achieving the convergence criteria of 10^{-5}, shooting approach is repeated such that no numerical oscillations would occur. The $\Delta\eta=0.01$ step-size is taken and the

selection of η_∞ varies from 2 to 5 depending upon the parameters.

4.5 Illustration of Results

For computing and comparing flow physiognomies and convective heat transfer performances of hybrid nanofluid, the most essential phase is the stable single/hybrid nanofluid preparation. There are two categories of nanofluids Alumina/water (Al_2O_3/H_2O) and Copper/water (Cu/H_2O) and then copper-alumina/water ($Cu–Al_2O_3/H_2O$) hybrid nanofluid is prepared for analysis. Numerical solutions derived in previous section allow us for the determination of behavior of dimensionless velocity, temperature distributions, skin friction coefficient and Nusselt number of manufactured copper-alumina/water ($Cu–Al_2O_3/H_2O$) hybrid nanofluid under the impact of various embedding parameters like particles concentration, magnetic parameter, Eckert number, curvature parameter, convection parameter and radiation parameter. The obtained results are represented in forms of figures and tables.

Figures 4.2 and 4.3 characterize the patterns of velocity and temperature distribution of Alumina-copper/water hybrid nanofluid and Alumina/water nanofluid and base fluid water. In figure 4.2, it is perceived that velocity profile is decreasing by dispersion of Alumina nanoparticles and more minimized due to hybrid nanomaterial. In figure 4.3, it is noticed that temperature profile of water is improved by dispersion of alumina nanoparticles in it and more improved when hybrid nanomaterial is used. Figures 4.4 and 4.5 describe the impact of magnetic parameter on velocity and temperature profiles of nanofluid and hybrid nanofluid. From figure 4.4, we have noted that the velocity profiles decrease by increasing magnetic parameter because magnetic field produces a Lorentz force which resists the fluid to flow. Figure 4.5 characterizes the impact of magnetic parameter on temperature distributions of nanofluid and hybrid nanofluid. It is noticed that the temperature distributions are increased by increasing values of the magnetic parameter due to increasing of frictional force between layers of fluid.

Figures 4.6 and 4.7 exhibit the impact of convection parameter on the velocity and temperature distributions of nanofluid as well as hybrid nanofluid. We conclude that the velocity and temperature profiles are improved by improving convection parameter. Figures 4.8 and 4.9 highlight the deviation of velocity and temperature

distribution of nanofluid and hybrid nanofluid versus curvature parameter. We found that the velocity and temperature profiles are improved by increasing curvature parameter. Figure 4.10 exhibits the impact of radiation parameter on temperature profiles of nanofluid and hybrid nanofluid. It is noticed that by enhancing radiation parameter the temperature profiles of nanofluid and hybrid nanofluid increases but hybrid nanofluid has greater magnitude as compared to nanofluid.

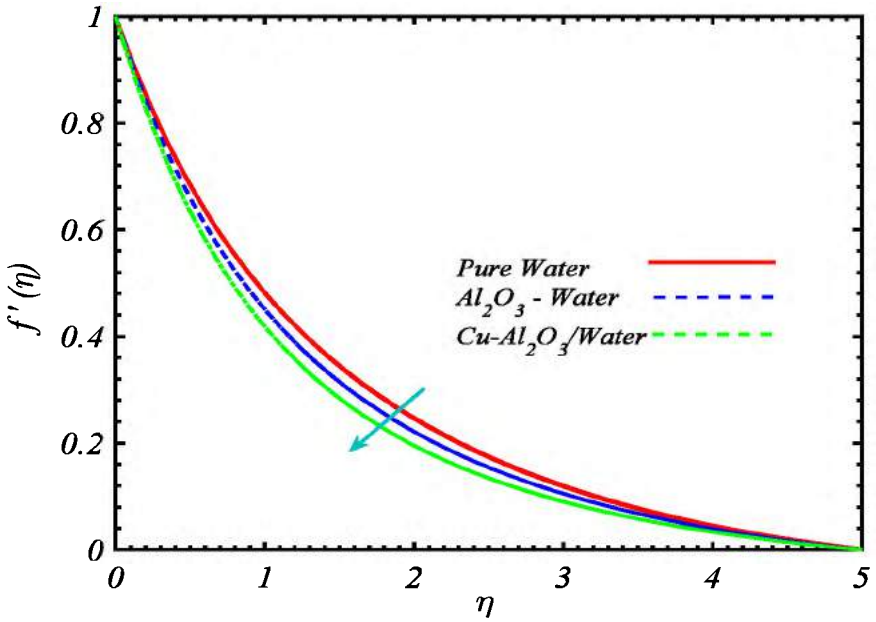

Figure 4.2: Flow profiles of single and hybrid nanofluid versus particles concentration.

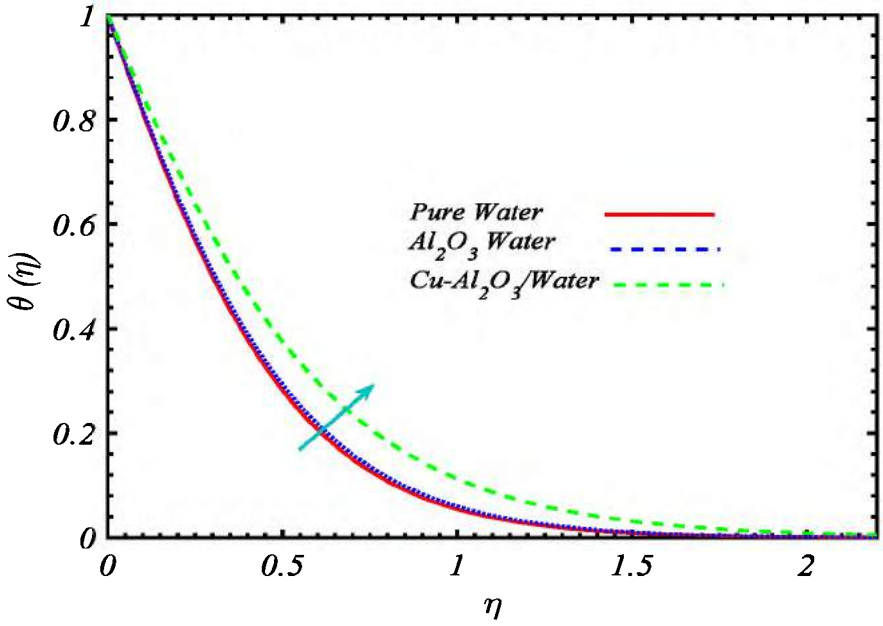

Figure 4.3: Thermal profiles of single and hybrid nanofluid versus particles concentration.

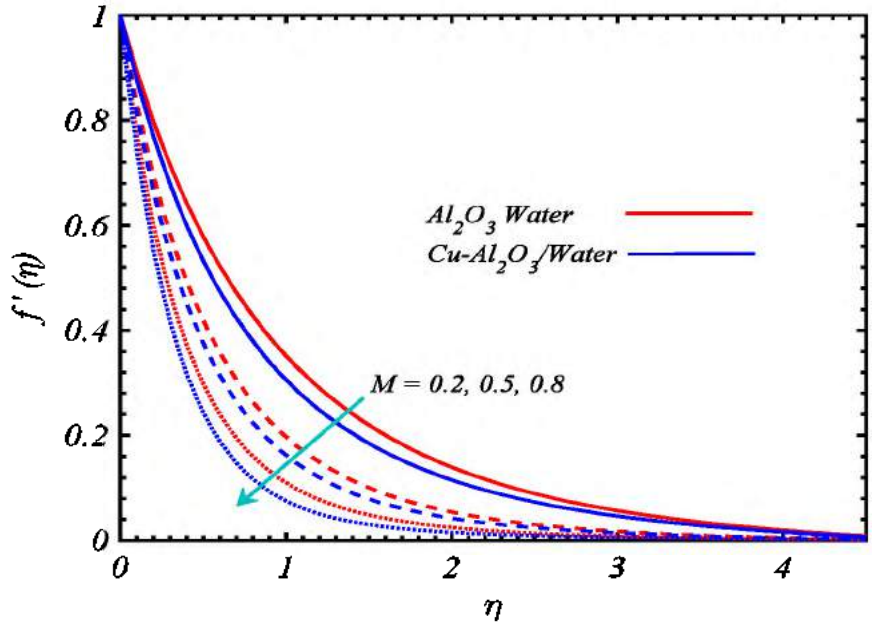

Figure 4.4: Flow profiles of single and hybrid nanofluid versus magnetic parameter.

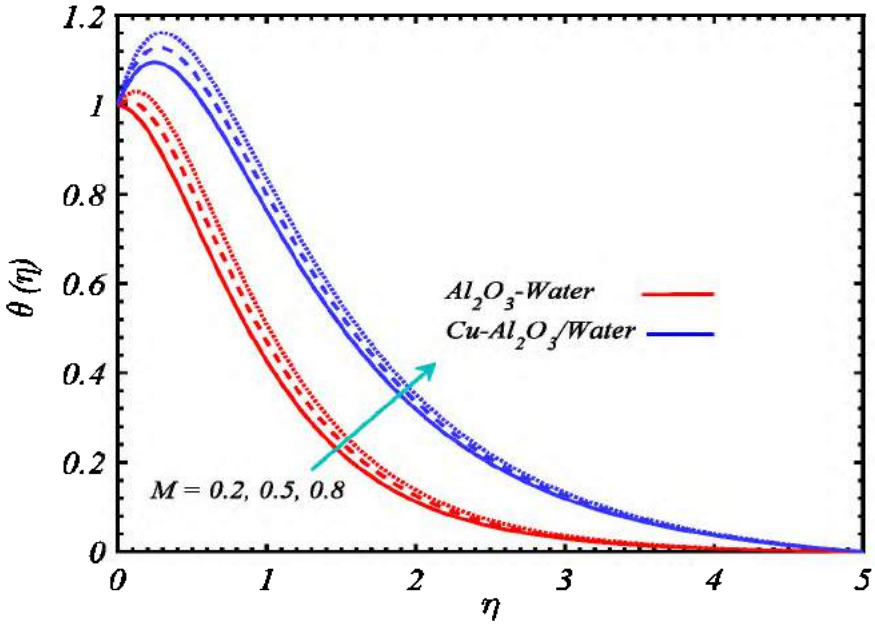

Figure 4.5: Thermal profiles of single and hybrid nanofluid versus magnetic parameter.

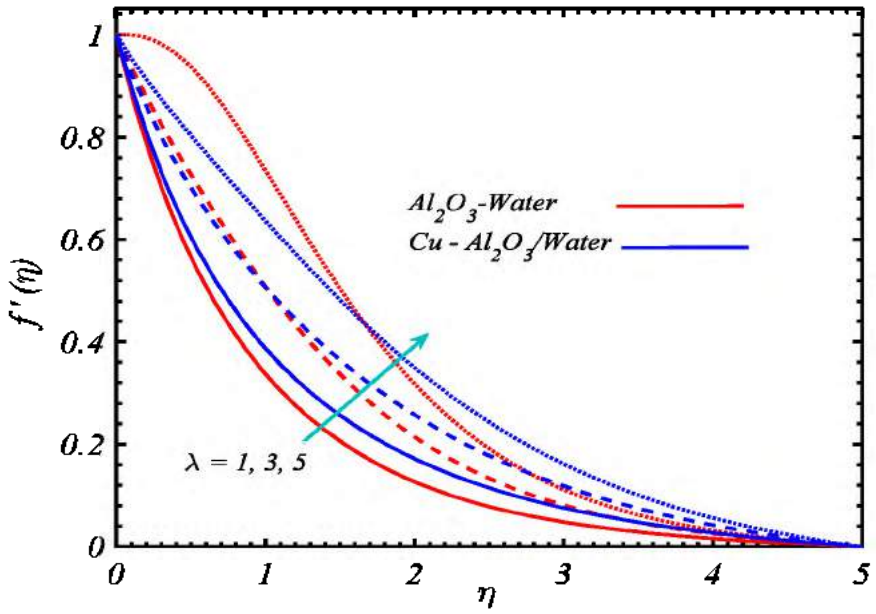

Figure 4.6: Flow profiles of single and hybrid nanofluid versus convection parameter.

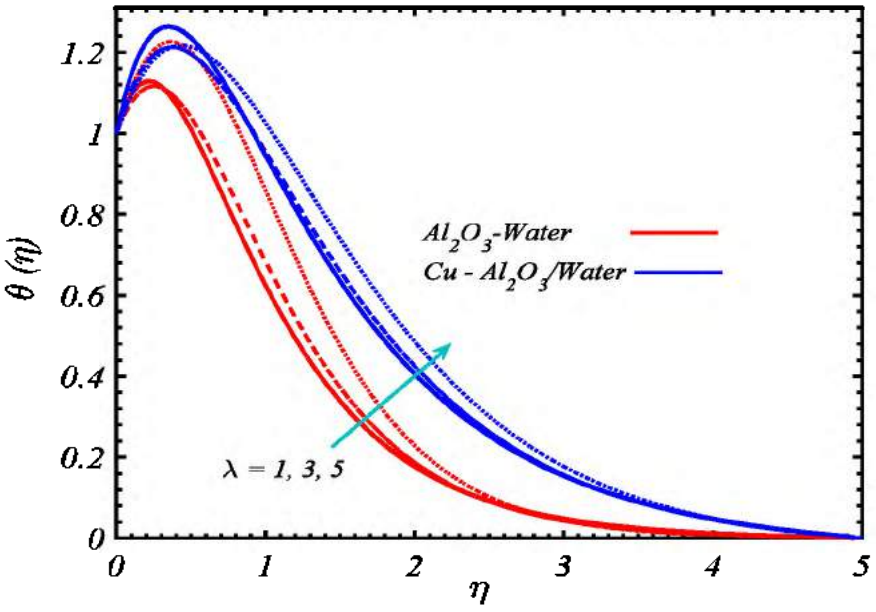

Figure 4.7: Thermal profiles of single and hybrid nanofluid versus convection parameter.

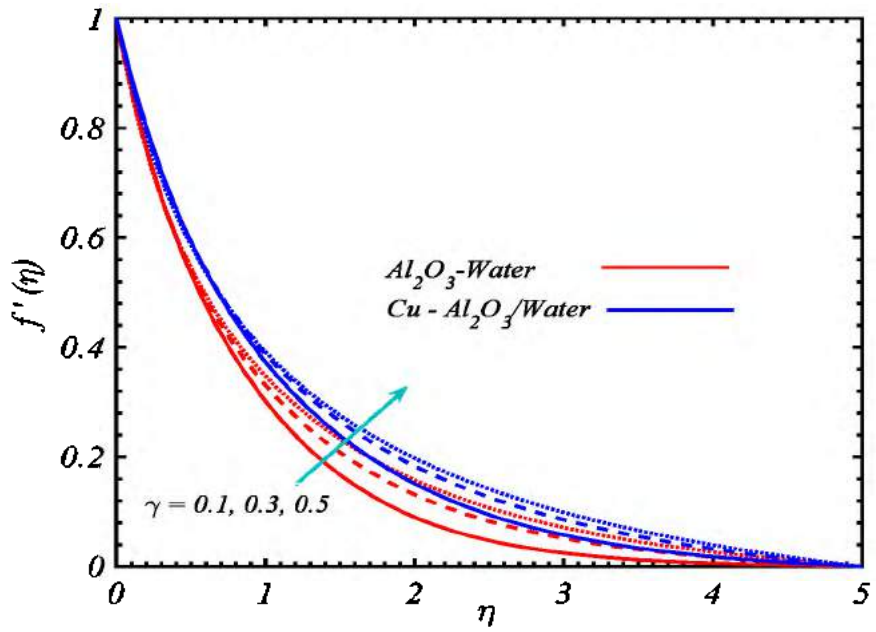

Figure 4.8: Flow profiles of single and hybrid nanofluid versus curvature parameter.

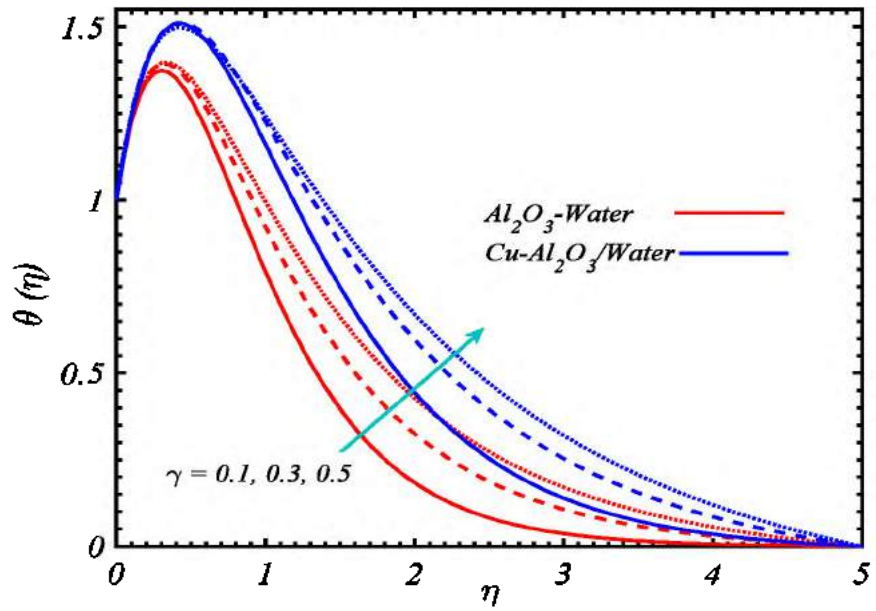

Figure 4.9: Thermal profiles of single and hybrid nanofluid versus curvature parameter.

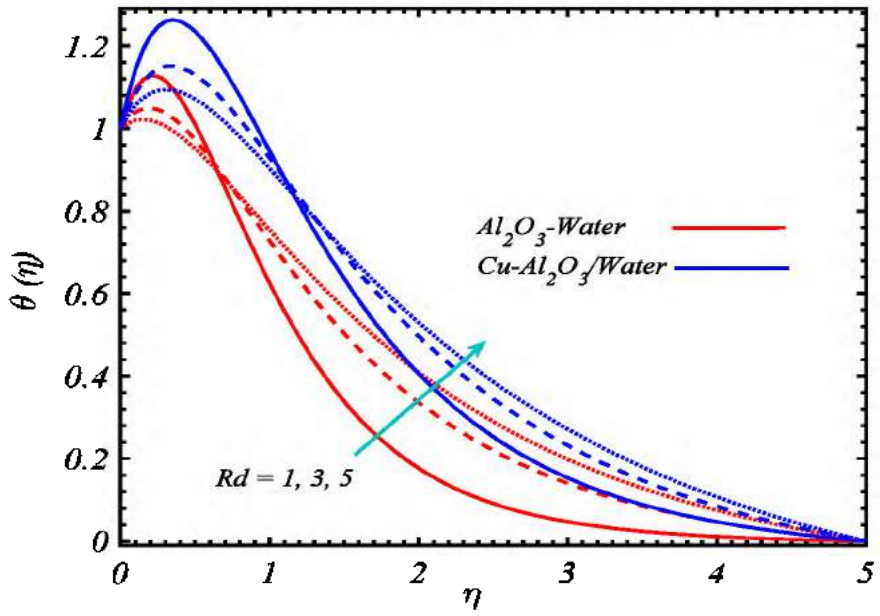

Figure 4.10: Thermal profiles of single and hybrid nanofluid versus radiation parameter.

In table 4.2, the numerically computed skin friction coefficient for numerous values of magnetic parameter, mixed convection parameter and curvature parameter are computed by keeping fixed parameters like; $Rd = 0.5, Ec = 0.2, \varphi_{p1} = 2\%, \varphi_{p2} = 3\%$. It is found that by increasing curvature parameter, the skin friction coefficient rises. On the other hand by increasing convection parameter, the value of skin friction coefficient decreases. When fluid layer is in contact with the surface of cylinder, it tries to be exerting a friction force on it. This friction force is more increased in concern of nanoparticle concentrations as presented in table 4.3. The highest wall shear stress at wall is observed in Cu/water due to much density and influence of other physical parameters. This wall shear stress is reduced for the case of hybrid nanofluid by composition of alumina nanoparticles. In table 4.4 the numerically computed values of Nusselt number are computed versus λ, Rd and Ec for numerous values of curvature parameter. For the computation of Nusselt number some parameters are kept fixed; $M = 0.5, \varphi_{p1} = 2\%, \varphi_{p2} = 3\%$. It is observed that by increasing radiation parameter and convection parameter, the values of Nusselt number increases. On the other hand by increasing curvature parameter and Eckert number, the value of Nusselt number decreases. Table 4.5 describes the results for heat transfer coefficient versus concentration of nanoparticles. The convection heat

transfer rate at every place on the surface of cylinder depends upon thermal conductivity and temperature gradient at the same location. Convective heat transfer coefficient is increased when thermal conductivity is quickly increased due to particle concentration improvement. Convective heat transfer is found minimum in case of copper/water nanofluid. Its convective heat transfer is enhanced by hybrid nanofluid through alumina nanoparticles composition.

Table 4.2: Computed numerical values of skin friction coefficient for various values of λ, M and γ, when $Rd = 0.5, Ec = 0.2, \varphi_{p1} = 2\%, \varphi_{p2} = 3\%$.

γ	λ	C_f (at $M = 0$)	C_f (at $M = 0.5$)	C_f (at $M = 1.0$)
0.0	0.5	0.8976	0.9557	1.0110
0.2		0.9756	1.0346	1.0908
0.3		1.0157	1.0748	1.1311
0.4		1.0562	1.1152	1.1716
0.2	0.0	1.0296	1.0897	1.1468
	0.5	0.9756	1.0346	1.0908
	0.8	0.9441	1.0023	1.0580
	1.0	0.9233	0.9811	1.0364

Table 4.3: Computed numerical values of skin friction coefficient via nanoparticles concentration, at fixed $Pr = 6.8, Rd = M = 0.5, Ec = \gamma = 0.2, \lambda = 1$

	Concentration	Alumina (Al_2O_3)	Copper (Cu)	-
Nanofluid	2%	0.9653	0.9982	-
	4%	0.9756	1.0374	-
	6%	0.9838	1.0707	-
	Concentration	Al_2O_3-Cu	Concentration	Al_2O_3-Cu
Hybrid Nanofluid	1% − 1%	0.9819	1.5% − 0.5%	0.9736
	2% − 2%	1.0069	3% − 1%	0.9914
	3% − 3%	1.0281	4.5% − 1.5%	1.0062

Table 4.4: Numerically computed Nusselt number (Nu) against λ, Rd, Ec and γ , at fixed $M = 0.5, \varphi_{np1} = 2\%, \varphi_{np2} = 3\%$.

λ	Rd	Ec	$Nu\left(\text{at } \gamma = 0\right)$	$Nu\left(\text{at } \gamma = 0.1\right)$	$Nu\left(\text{at } \gamma = 0.2\right)$
0.0	0.5	0.2	0.1653	0.0897	0.0198
0.3			0.2296	0.1609	0.0964
0.5			0.2703	0.2060	0.1448
0.8			0.3287	0.2704	0.2139
0.2	0.0	0.2	0.1312	0.0592	0.0225
	0.5		0.2086	0.1377	0.1036
	0.8		0.2387	0.1692	0.1372
	1.0		0.2544	0.1861	0.1555
0.2	0.5	0.0	1.9523	1.9867	2.0244
		0.05	1.5141	1.5219	1.5334
		0.1	1.0774	1.0588	1.0442
		0.15	0.6423	0.5974	0.5569

Table 4.5: Numerically computed Nusselt number Nu versus different nanoparticles concentration, at fixed $Pr = 6.8, Rd = Ec = 0.5, \lambda = \gamma = 0.2, M = 1$

	Concentration	Alumina (Al_2O_3)	Copper (Cu)	-
Nanofluid	2%	1.1776	1.0678	-
	4%	1.2302	1.1518	-
	6%	1.2811	1.2393	-
	Concentration	Al_2O_3-Cu	Concentration	Al_2O_3-Cu
Hybrid	1% − 1%	1.1232	1.5% − 0.5%	1.1506
Nanofluid	2% − 2%	1.1911	3% − 1%	1.2107
	3% − 3%	1.2602	4.5% − 1.5%	1.2707

Chapter 5

Hydromagnetic Transport of Iron Nanoparticles Aggregates Suspended in Water

5.1 Introduction

The current chapter is reported about the transport phenomenon of iron metal (*Fe*) nanoparticles aggregates suspended in water under the impact of external exerted magnetic field over a stretching cylinder. The governed problem is nonlinear coupled ordinary differential equations which are then tackled by Mathematica package Bvph 2.0 based on the homotopy scheme. The impact of chemical dimension (d_l), fractal dimension (d_f) and radius of gyration (R_g) on the flow and temperature profiles are presented via graphs. Numerical results of skin friction coefficient and heat transfer coefficient are computed for various involving parameters, presented in tabular form.

5.2 Geometry of Problem

Consider a steady two-dimensional mixed convective transport of *Fe* particle aggregations in water over a linearly stretching cylinder. The magnetic field $\mathbf{B} = (0, B_0, 0)$ is imposed in transverse direction.

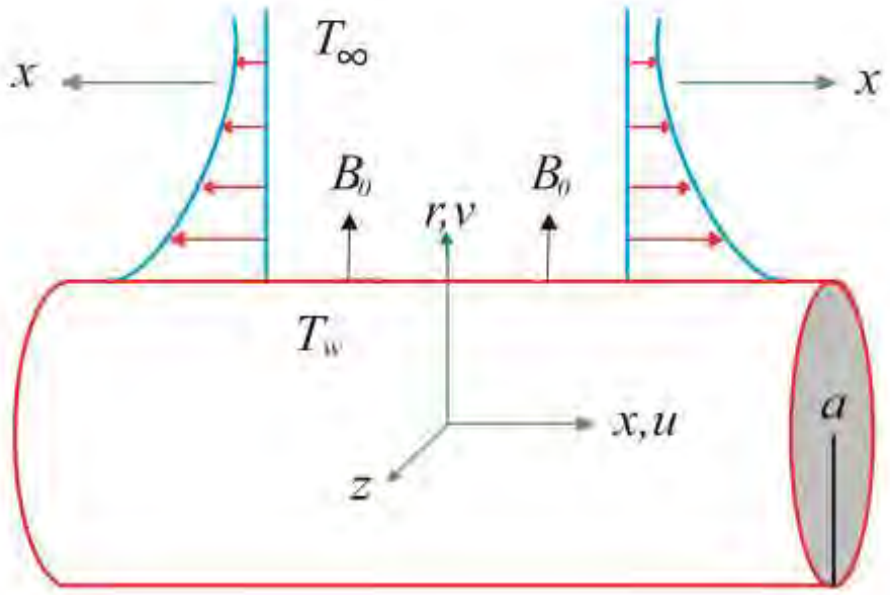

Figure. 5.1: Flow schematic, coordinates and geometrical variables.

The induced magnetic field is supposed to be negligible for low magnetic Reynolds number. The flow is originated by the linear stretching of cylinder with wall velocity $u_w(x) = cx$. The physical flow model and coordinate system are presented in figure 5.1.

5.3 Mathematical Formulation

The governing flow problem under the Boussinesq's and the boundary layer approximations can be expressed as follows:

$$\frac{\partial(ru)}{\partial x} + \frac{\partial(rv)}{\partial r} = 0, \tag{5.1}$$

$$\rho_{nf}\left(u\frac{\partial u}{\partial x} + v\frac{\partial u}{\partial r}\right) = \frac{\mu_{nf}}{r}\frac{\partial}{\partial r}\left(r\frac{\partial u}{\partial r}\right) - \sigma_{nf}B_o^2 u + (\rho\beta)_{nf}\, g(T - T_\infty), \tag{5.2}$$

$$(\rho c_p)_{nf}\left(u\frac{\partial T}{\partial x} + v\frac{\partial T}{\partial r}\right) = \frac{k_{nf}}{r}\frac{\partial}{\partial r}\left(r\frac{\partial T}{\partial r}\right) + \sigma_{nf}B_o^2 u^2. \tag{5.3}$$

The corresponding set of boundary conditions is below:

$$\left.\begin{array}{ll} u = cx,\ v = 0,\ T = T_w & \text{at } r = a \\ u = 0,\ T = T_\infty & \text{at } r \to \infty \end{array}\right\}. \tag{5.4}$$

To reduce the above governing equations in self-similar form, the below given similarity transformations are used:

$$\eta = \frac{r^2 - a^2}{2a}\sqrt{\frac{c}{\nu}},\ u = cxf'(\eta),\ v = -\frac{a}{r}\sqrt{c\nu}\, f(\eta),\ \theta = \frac{T - T_\infty}{T_w - T_\infty}, \tag{5.5}$$

substituting Eq. (5.5) in Eqs. (5.1) to Eq. (5.4), the self-similar form is expressed as follows:

$$\frac{\mu_{nf}}{\mu_f}\left\{(1 + 2\eta\gamma)f''' + 2\gamma f''\right\} + \frac{\rho_{nf}}{\rho_f}\left(ff'' - f'^2\right) + \frac{(\rho\beta)_{nf}}{(\rho\beta)_f}\lambda\theta - \frac{\sigma_{nf}}{\sigma_f}Mf' = 0, \tag{5.6}$$

$$\frac{k_{nf}}{k_f}\left\{(1 + 2\eta\gamma)\theta'' + 2\gamma\theta'\right\} + \frac{(\rho c_p)_{nf}}{(\rho c_p)_f}Prf\theta' + \frac{\sigma_{nf}}{\sigma_f}MEcf'^2 = 0, \tag{5.7}$$

the dimensionless form of boundary condition is written as follows:

$$\left.\begin{array}{ll} f(0) = 0,\ f'(0) = \theta(0) = 1 & \text{at } \eta = 0 \\ f'(\infty) = \theta(\infty) = 0 & \text{at } \eta \to \infty \end{array}\right\}. \tag{5.8}$$

The sundry parameters appearing in above equations are formulated as follows:

$$\left.\begin{aligned} M=\frac{\sigma_f B_0^2}{\rho c},\ \gamma=\sqrt{\frac{\mu_f}{\rho_f c a^2}}, Pr=\frac{\mu_f}{k_f\left(c_p\right)_f},\ \lambda=\frac{Gr}{Re^2}, \\ Gr=\frac{g\beta_f\left(T_w-T_\infty\right)x^3}{{\nu_f}^2}, Re=\frac{u_w x}{\nu_f},\ Ec=\frac{u_w^2}{\left(c_p\right)_f\left(T_w-T_\infty\right)} \end{aligned}\right\}. \tag{5.9}$$

5.3.1 Nanofluid Correlations

Nanoparticles suspended in liquid would move in form of aggregations that produced significant influence on physical properties of carrier fluid. The correlations for the properties of nanofluid under effect of aggregation are defined as [83]:

$$\left(\rho c_p\right)_{nf}=\varphi_a\left(\rho c_p\right)_a+\left(1-\varphi_a\right)\left(\rho c_p\right)_f, \tag{5.10}$$

$$\left(\rho\beta\right)_{nf}=\varphi_a\left(\rho\beta\right)_a+\left(1-\varphi_a\right)\left(\rho\beta\right)_f, \tag{5.11}$$

$$\rho_{nf}=\varphi_a\rho_a+\left(1-\varphi_a\right)\rho_f, \tag{5.12}$$

$$\mu_{nf}=\mu_f\left(1-\frac{\varphi_a}{\varphi_{max}}\right)^{-2.5\varphi_{max}}, \tag{5.13}$$

$$\sigma_{nf}=\frac{2\sigma_f+\sigma_a+2\varphi_a\left(\sigma_a-\sigma_f\right)}{2\sigma_f+\sigma_a-\varphi_a\left(\sigma_a-\sigma_f\right)}\sigma_f, \tag{5.14}$$

$$k_{nf}=\frac{2k_f+k_a+2\varphi_a\left(k_a-k_f\right)}{2k_f+k_a-\varphi_a\left(k_a-k_f\right)}k_f. \tag{5.15}$$

In aggregations, physical properties are calculated through following models:

$$\rho_a=\varphi_{int}\rho_p+\left(1-\varphi_{int}\right)\rho_f, \tag{5.16}$$

$$\beta_a=\varphi_{int}\beta_p+\left(1-\varphi_{int}\right)\beta_f, \tag{5.17}$$

$$\left(c_p\right)_a=\varphi_{int}\left(c_p\right)_p+\left(1-\varphi_{int}\right)\left(c_p\right)_f. \tag{5.18}$$

Nanoparticles dispersed in base fluid would aggregate with each other to produce chain structure. Linear chains which span the entire aggregate are known as backbone and rest of the particles are termed as dead end particles. The backbone shows a prominent part in rheology of colloids because it can transfer elastic forces within aggregate. Figure 5.2 shows schematic of independent single aggregate which contains the backbone and dead-end particles.

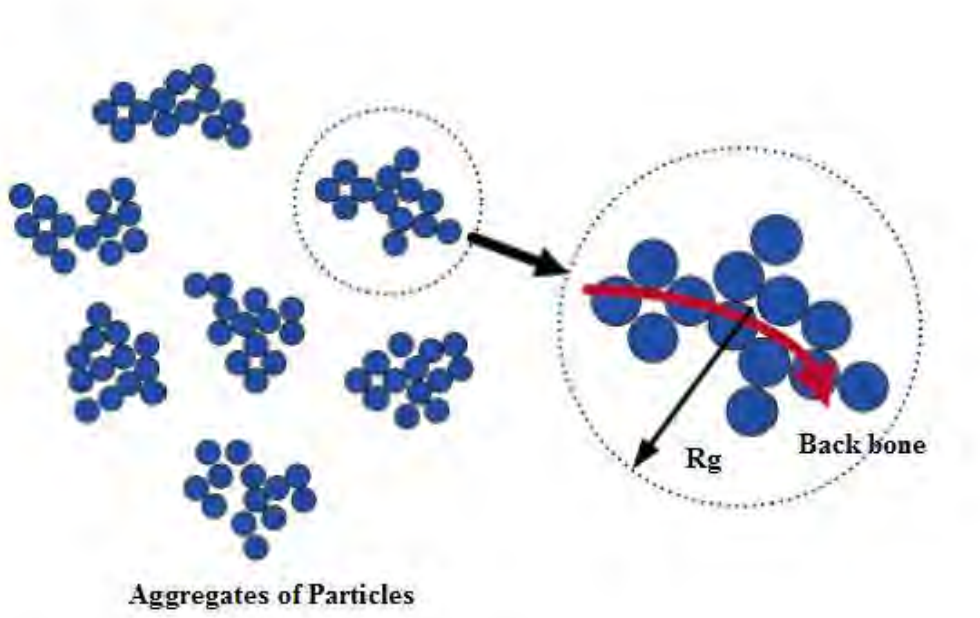

Figure. 5.2: Aggregations of nanoparticles

For further understanding the effect of aggregation on fluid properties the thermal conductivity of the aggregate due to dead end particles is evaluated via Bruggeman model [112]:

$$\frac{\varphi_{nc}\left(k_s-k_{nc}\right)}{\left(k_s+2k_{nc}\right)}+\frac{\left(1-\varphi_{nc}\right)\left(k_f-k_{nc}\right)}{\left(k_f+2k_{nc}\right)}=0, \tag{5.19}$$

we employed the model suggested by Nan et al. [113] for randomly oriented cylindrical particles. In his model, the correlation for effective thermal conductivity of aggregate sphere k_a is given by:

$$\frac{k_a}{k_{nc}}=\frac{3+\varphi_c\left\lfloor\beta_{33}\left(1-M_{33}\right)+2\beta_{11}\left(1-M_{11}\right)\right\rfloor}{3-\varphi_c\left[\beta_{33}M_{33}+2\beta_{11}M_{11}\right]}, \tag{5.20}$$

Here

$$\left.\begin{aligned} M_{11}&=\frac{e^2}{2\left(e^2-1\right)}-\frac{e\cosh^{-1}e}{2\left(e^2-1\right)^{1.5}},\\ M_{33}&=1-2M_{11}\ \text{and}\ \beta_{ii}=\frac{\left(k_{ii}^c-k_{nc}\right)}{\left[k_{nc}-M_{ii}\left(k_{ii}^c-k_{nc}\right)\right]}, \end{aligned}\right\}, \tag{5.21}$$

The term which interprets the interfacial resistance is given by:

$$k_{ii}^c=\frac{k_s}{\left(1+\tilde{\gamma}M_{ii}k_s/k_f\right)}, \tag{5.22}$$

The terms in above Eq. (5.22) are given below:

$$\tilde{\gamma} = \left(2 + \frac{1}{e}\right)\tilde{\alpha}, \text{ here } \tilde{\alpha} = \frac{A_k}{a^*}, e = \frac{R_g}{a^*} \Bigg\}, \tag{5.23}$$

Here A_k is Kapitza radius which represents the thickness of matrix over which the temperature drop in planar geometry is similar as at the interface. The number of particles within aggregation in terms of fractal dimensions can be formulated as follows:

$$N_{int} = \left(\frac{R_g}{a^*}\right)^{d_f}, \tag{5.24}$$

For $\varphi_a = 1$, we can find that:

$$\varphi_{\text{int}} = \left(\frac{R_g}{a^*}\right)^{1/d_f - 3}, \quad \left(\frac{R_g}{a^*}\right)_{max} = \varphi^{1/d_f - 3} \tag{5.25}$$

The number of particles which belong to backbone N_c in terms of chemical dimensions can be correlated as follows:

$$N_c = \left(\frac{R_g}{a^*}\right)^{d_l}, \tag{5.26}$$

The concentration of backbone particles φ_c and dead ends particles φ_{nc} can be written as follows:

$$\varphi_c = \left(\frac{R_g}{a^*}\right)^{d_l - 3}, \text{ where } \varphi_{nc} = \varphi_{\text{int}} - \varphi_c. \tag{5.27}$$

5.3.2 Physical Parameters of Interest

The parameters of physical and practical importance are given below:

$$C_f = \frac{2\tau_w}{\rho u_w^2}, \quad Nu = \frac{aQ_w}{k_f\left(T_w - T_\infty\right)}, \tag{5.28}$$

here τ_w and Q_w are given by:

$$\tau_w = \mu_{nf}\left(\frac{\partial u}{\partial r}\right)_{r=a}, \; Q_w = -k_{nf}\left(\frac{\partial T}{\partial r}\right)_{r=a}, \tag{5.29}$$

applying similarity transformation defined in Eq. (5.5), the dimensionless form of C_f and Nu can be written as:

$$C_f\left(Re_x\right)^{0.5} = 2\frac{\mu_{nf}}{\mu_f} f''(0),\ Nu\left(Re_x\right)^{-0.5} = -\frac{k_{nf}}{k_f}\theta'(0). \tag{5.30}$$

5.4 Solution Procedure

The nonlinear ordinary differential Eq. (5.6) and Eq. (5.7) are tackled by using homotopy based Mathematica package Bvph 2.0. The solutions of velocity and temperature distributions can be expressed explicitly by an infinite series of the subsequent form:

$$f_i(\eta) = \sum_{m=0}^{\infty} f_{i,m}(\eta),\ \theta_i(\eta) = \sum_{m=0}^{\infty} \theta_{i,m}(\eta), \tag{5.31}$$

Where $f_i(\eta)$ and $\theta_i(\eta)$ are governed by the Eq. (5.6) and Eq. (5.7), which are linear and depend upon the auxiliary linear operator. The appropriate selection of initial guess, the auxiliary linear operator and the auxiliary function is requisite for convergence of homotopy series. In current flow problem the auxiliary linear operators are taken as below:

$$£_1(f) = \frac{d^3 f}{d\eta^3} + \frac{d^2 f}{d\eta^2},\ £_2(\theta) = \frac{d^2\theta}{d\eta^2} + \frac{d\theta}{d\eta}, \tag{5.32}$$

The initial guesses satisfying the corresponding boundary conditions Eq. (5.8) are chosen as below:

$$f_0(\eta) = 1 - e^{-\eta},\ \theta_0(\eta) = e^{-\eta}, \tag{5.33}$$

The error of the two successive approximations over [0, 1] at 20th iterations are given as follows:

$$E_f = \sqrt{\frac{1}{21}\sum_{i=0}^{15}\left(f\left(\frac{i}{20}\right)\right)^2} \tag{5.34}$$

$$E_\theta = \sqrt{\frac{1}{21}\sum_{i=0}^{15}\left(\theta\left(\frac{i}{20}\right)\right)^2} \tag{5.35}$$

The results for velocity, temperature profiles, sink friction coefficient and Nusselt numbers for various involving parameters are obtained at 20th iteration.

5.5 Illustration of Results

The three level homogenization model is used to understand the fractal morphology of nanoparticles. For homogenization theory, we used parameters matching those describing the model fractal aggregates including $d_l = 1.4,\ d_f = 1.8,\ R_g = 100$ and zero interfacial thermal resistance. The outcomes of the homogenization theory and Monte Carlo simulations validated very well with all volume fractions and across the whole range of aggregate sizes. The particles aggregations dynamics is reflected through the radius of gyration, fractal dimension and chemical dimensions. Influences of various involved parameters on flow and temperature distributions, Nusselt number and skin friction coefficient are displayed in graphical and tabular form. For evaluation of results, some parameters are fixed throughout like $Re = 897, Ec = 2.39\times10^{-9}, M = 0.5, \gamma = 0.03, Pr = 7.0, \lambda = 0.1$

The impact of fractal dimension d_f on flow and temperature distributions is demonstrated in figures 5.3 and 5.4. In figure 5.3, it is perceived that the velocity distribution is improved by enhancing fractal dimensions. This is due to declination of particles in backbone as compare to dead ends particles which our come to a resistance in fluid flow. It can also be visualized that velocity is declined by growing the volume fraction of nanoparticles. In figure 5.4, it is noted that by increasing fractal dimensions the temperature of nanofluid is decreased. Due to declination in thermal conduction corresponding to enhancement in numbers of dead-end particles, temperature is reduced. In addition, temperature distribution is improved by improving the nanoparticles volume fraction. Figures 5.5 and 5.6 are plotted to view the impact of chemical dimension on velocity and temperature profiles. It can be visualized that the velocity distribution is dropped down by increasing the chemical dimension in figure. 5.5. Because the numbers of particles are aggregated in backbone which makes a resistance in flow distribution. On the other hand, the temperature distribution is improved by improving the value of chemical dimension in figure. 5.6. It is happening in consequence of enhancement in thermal conductivity by improving backbone chain. The impact of gyration radius on velocity and temperature distribution is revealed through figures. 5.7 and 5.8. In these figures the velocity profile is decreased by enhancing the gyration radius, but opposite behavior is noted in temperature profile. These figures are prepared by taken fixed dead ends and back bone's particles. In consequence of gyration radius increment, length of backbone

chain is increased that produces resistance in flow but this play important role to improve the thermal conduction.

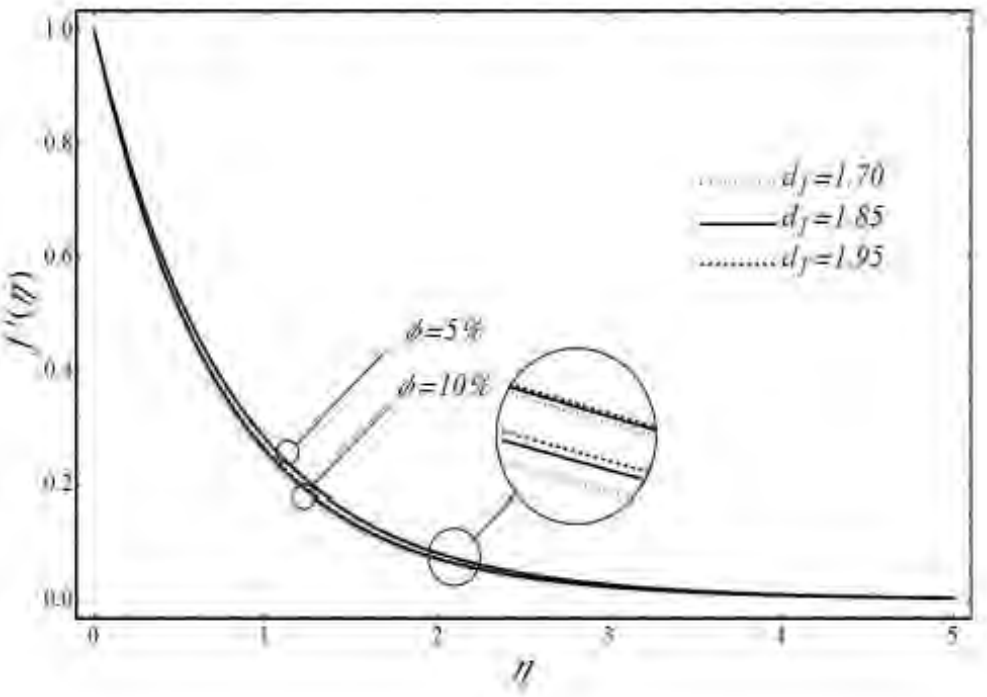

Figure 5.3: Velocity distribution versus fractal dimensions d_f.

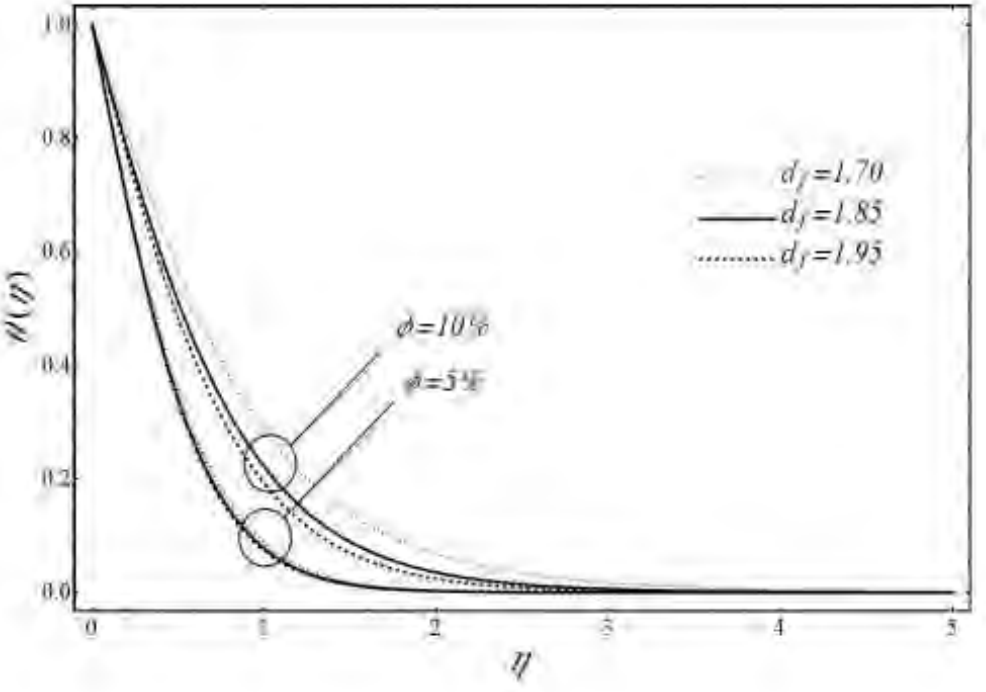

Figure 5.4: Temperature distribution versus fractal dimensions d_f.

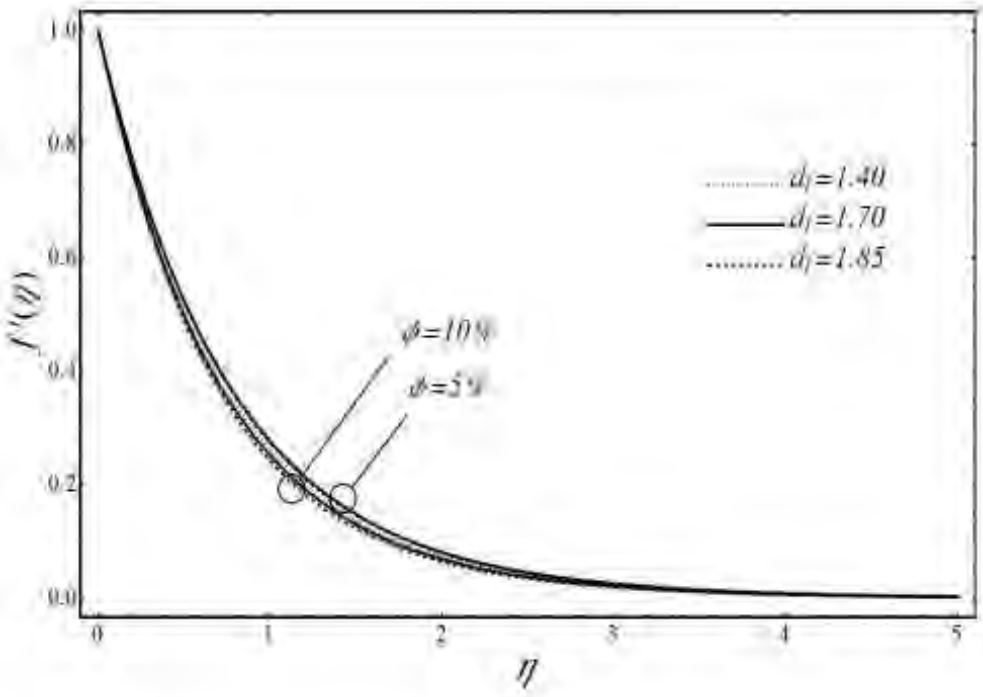

Figure 5.5: Velocity distribution versus chemical dimensions d_l .

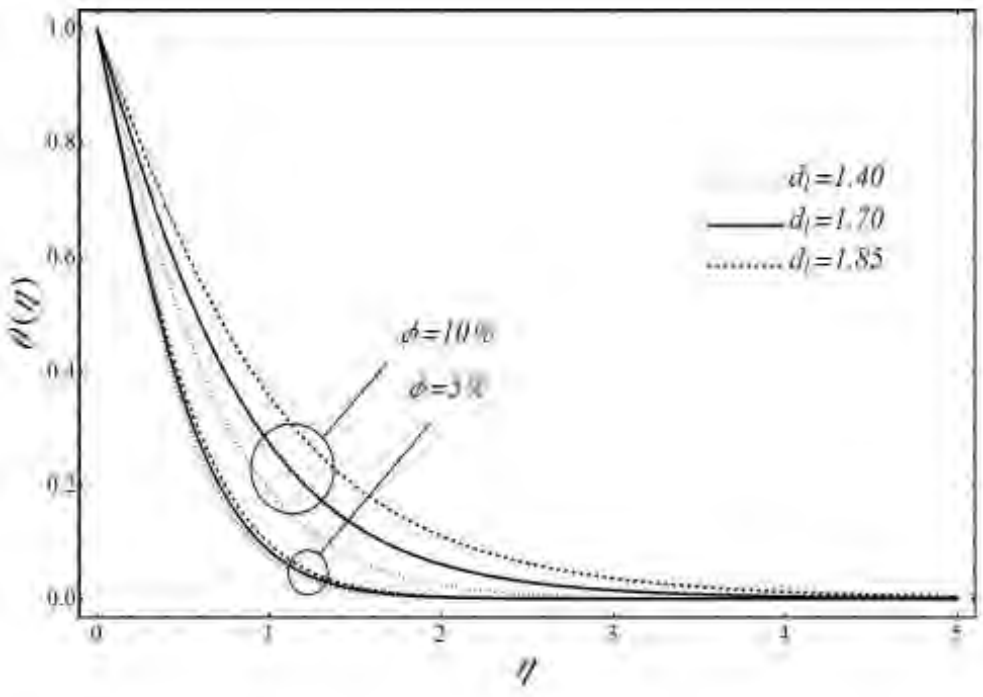

Figure 5.6: Temperature distribution versus chemical dimensions d_l .

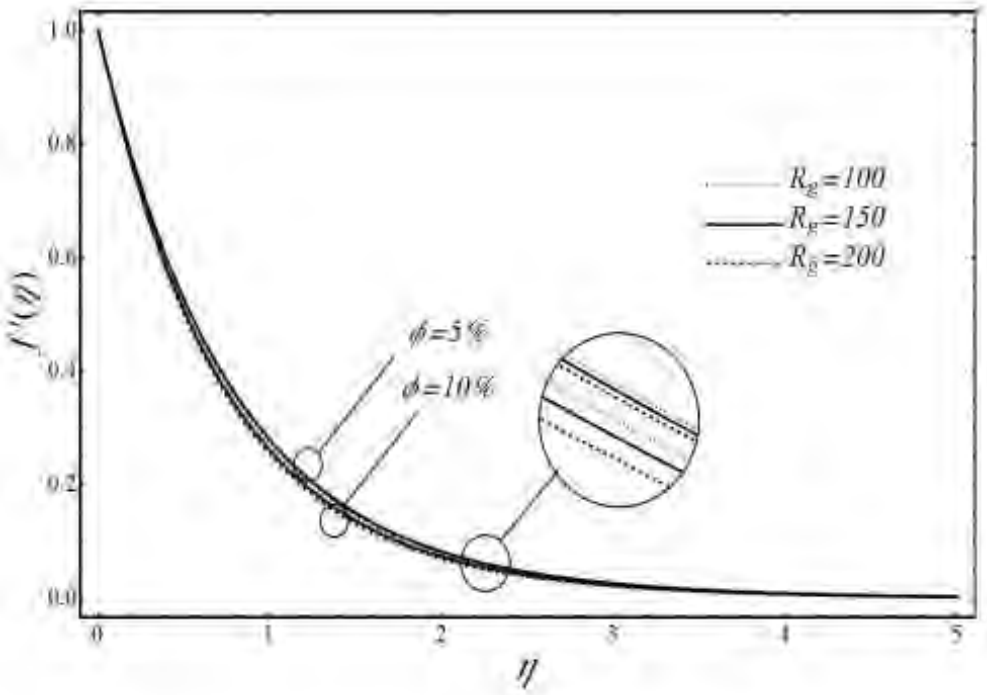

Figure 5.7: Velocity distribution versus radius of gyration R_g

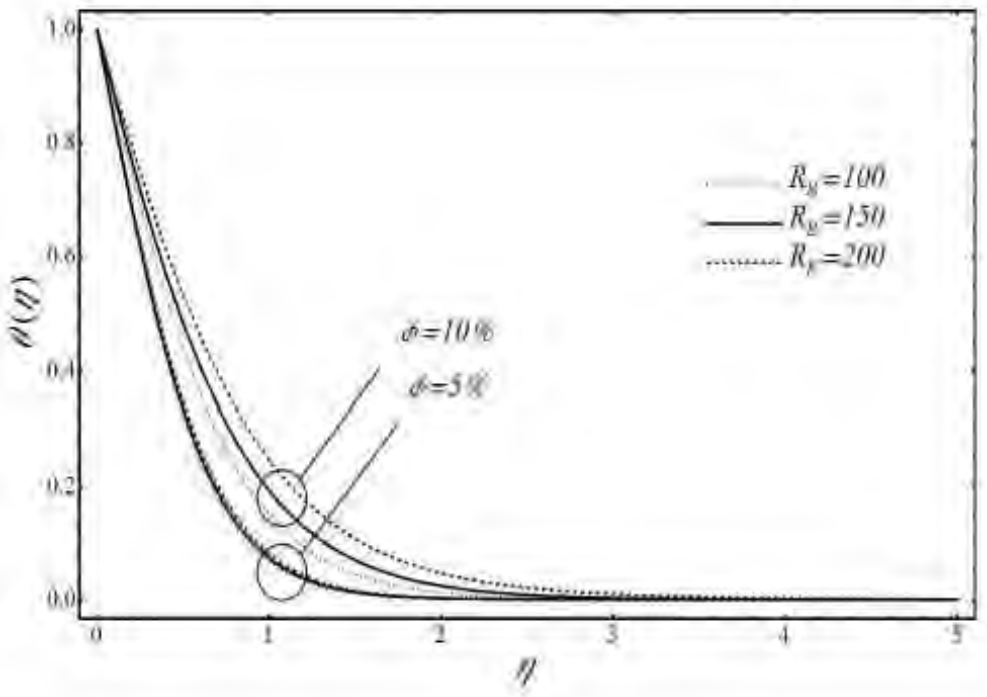

Figure 5.8: Temperature distribution versus radius of gyration R_g .

In table 5.1 the numerical values are computed to show impact of the fractal dimension, chemical dimensions and radius of gyration at different nanoparticles concentration on skin friction coefficient and Nusselt number. This table depicts that

shear stress on wall and convection heat transfer is enhanced by enhancing nanoparticles concentrations. In enhancement of heat transfer, thermal conductivity plays an important role that is improved by improving particles concentration. On the other hand, viscosity becomes the main cause of cumulating in shear stress insignificance of particles concentration enhancement. In this table, it can be analyzed that convection heat transfer, as well as wall shear stress, is little bit decreased when dead-end particles are increased in consequence of fractal dimension. Alternatively, when dead-end particles are reduced and backbones particles are increased, convective heat transfer and wall shear stress are increased. It can also be perceived that convection heat transfer and wall shear stress has same behavior as chemical dimensions.

Table 5.1: Numerical values of heat transfer rate and skin friction coefficient.

φ	d_f	d_l	R_g	$-\theta'(0)$	$-f''(0)$
0%	1.85	1.45	15	1.83258	2.42750
5%				1.96859	2.95653
10%				2.10685	3.53064
5%	1.70	1.45	15	2.00989	2.97461
	1.85			1.96859	2.95653
	1.95			1.94859	2.94809
5%	1.95	1.45	15	1.94859	2.94809
		1.70		2.00216	2.97058
		1.85		2.05287	2.99246
5%	2.3	1.69	10	1.91758	2.93192
	1.95	1.45	15	1.94859	2.94809
	1.76	1.30	20	1.98337	2.96806

Chapter 6

Hydromagnetic Nanofluid Flow past a Stretching Cylinder Embedded in Non-Darcian Forchheimer Porous Media

6.1 Introduction

The present chapter presents the hydromagnetic nanofluid flow past over a stretching cylinder in non-Darcian Forchheimer porous medium. Thermal radiation via Roseland's approximation, Brownian motion, thermophoresis and Joule heating effects are also incorporated. To explore thermal characteristics prescribed heat flux (PHF) and prescribed concentration flux (PCF) boundary conditions are deployed. Governing flow problem consists of partial differential equations in cylindrical form, which is converted into system of nonlinear ordinary differential equations by applying applicable similarity transforms. Governing equations are tackled by Runge-Kutta-Fehlberg fourth-fifth order numerical integration scheme along with shooting algorithm. Impact of numerous involving physical parameters on flow features like temperature distribution, velocity distribution, Sherwood number, local Nusselt number and skin friction coefficient are shown in graphical and tabular form.

6.2 Geometry of Problem

Let us assume a steady two-dimensional boundary layer flow of nanofluid past a stretching cylinder embedded in non-Darcy Forchheimer porous media. The cylindrical polar coordinates x and r are taken in axial and the radial directions. The external magnetic field B_0 is applied in transverse direction. The impact of pressure gradient and flow is caused due to linear stretching of cylinder with stretching wall velocity $u_w = cx$. The geometry and coordinate system of current flow problem are described in figure. 6.1.

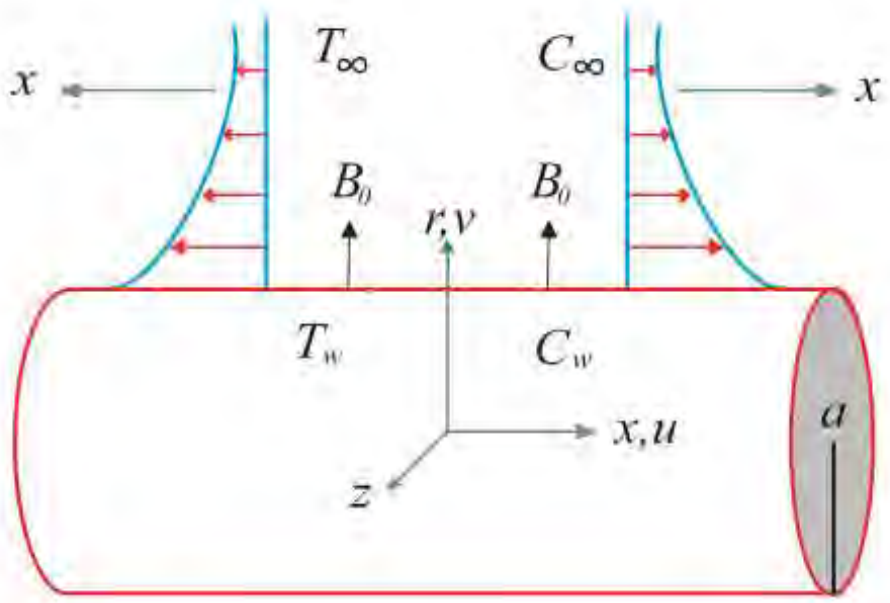

Figure 6.1: Flow schematic, coordinates and geometrical variables.

6.3 Mathematical Formulation

Under the above mentioned conditions, the current flow problem can be represented as follows:

$$\frac{\partial}{\partial x}(ru)+\frac{\partial}{\partial r}(rv)=0, \tag{6.1}$$

$$u\frac{\partial u}{\partial x}+v\frac{\partial u}{\partial r}=\frac{\nu}{r}\frac{\partial}{\partial r}\left(r\frac{\partial u}{\partial r}\right)-\frac{\nu}{k_1}u-\frac{C_b}{\sqrt{k_1}}u^2-\frac{\sigma B_0^2}{\rho}u, \tag{6.2}$$

$$u\frac{\partial T}{\partial x}+v\frac{\partial T}{\partial r}=\frac{\overline{\alpha}}{r}\frac{\partial}{\partial r}\left(r\frac{\partial T}{\partial r}\right)+\tau\left\{D_B\frac{\partial C}{\partial r}\frac{\partial T}{\partial r}+\frac{D_T}{T_\infty}\left(\frac{\partial T}{\partial r}\right)^2\right\}+\frac{\sigma B_0^2u^2}{(\rho c)_f}-\frac{1}{(\rho c)_f}\frac{\partial Q_r}{\partial r}, \tag{6.3}$$

$$u\frac{\partial C}{\partial x}+v\frac{\partial C}{\partial r}=\frac{D_B}{r}\frac{\partial}{\partial r}\left(r\frac{\partial C}{\partial r}\right)+\frac{D_T}{T_\infty}\frac{1}{r}\frac{\partial}{\partial r}\left(r\frac{\partial T}{\partial r}\right). \tag{6.4}$$

The following appropriate boundary conditions are employed:

$$\text{At}\quad r=a\;\; u=u_w=cx,\; v=0,\;\; -k\left(\frac{\partial T}{\partial r}\right)=T_w,\;\; -D_B\left(\frac{\partial C}{\partial r}\right)=C_w, \tag{6.5}$$

$$\text{At}\quad r\to\infty\quad u=0,\; T=T_\infty,\; C=C_\infty. \tag{6.6}$$

The radiation flux model offered by Roseland's can be written as:

$$Q_r = -\frac{4\sigma^*}{3k^*}\frac{\partial T^4}{\partial r}, \tag{6.7}$$

by expanding Taylor series of T^4 about T_∞ and retaining linear terms, we attain the following form:

$$T^4 \cong 4T_\infty^3 T - 3T_\infty^4, \tag{6.8}$$

$$\frac{\partial Q_r}{\partial r} = -\frac{16\sigma^* T_\infty^3}{3k^*}\frac{\partial^2 T}{\partial r^2}. \tag{6.9}$$

To reduce the problem in similar form, the below mentioned suitable similarity transformations are applied:

$$\left.\begin{aligned} &\eta = \frac{r^2 - a^2}{2a}\sqrt{\frac{c}{\nu}},\ u = cxf'(\eta),\ v = -\frac{a}{r}\sqrt{c\nu}\, f(\eta) \\ &T = T_\infty + \frac{T_w}{k}\sqrt{\frac{\nu}{c}}\theta(\eta),\ C = C_\infty + \frac{C_w}{D_B}\sqrt{\frac{\nu}{c}}\phi(\eta) \end{aligned}\right\}, \tag{6.10}$$

the governing problem in non-dimensional form can be described as follows:

$$(1+2\eta\gamma) f''' + 2\gamma f'' - (1+F^*) f'^2 + ff'' - (M^2 + K^*) f' = 0, \tag{6.11}$$

$$\begin{aligned} \frac{1}{Pr}\Big[(1+2\eta\gamma)\{(1+Rd)\theta'' + PrNb\phi'\theta' + PrNt\theta'^2\} + \gamma(2+Rd)\theta'\Big] \\ + M^2 Ecf'^2 + f\theta' = 0, \end{aligned} \tag{6.12}$$

$$(1+2\eta\gamma)\phi'' + 2\gamma\phi' + (1+2\eta\gamma)\left(\frac{Nt}{Nb}\right)\theta'' + 2\gamma\left(\frac{Nt}{Nb}\right)\theta' + Scf\phi' = 0, \tag{6.13}$$

the corresponding boundary conditions in dimensionless form are:

$$f(0) = 0,\ f'(0) = 1,\ \theta'(0) = -1,\ \phi'(0) = -1, \tag{6.14}$$

$$f'(\infty) = 0,\ \theta(\infty) = 0,\ \phi(\infty) = 0, \tag{6.15}$$

here prime indicates derivative w.r.t η. The involving parameters are formulated as

$$\left.\begin{aligned} &M^2 = \frac{\sigma B_0^2}{\rho c}, F^* = \frac{C_b x}{\sqrt{k_1}}, K^* = \frac{\nu}{ck_1}, \gamma = \sqrt{\frac{\nu}{ca^2}},\ Pr = \frac{\nu}{\bar{\alpha}}, \\ &Ec = \frac{u_w^2}{c_f(T_w - T_\infty)}, Rd = \frac{16\sigma^* T_\infty^3}{3kk^*}, Nt = \frac{\tilde{\tau} D_T (T_w - T_\infty)}{\nu T_\infty}, \\ &Nb = \frac{\tilde{\tau} D_B (C_w - C_\infty)}{\nu},\ Sc = \frac{\nu}{D_B}, \tilde{\tau} = \frac{(\rho c)_p}{(\rho c)_f}. \end{aligned}\right\}. \tag{6.16}$$

6.3.1 Physical Parameters of Interest

The physical quantities of engineering and scientific concern are skin friction coefficient, Nusselt number and Sherwood number, which are formulated as follows:

$$C_f = \frac{2\tau_w}{\rho u_w^2},\ Sh = \frac{aQ_m}{D_B\left(C_w - C_\infty\right)}, Nu = \frac{aQ_w}{k\left(T_w - T_\infty\right)}, \tag{6.17}$$

$$\text{Where } \tau_w = \mu\left(\frac{\partial u}{\partial r}\right)_{r=a}, Q_w = -k\left(\frac{\partial T}{\partial r}\right)_{r=a}, Q_m = -D_B\left(\frac{\partial C}{\partial r}\right)_{r=a}, \tag{6.18}$$

Using Eq. (6.10) and Eq. (6.18) in Eq. (6.17), the non-dimensional form can be expressed as below:

$$C_f\left(Re_x\right)^{0.5} = f''(0),\ Nu\left(Re_x\right)^{-0.5} = \frac{1}{\theta(0)},\ Sh\left(Re_x\right)^{-0.5} = \frac{1}{\phi(0)},\ Re_x = \frac{xu_w}{\nu}. \tag{6.19}$$

6.4 Solution Procedure

The governed flow problem is the system of nonlinear coupled ordinary differential equations from Eq. (6.11) to (6.13) along with the boundary conditions Eq. (6.14) to (6.15), which are tackled by Runge-Kutta-Fehlberg (RKF45) numerical integration technique along with shooting algorithm. The set of Eq. (6.11) to Eq. (6.13) are converted into system of seven 1st order ordinary differential equations as below.

$$f = F_1,\ f' = F_2,\ f'' = F_3,\ \theta = F_4,\ \theta' = F_5,\ \phi = F_6,\ \phi' = F_7, \tag{6.20}$$

$$\begin{bmatrix} F_1' \\ F_2' \\ F_3' \\ F_4' \\ F_5' \\ F_6' \\ F_7' \end{bmatrix} = \begin{bmatrix} F_2 \\ F_3 \\ -\frac{1}{(1+2\eta\gamma)}\left\{2\gamma F_3 + F_1F_3 - (1+F^*)F_2^{\,2} - (M^2+K^*)F_2\right\} \\ F_5 \\ -\frac{1}{\{(1+2\eta\gamma)(1+Rd)\}} \times \begin{Bmatrix} Pr(1+2\eta\gamma)\left(NbF_5F_7 + NtF_5^2\right) + \\ \gamma(2+Rd)F_5 + PrEcM^2F_2^2 + PrF_1F_5 \end{Bmatrix} \\ F_7 \\ -\frac{1}{(1+2\eta\gamma)}\left\{2\gamma F_7 + 2\gamma\left(\frac{Nt}{Nb}\right)F_5 + (1+2\eta\gamma)\left(\frac{Nt}{Nb}\right)F_5' + ScF_1F_7\right\} \end{bmatrix}, \tag{6.21}$$

$$F_1(0) = 0,\quad F_2(0) = 1,\quad F_5(0) = F_7(0) = -1\,. \tag{6.22}$$

Since $F_3(0)$, $F_4(0)$ and $F_6(0)$ are missing conditions, so we can start with the initial values of $F_3(0) = g_{10}$, $F_4(0) = g_{20}$ and $F_6(0) = g_{30}$. Let γ_1, γ_2 and γ_3 are the accurate $F_3(0)$, $F_4(0)$ and $F_6(0)$ respectively. We represent F_3, F_4 and F_6 at $\eta = \eta_\infty$ by $F_3(g_{10}, g_{20}, g_{30}, \eta_\infty)$, $F_4(g_{10}, g_{20}, g_{30}, \eta_\infty)$ and $F_6(g_{10}, g_{20}, g_{30}, \eta_\infty)$ respectively. Since F_3, F_4 and F_6 at $\eta = \eta_\infty$ are clearly function of γ_1, γ_2 and γ_3, they are expanded in Taylor series about $\gamma_1 - g_{10}$, $\gamma_2 - g_{20}$ and $\gamma_3 - g_{30}$, respectively. After explaining the system of Taylor series expansions for $\delta\gamma_1 = \gamma_1 - g_{10}$, $\delta\gamma_2 = \gamma_2 - g_{20}$ and $\delta\gamma_3 = \gamma_3 - g_{30}$, we obtain the new estimates $g_{11} = g_{10} + \delta g_{10}$, $g_{21} = g_{20} + \delta g_{20}$ and $g_{31} = g_{30} + \delta g_{30}$. Next, the complete procedure is reiterated with $F_1(0)$, $F_2(0)$, g_{11}, g_{21}, $F_5(0)$, g_{31} and $F_7(0)$ are initial conditions. With the latest estimates of γ_1, γ_2 and γ_3 the whole procedure is repeated until prescribed boundary conditions are satisfied. Finally $g_{1n} = g_{1(n-1)} + \delta g_{1(n-1)}$, $g_{2n} = g_{2(n-1)} + \delta g_{2(n-1)}$ and $g_{3n} = g_{3(n-1)} + \delta g_{3(n-1)}$ for n = 1, 2, 3. . . are attained, which seemed to be most favorite approximate initial values of $F_3(0)$, $F_4(0)$ and $F_6(0)$. By this approach, all requisite missing initial conditions are obtained. The choice of η_∞ varies from 3 to 20 depending upon the involving parameters so that no numerical oscillations would happen. Now we will solve the resulting system of seven 1st order equations by Runge-Kutta-Fehlberg (RKF45) numerical technique.

6.5 Illustration of Results

Impact of various involving emergent parameters on dimensionless velocity, temperature and concentration distributions, skin friction coefficient, Nusselt number and Sherwood number are conversed briefly via graphical and tabular results.

Figures 6.2 and 6.3 are drawn to see behavior of velocity distribution against several values of curvature parameter and magnetic parameter. From figures, it can be visualized that velocity distribution rises by enhancing curvature parameter while it decreases by increasing magnetic parameter. Figures 6.4 and 6.5 are displayed to observe the influence of porosity parameter and local inertia coefficient on velocity

distribution. We observe that the flow profile decreases by increasing both the porosity parameter and local inertia coefficient. Figure 6.6 and 6.7 depict the behavior of thermal profile versus curvature parameter and magnetic parameter. We concluded that temperature distribution rises for both curvature parameter and magnetic parameter. Obviously, Lorentz force arises in magnetic parameter. Hence this force opposes the flow, which produced an improvement in the temperature distribution and thermal boundary layer thickness.

Figures 6.8 and 6.9 represent the impact of Prandtl number and Eckert number on temperature distribution. By investigating the figure, we observed that the impact of Eckert number is to enhance the thermal distribution because of stored thermal energy in the liquid. Here $Ec = 0$ corresponds to flow without viscous dissipation or joule heating. The temperature throughout the boundary layer decreases when we increase Prandtl number. Due to this thermal boundary layer thickness is decreased. Figure 6.10 and 6.11 demonstrates the effects of thermophoretic parameter and radiation parameter on temperature distribution. We see an enhancement in thermophoretic parameters lead to larger temperature and thicker thermal boundary layer thickness. Clearly, thermophoretic parameter is due to nanoparticles concentration. The nanoparticles concentration enhances the thermal conductivity of base fluid. Due to these facts, an improvement in the temperature and thermal boundary layer thickness is found for the larger values of thermophoretic parameters. Also, it is noticed that temperature distribution is an increasing function of radiation parameter.

Figures 6.12 and 6.13 are drawn to see the behavior of concentration distribution versus curvature parameter and magnetic parameter. We can conclude that nanoparticles concentration profile is higher for higher values of curvature parameter and magnetic parameter. Figures 6.14 and 6.15 exhibits the influence of radiation parameter and Brownian motion parameter on concentration distribution. We observed that by enhancing Brownian motion parameter and thermophoretic parameter show a decrease in the concentration distribution and its related boundary layer thickness, while the reverse trend is seen for increasing radiation parameter.

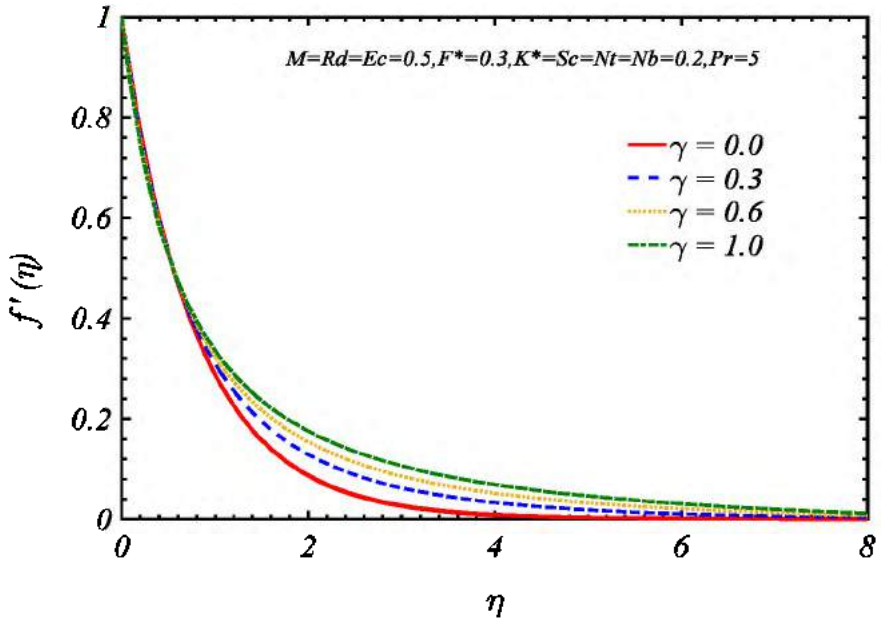

Figure 6.2: Variation of $f'(\eta)$ via curvature parameter γ.

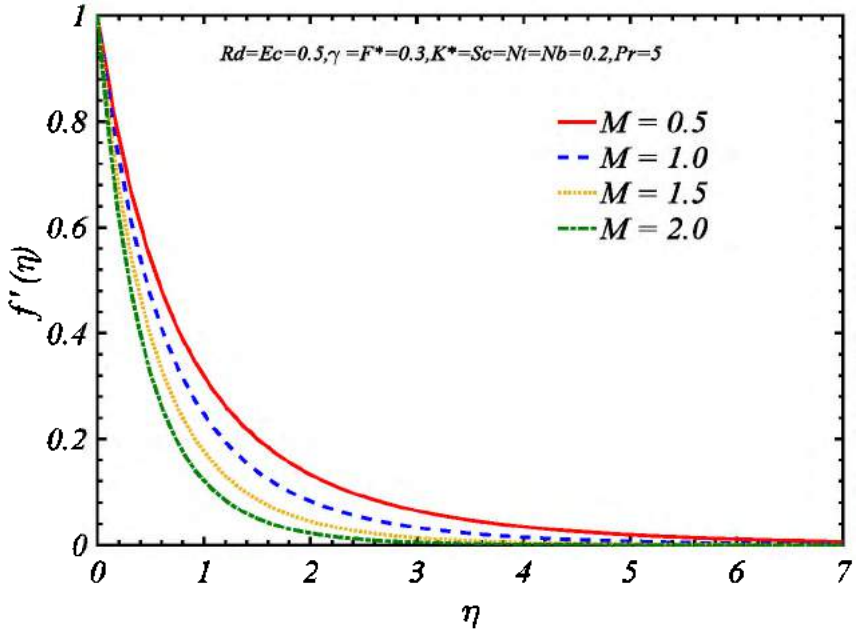

Figure 6.3: Variation of $f'(\eta)$ via magnetic parameter M.

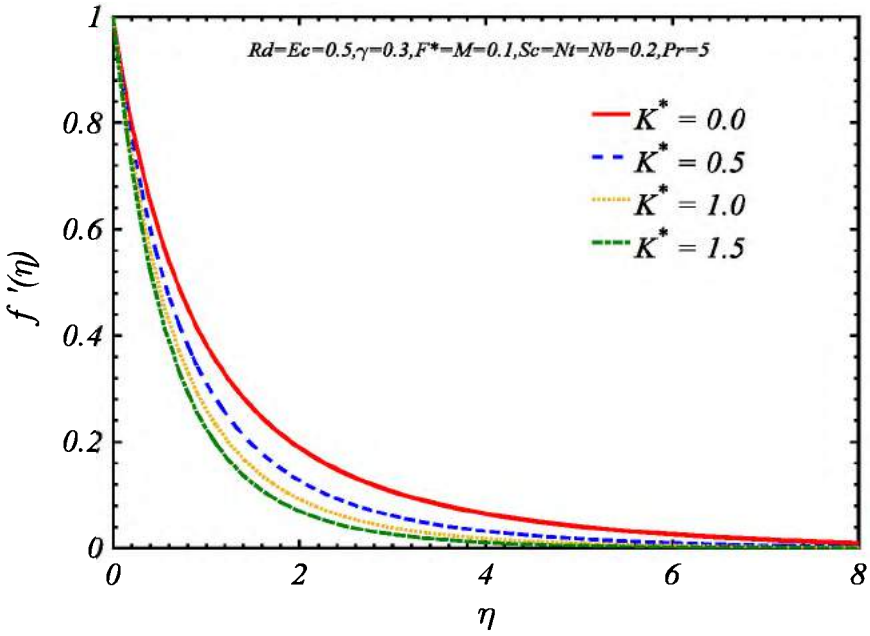

Figure 6.4: Variation of $f'(\eta)$ via porosity parameter K^*.

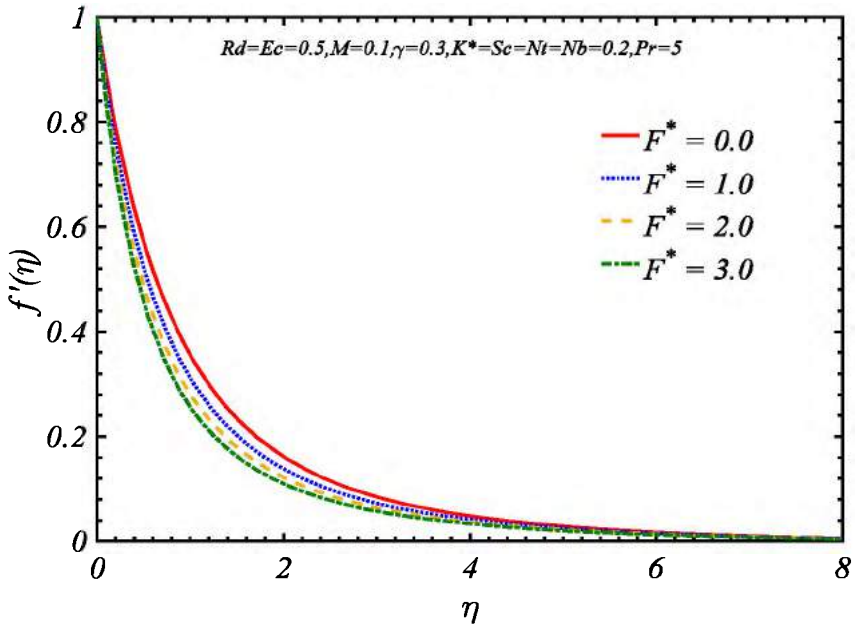

Figure 6.5: Variation of $f'(\eta)$ via non-Darcy parameter F^*.

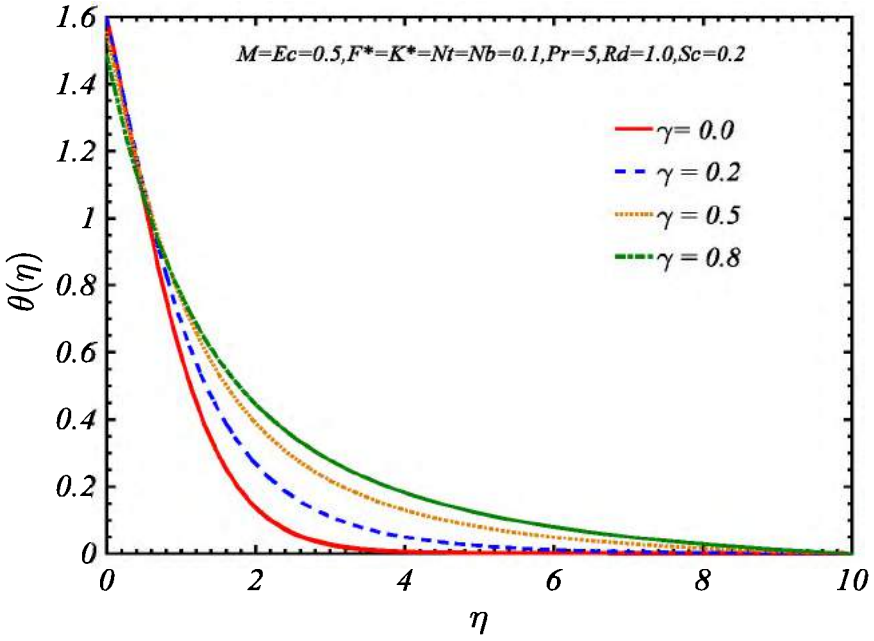

Figure 6.6: Variation of $\theta(\eta)$ via curvature parameter γ.

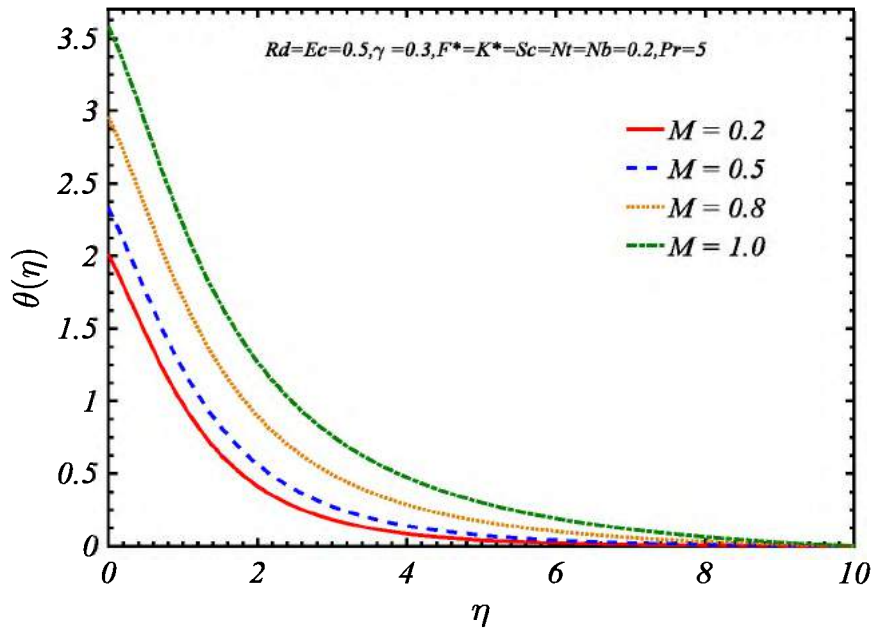

Figure 6.7: Variation of $\theta(\eta)$ via magnetic parameter M.

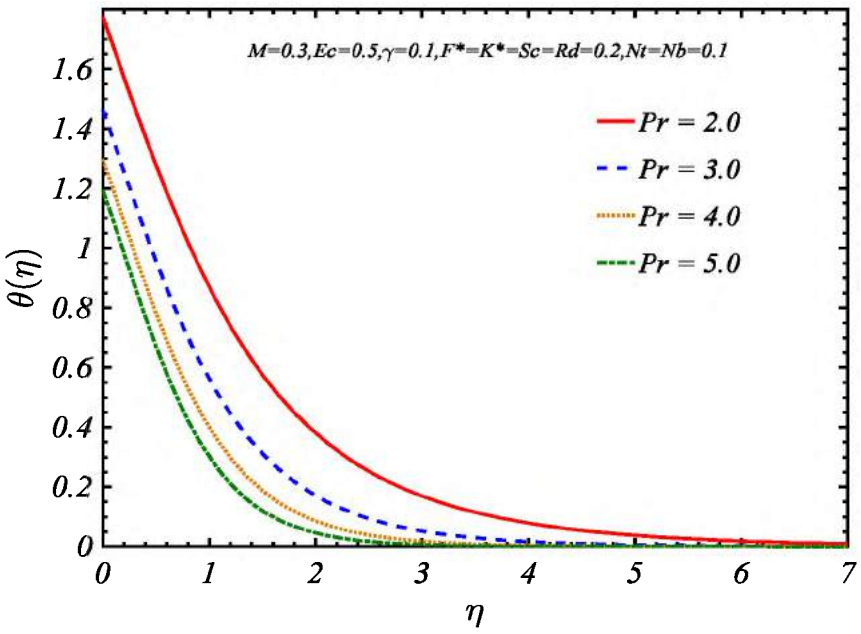

Figure 6.8: Variation of $\theta(\eta)$ via Prandtl number Pr.

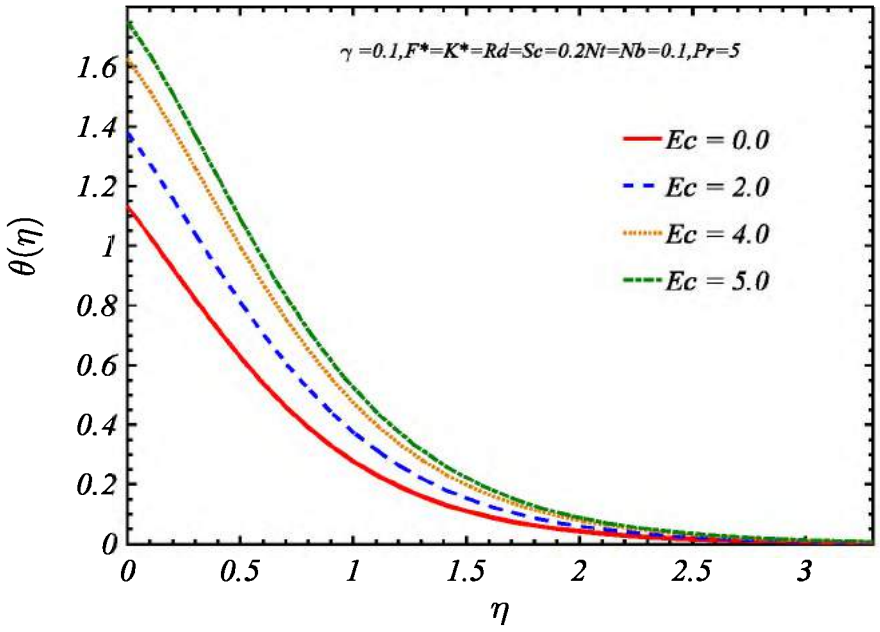

Figure 6.9: Variation of $\theta(\eta)$ via Eckert number Ec.

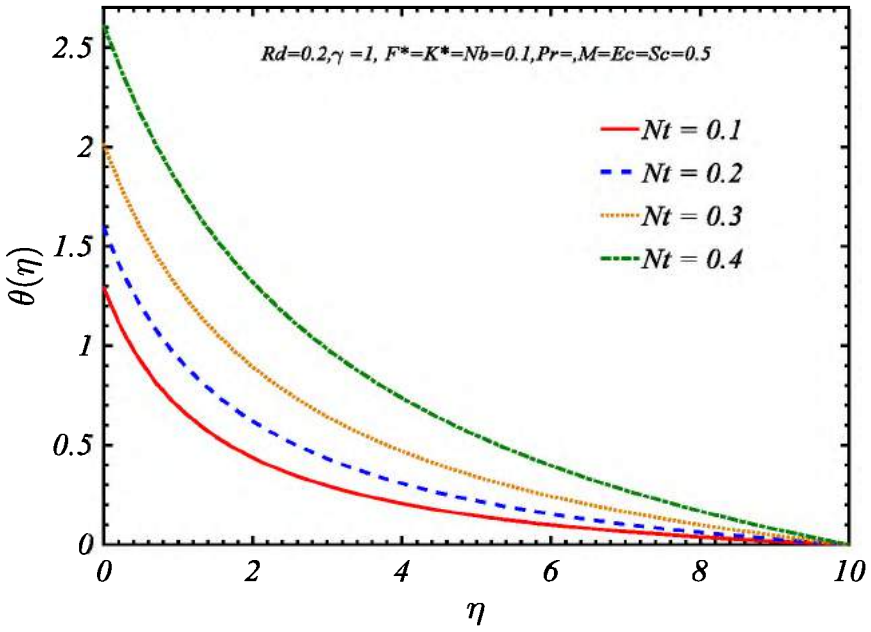

Figure 6.10: Variation of $\theta(\eta)$ via thermophoretic parameter Nt.

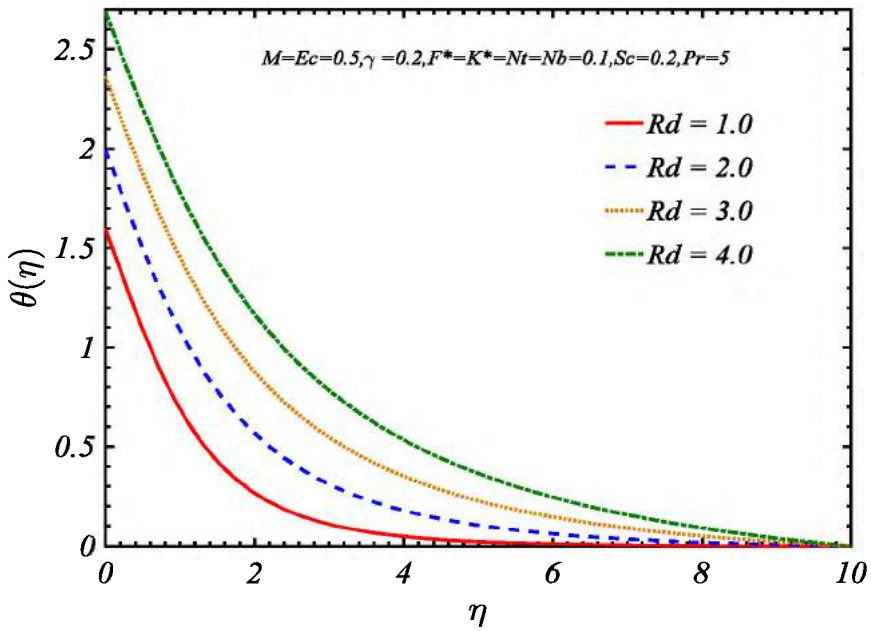

Figure 6.11: Variation of $\theta(\eta)$ via radiation parameter Rd

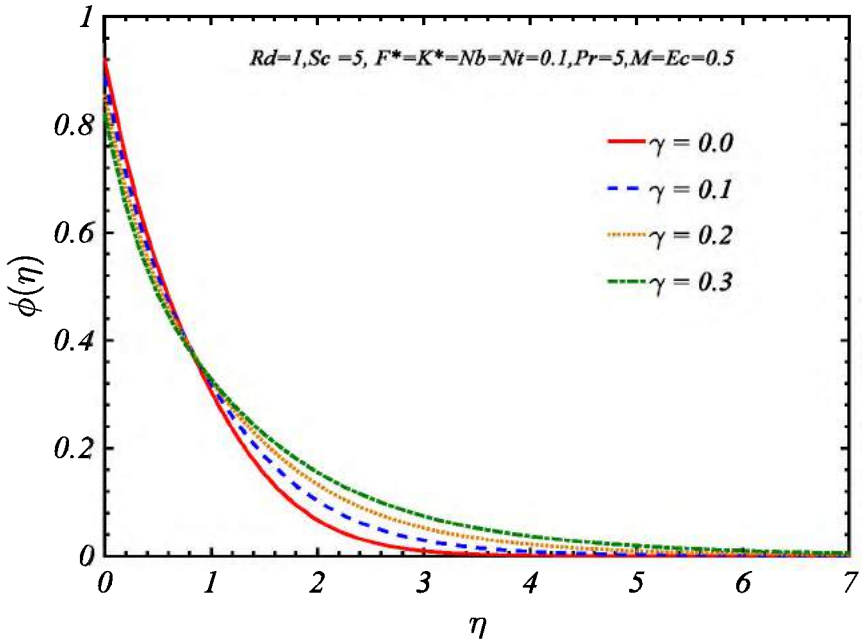

Figure 6.12: Variation of $\phi(\eta)$ via curvature parameter γ.

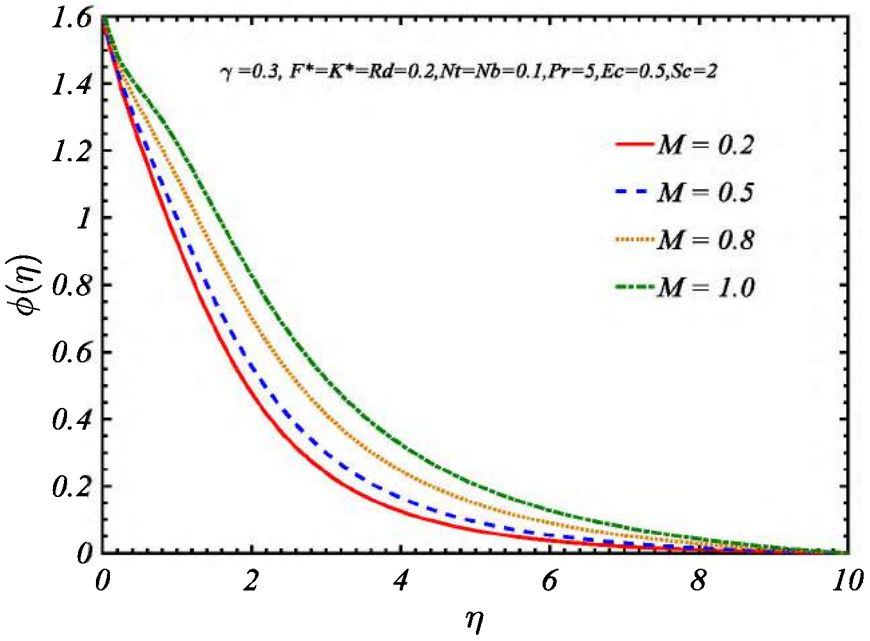

Figure 6.13: Variation of $\phi(\eta)$ via magnetic parameter M.

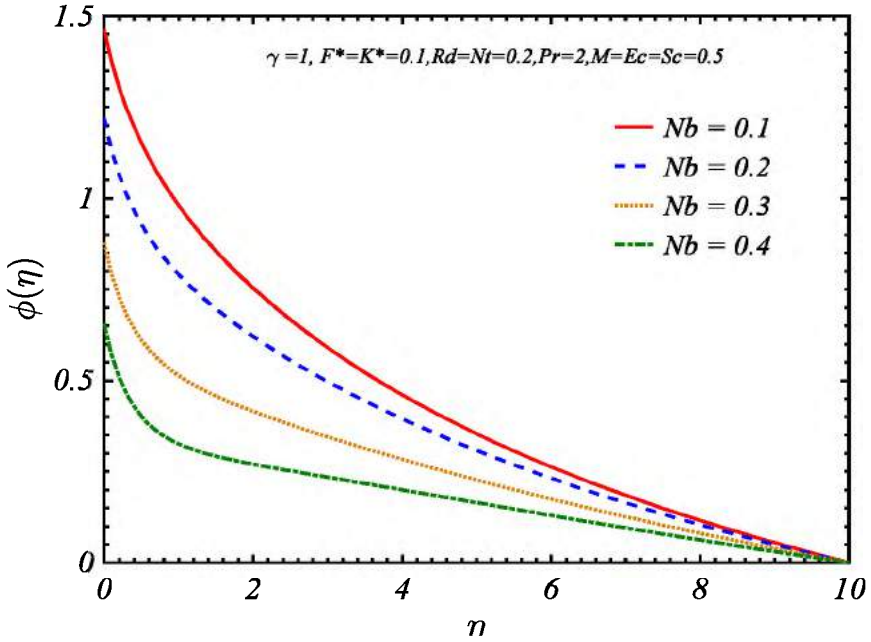

Figure 6.14: Variation of $\phi(\eta)$ via Brownian motion parameter *Nb.*

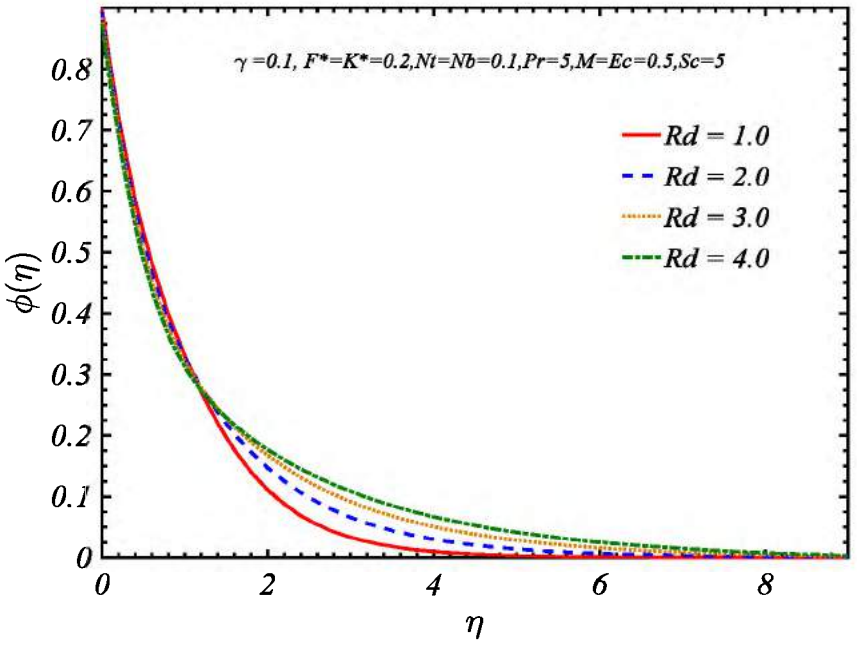

Figure 6.15: Variation of $\phi(\eta)$ via radiation parameter *Rd*.

The numerically computed values $C_f\left(Re_x\right)^{0.5}$ for numerous values of γ, K^*, F^* when M = 0, 0.5, 1.0 are displayed in table 6.1. In case of M = *0* resembles to hydro-

dynamic flow, while $M > 0$ denotes the hydromagnetic flow. We can visualize that numerical values of $C_f \left(Re_x\right)^{0.5}$ are greater for the case of hydromagnetic flow. Because the Lorentz force for the greater values of magnetic parameter becomes more prominent this opposes the flow. Due to this, an enhancement in skin-friction coefficient can be seen. The large values of skin friction coefficient correspond to increasing curvature parameter. The skin friction coefficient is increased when we increase the porosity parameter and local inertia coefficient.

Table-6.1: Numerical values of skin-friction coefficient $C_f \left(Re_x\right)^{0.5}$ for various values of K^*, F^* and γ when *M = 0, M = 0.5* and *M = 1*

γ	K^*	F^*	$C_f \left(Re_x\right)^{0.5}$ at $M = 0$	$C_f \left(Re_x\right)^{0.5}$ at $M = 0.5$	$C_f \left(Re_x\right)^{0.5}$ at $M = 1$
0.0	0.2	0.2	1.1525	1.2567	1.5267
0.3			1.2703	1.3796	1.6578
0.6			1.3834	1.4961	1.7814
1.0			1.5288	1.6447	1.9381
0.2	0.0	0.2	1.1364	1.2541	1.5469
	0.2		1.2316	1.3394	1.6150
	0.5		1.3598	1.4567	1.7117
0.2	0.2	0.0	1.1744	1.2871	1.5720
		0.2	1.2316	1.3394	1.6150
		0.5	1.3130	1.4144	1.6775

Table 6.2 represents the numerically computed local Nusselt number and Sherwood number for several values of Rd, Sc, Nb, Nt and Ec at fixed values of $Pr = 5.0, M = 0.5, K^* = 0.2$, $F^* = 0.2$ and $\gamma = 0.2$. It is noticed from table that the local Nusselt number are reduces while local Sherwood number increases by

increasing the radiation parameter. By raising Schmidt number the local Nusselt number and Sherwood number are increased. By increasing Brownian motion parameter and thermophoretic parameter, the local Nusselt number reduces, while the Sherwood number is increased. By increasing Eckert number, the local Nusselt number and Sherwood number are reduced because of the stronger Joule dissipation.

Table 6.2: Numerical values of $Nu\left(Re_x\right)^{-0.5}$ and $Sh\left(Re_x\right)^{-0.5}$ for different values of Nt, Nb, Ec, Rd, Sc when $Pr = 5.0, M = 0.5, K^* = F^* = \gamma = 0.2$

Rd	*Sc*	*Ec*	*Nt*	*Nb*	$Nu\left(Re_x\right)^{-0.5}$	$Sh\left(Re_x\right)^{-0.5}$
0.0	1.0	0.5	0.1	0.1	0.8497	0.3640
0.2					0.7964	0.3660
0.5					0.7274	0.3693
0.3	0.5	0.5	0.1	0.1	0.7596	0.2514
	1.0				0.7720	0.3671
	1.5				0.7821	0.4834
0.3	1.0	0.1	0.1	0.5	0.7720	0.3671
		0.2			0.5891	0.2844
		0.3			0.4108	0.2634
0.3	1.0	0.1	0.1	0.5	0.7720	0.3671
			0.2		0.6162	0.4667
			0.3		0.4797	0.5164
0.3	1.0	0.1	0.1	0.0	0.8784	0.3591
				0.5	0.7720	0.3671
				1.0	0.6880	0.3755

Chapter 7

Hydromagnetic Transport of Non-Newtonian Nanofluid over a Permeable Stretching Cylinder with Binary Chemical Reaction and Arrhenius Activation Energy using Convective Boundary Conditions

7.1 Introduction

The present chapter investigates the magnetohydrodynamic flow of Casson nanofluid flow past over permeable stretching cylinder by employing Buongiorno's mathematical model. Unlike the frequently used constant temperature and concentration boundary conditions, the present study employed convective boundary conditions. The influences of inclined magnetic field, joule heating, viscous dissipation, Thermophoresis, Brownian motion, chemical reaction and Arrhenius activation energy are accounted for. The flow problem is first modeled and then transformed into dimensionless form via suitable similarity transforms. For solution purpose Runge-Kutta-Fehlberg fourth-fifth order (RKF45) scheme with shooting algorithm is adopted. Impact of various emerging parameters on the velocity, temperature and concentration distributions, skin friction coefficient, Nusselt number and Sherwood number are depicted via graphs and tables.

7.2 Geometry of Problem

Assuming a steady two dimensional boundary layer flow of non-Newtonian Casson nanofluid over a permeable stretching cylinder. The cylindrical polar coordinates x and r are considered in axial and radial directions respectively. The cylinder is linearly stretched with wall velocity $u_w(x) = cx$. The external magnetic field B_0 is applied at an inclination ψ. The boundary conditions at the surface of cylinder are convective type. The impact of pressure gradient and external body forces is supposed to be negligible and the flow is originated due to linear stretching of cylinder. Physical flow model and coordinate system are given in figure 7.1.

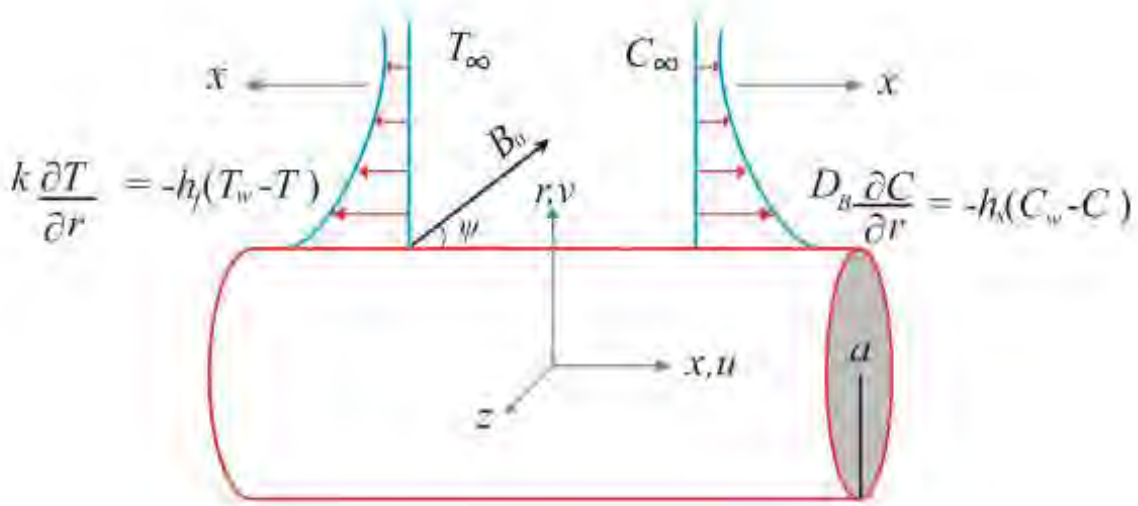

Figure 7.1: Flow schematic, coordinates and geometrical variables.

7.3 Mathematical Formulation

The rheological equation of state for an isotropic and incompressible flow of non-Newtonian Casson fluid can be expressed as follows:

$$\tau_{ij} = \begin{cases} 2e_{ij}\left(\mu_B + \dfrac{p_r}{\sqrt{2\pi}}\right), & \pi > \pi_c, \\ 2e_{ij}\left(\mu_B + \dfrac{p_r}{\sqrt{2\pi_c}}\right), & \pi < \pi_c, \end{cases} \tag{7.1}$$

Where e_{ij} the rate of strain tensor, μ_B the Casson coefficient of viscosity, p_r the yield stress of fluid, π the product of the component of deformation rate with itself, and π_c is the critical value of product of the component of the rate of strain tensor with itself.

Under above mentioned suppositions and boundary layer approximation the governing flow problem of steady Casson nanofluid can be expressed as follows:

$$\frac{\partial}{\partial x}(ru) + \frac{\partial}{\partial r}(rv) = 0, \tag{7.2}$$

$$u\frac{\partial u}{\partial x} + v\frac{\partial u}{\partial r} = \nu\left(1 + \frac{1}{\beta_2}\right)\frac{1}{r}\frac{\partial}{\partial r}\left(r\frac{\partial u}{\partial r}\right) - \frac{\sigma B_0^2 \sin^2\psi}{\rho}u, \tag{7.3}$$

$$u\frac{\partial T}{\partial x}+v\frac{\partial T}{\partial r}=\hat{\alpha}\frac{1}{r}\frac{\partial}{\partial r}\left(r\frac{\partial T}{\partial r}\right)+\tilde{\tau}\left[D_B\frac{\partial T}{\partial r}\frac{\partial C}{\partial r}+\frac{D_T}{T_\infty}\left(\frac{\partial T}{\partial r}\right)^2\right]+\frac{\nu}{c_p}\left(1+\frac{1}{\beta_2}\right)\left(\frac{\partial u}{\partial r}\right)^2+\frac{\sigma B_0^2\sin^2\psi}{\rho c_p}u^2, \tag{7.4}$$

$$u\frac{\partial C}{\partial x}+v\frac{\partial C}{\partial r}=D_B\frac{1}{r}\frac{\partial}{\partial r}\left(r\frac{\partial C}{\partial r}\right)+\frac{D_T}{T_\infty}\frac{1}{r}\frac{\partial}{\partial r}\left(r\frac{\partial T}{\partial r}\right)-k_r^2\left(\frac{T}{T_\infty}\right)^n \mathrm{e}^{\frac{-E_a}{\kappa T}}\left(C-C_\infty\right). \tag{7.5}$$

The appropriate set of boundary conditions is given below:

$$\text{At}\quad r=a\ :u=u_w\left(x\right),\ \ v=v_w,\ \ k\frac{\partial T}{\partial r}=-h_f\left(T_s-T\right),\ \ D_B\frac{\partial C}{\partial r}=-h_s\left(C_s-C\right), \tag{7.6}$$

$$\text{At}\quad r\to\infty\quad u=0,\ T=T_\infty,\ \ C=C_\infty. \tag{7.7}$$

In above equations k_r^2 the chemical reaction rate, E_a the activation energy , $\kappa=8.61\times10^{-5}\mathrm{eVK}^{-1}$ the Boltzman constant, n the unit less exponent fitted rate constant which lies in the range $n\in\left(-1,1\right)$.

To convert the problem in similar form, invoking the following similarity variables:

$$\eta=\frac{r^2-a^2}{2a}\sqrt{\frac{c}{\nu}},\ u=cxf'\left(\eta\right),\ v=-\frac{a}{r}\sqrt{c\nu}\,f\left(\eta\right),\theta=\frac{T-T_\infty}{T_w-T_\infty},\ \phi=\frac{C-C_\infty}{C_w-C_\infty}. \tag{7.8}$$

Using Eq. (7.8) in Eq. (7.2) to Eq. (7.5) along with boundary conditions Eq. (7.6) to Eq. (7.7), we got the following non-dimensional form:

$$\left(1+2\eta\gamma\right)f'''+2\gamma f''+\frac{\beta_2}{1+\beta_2}\left\{ff''-f'^2-M^2\sin^2\psi f'\right\}=0, \tag{7.9}$$

$$\frac{1}{Pr}\left\{\left(1+2\eta\gamma\right)\theta''+2\gamma\theta'\right\}+\left(1+2\eta\gamma\right)\left\{\left(\frac{1+\beta_2}{\beta_2}\right)Ecf''^2+Nb\theta'\phi'+Nt\theta'^2\right\}+M^2Ec\sin^2\psi f'^2+f\theta'=0, \tag{7.10}$$

$$\left(1+2\eta\gamma\right)\left\{\phi''+\frac{Nt}{Nb}\theta''\right\}+2\gamma\left\{\phi'+\frac{Nt}{Nb}\theta'\right\}+Scf\phi'-\beta_3Sc\left(1+\hat{\delta}\theta\right)^n e^{\frac{-E_A}{1+\hat{\delta}\theta}}\phi=0, \tag{7.11}$$

Subject to the below boundary conditions in non-dimensional form:

$$f\left(0\right)=-\alpha^*,\ \ f'\left(0\right)=1,\ \ \theta'\left(0\right)=-Bi\left\{1-\theta\left(0\right)\right\},\ \ \phi'\left(0\right)=-Bj\left\{1-\phi\left(0\right)\right\}, \tag{7.12}$$

$$f'\left(\infty\right)=0,\ \ \theta\left(\infty\right)=0,\ \ \phi\left(\infty\right)=0. \tag{7.13}$$

The parameters involving in the governing equations are formulated as follows:

$$\left.\begin{aligned} &M^2=\frac{\sigma B_0^2}{\rho c},\gamma=\sqrt{\frac{\nu}{a^2 c}},Pr=\frac{\mu c_p}{k},Ec=\frac{u_w^2}{c_p\left(T_s-T_\infty\right)},Nt=\frac{\tilde{\tau}D_T\left(T_w-T_\infty\right)}{\nu T_\infty},\\ &Nb=\frac{\tilde{\tau}D_B\left(C_w-C_\infty\right)}{\nu},\tilde{\tau}=\frac{\left(\rho c_p\right)_p}{\left(\rho c_p\right)_f},Sc=\frac{\nu}{D_B},E_A=\frac{E_a}{\kappa T_\infty},\beta_3=\frac{k_r^2}{c},\\ &\hat{\delta}=\frac{T_s-T_\infty}{T_\infty},Bi=\frac{h_f}{k}\sqrt{\frac{\nu}{c}},Bj=\frac{h_s}{D_B}\sqrt{\frac{\nu}{c}},\alpha^*=\frac{v_w}{\sqrt{c\nu}}. \end{aligned}\right\}. \tag{7.14}$$

7.3.1 Physical Parameters of Interest

The quantities of practical, scientific and engineering concern are skin friction coefficient, Nusselt number and Sherwood number, which are given as follows:

$$C_f=\frac{2\tau_w}{\rho u_w^2},\ Nu=\frac{xQ_w}{k\left(T_w-T_\infty\right)},\ Sh=\frac{xQ_m}{D_B\left(C_w-C_\infty\right)}, \tag{7.15}$$

in above Eq. (7.15) τ_w is the wall shear stress, Q_w the wall heat flux and Q_m the wall mass flux, which are formulated as follows:

$$\tau_w=\mu\left(1+\frac{1}{\beta_2}\right)\left(\frac{\partial u}{\partial r}\right)_{r=a},\quad Q_w=-k\left(\frac{\partial T}{\partial r}\right)_{r=a},\quad Q_m=-D_B\left(\frac{\partial C}{\partial r}\right)_{r=a}, \tag{7.16}$$

using Eq. (7.8) and Eq. (7.16) in Eq. (7.15), the dimensionless form can be written as:

$$0.5\left(Re_x\right)^{0.5}C_f=\left(1+\frac{1}{\beta_2}\right)f''(0),\ Nu\left(Re_x\right)^{-0.5}=-\theta'(0),\ Sh\left(Re_x\right)^{-0.5}=-\phi'(0). \tag{7.17}$$

7.4 Solution Procedure

In order to apply Runge-Kutta-Fehlberg fourth-fifth order (RKF45) numerical integrating scheme, first of all we converted the governing problem into system of simultaneous first order equations. Let us assume

$$f=F_1,\ f'=F_2,\ f''=F_3,\ \theta=F_4,\ \theta'=F_5,\ \phi=F_6,\ \phi'=F_7, \tag{7.18}$$

$$\left.\begin{aligned}
&F_1' = F_2, F_2' = F_3, F_3' = \frac{-1}{(1+2\eta\gamma)}\left\{2\gamma F_3 + \frac{\beta_2}{1+\beta_2}\left(F_1F_3 - F_2^{\,2} - M^2\sin^2\psi F_2\right)\right\},\\
&F_4' = F_5, F_5' = \frac{-Pr}{(1+2\eta\gamma)}\left\{\begin{aligned}&\left(\frac{1+\beta_2}{\beta_2}\right)(1+2\eta\gamma)EcF_3^2 + Nb(1+2\eta\gamma)F_5F_7 +\\ &Nt(1+2\eta\gamma)F_5^2 + M^2Ec\sin^2\psi F_2^{\,2} + 2\left(\frac{\gamma}{Pr}\right)F_5 + F_1F_5\end{aligned}\right\},\\
&F_6' = F_7, F_7' = \frac{-1}{(1+2\eta\gamma)}\left\{\begin{aligned}&2\gamma F_7 + 2\gamma\left(\frac{Nt}{Nb}\right)F_5 + (1+2\eta\gamma)\left(\frac{Nt}{Nb}\right)F_5' + ScF_1F_7 -\\ &\beta_3 Sc\left(1+\tilde{\delta}F_4\right)^n e^{\frac{-E_A}{1+\delta F_4}}F_6\end{aligned}\right\}.
\end{aligned}\right\}, \quad (7.19)$$

$$\left.\begin{aligned}
&F_1(0) = -\alpha^*, F_2(0) = 1, F_3(0) = s_1, F_4(0) = s_2,\\
&F_5(0) = -Bi(1-s_2), F_6(0) = s_3, F_7(0) = -Bj(1-s_3).
\end{aligned}\right\}. \quad (7.20)$$

Here $[s_1,\ s_2,\ s_3] = [f''(0),\ \theta(0),\ \phi(0)]$ are the missing initial conditions. Appropriate values of unknown initial conditions s_1, s_2 and s_3 are estimated by using Newton-Raphson method iteratively. Once the missing initial conditions are achieved then we will solve the resulting system of seven first order equations by Runge-Kutta-Fehlberg (RKF45) numerical scheme. In table 7.1 the obtained results are authenticated by comparing them with published results and found good agreement.

Table - 7.1: Verification of results for Nusselt number $-\theta'(0)$ versus numerous values of Pr at fixed values of $M = \beta_2 = \beta_3 = \alpha^* = Ec = Sc = \gamma = Nt = 0, Bi \to \infty, Bj \to \infty$

Pr	Present	Khan and Pop [114]	Gorla and Sidawi [115]
0.7	0.4539	0.4539	0.4539
2	0.9100	0.9114	0.9114
7	1.8908	1.8954	1.8905
20	3.3409	3.3539	3.3539
70	6.4173	6.4622	6.4622

7.5 Illustration of Results

Impact of emerging sundry parameters like magnetic parameter, Casson parameter, curvature parameter, inclination of magnetic field, thermophoretic parameter,

Brownian parameter, activation energy parameter, chemical reaction parameter, thermal Biot number, diffusion Biot number and suction parameter on dimensionless profiles of velocity, temperature and concentration are illustrated through figures. 7.2 to 7.14. For evaluation of graphical results, some parameters are fixed like $Pr = 7, Sc = 10, n = \tilde{\delta} = Ec = 0.5, \gamma = 0.25$.

Figures 7.2 to 7.4 are drawn to explore the impact of magnetic parameter on dimensionless velocity, temperature and concentration distributions of nanofluid. Figure 7.2 illustrates that velocity of Casson nanofluid have a decreasing behaviour by raising magnetic parameter. Magnetic parameter is the ratio of electromagnetic forces to viscous forces and we are applying inclined magnetic field which opposes the flow, therefore velocity distribution decreases. Figure 7.3 and figure. 7.4 demonstrate that the temperature and concentration distributions rise by enhancing magnetic field parameter. Because magnetic field produces "Lorentz force" which resists the flow due to this temperature and concentration distributions are increases. Figure 7.5 is drawn to investigate the behaviour of Casson parameter on dimensionless flow velocity of nanofluids. Physically, enhancing Casson parameter will causes enhancements in plastic dynamic viscosity. From graphical results, we observed that by enlarging Casson fluid parameter the velocity of nanofluids decreases due to greater resistance in the fluid flow.

Figures 7.6 to 7.8 are plotted to interpret the significance of inclination of magnetic field on dimensionless velocity, temperature and concentration distributions of nanofluid. By up surging the magnetic field inclination the velocity distribution declines while the temperature and concentration distributions are increases. Figures 7.9 and 7.10 are portrayed to examine the impact of thermophoretic parameter on temperature and concentration distribution. From graphs, we perceived that by enhancing thermophoretic parameter both the temperature distribution as well as the concentration distributions is enhanced. This is because diffusion penetrates deeper into the fluid so by enhancing the thermophoretic parameter will causes the thickening of the thermal boundary layer as well as the concentration boundary layer. It is very fascinating to see that the influence of thermophoretic parameter is more prominent on the nanoparticles concentration distribution as compared to the temperature distribution.

The influence of Brownian motion parameter on temperature and concentration distributions is shown in figure 7.11 and 7.12. Brownian motion is basically the inconsistent random movement of nanoparticles. It has been instigated that the Brownian motion of nanofluid at the molecular level is a central mechanism leading to thermal conductivity of nanofluids. Enhancing Brownian motion parameter increases the temperature distribution while the reverse trend is observed in concentration distribution. In fact by increasing Brownian motion parameter, the kinetic energy of nanoparticles rises due to which temperature field increases. The concentration distribution is fall down against the greater values of the Brownian motion parameter. In chemical engineering, binary chemical reaction is a type of reaction which takes place in two steps. The activation energy is a terminology invented by Svante Arrhenius and is defined as the amount of energy needed for a chemical reaction to be happening. For a chemical reaction to occur at a reasonable rate there should be a significant number of molecules with energy equal to or greater than the activation energy. Figure 7.13 is drawn to notice the influence of chemical reaction parameter on concentration distribution. By enhancing chemical reaction parameter the concentration profiles declined with in the boundary layer. Figure 7.14 illustrates the impact of activation energy parameter on concentration distribution. From figure we can see that if the amount of energy needed to start the chemical reaction is large then the concentration profile will depicts the increasing behaviour.

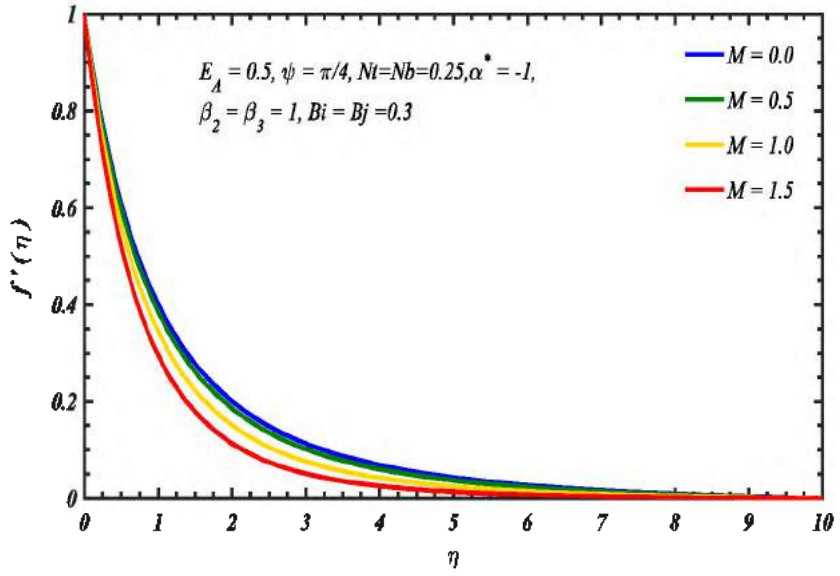

Figure 7.2: Impact of magnetic parameter M on velocity distribution $f'(\eta)$.

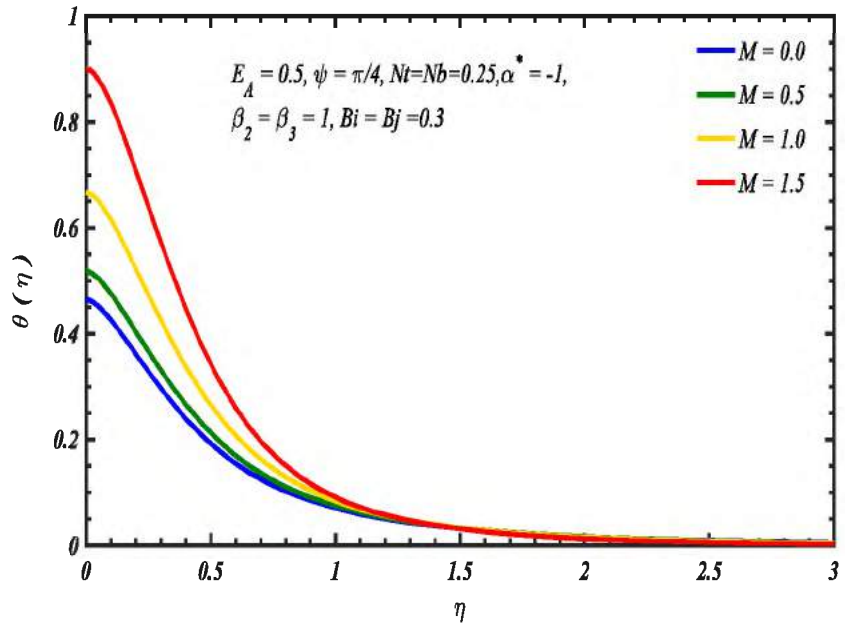

Figure 7.3: Impact of magnetic parameter M on temperature distribution $\theta(\eta)$.

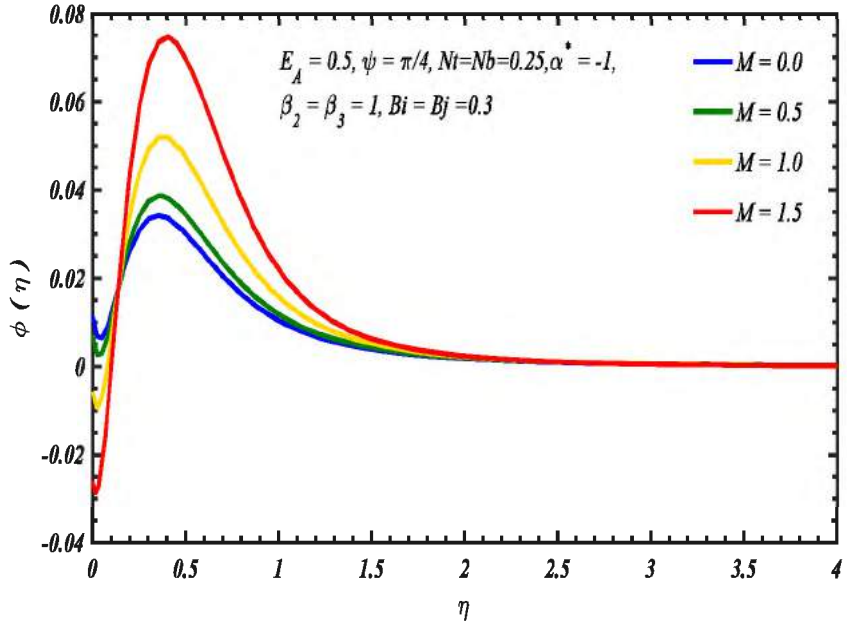

Figure 7.4: Impact of magnetic parameter M on concentration distribution $\phi(\eta)$.

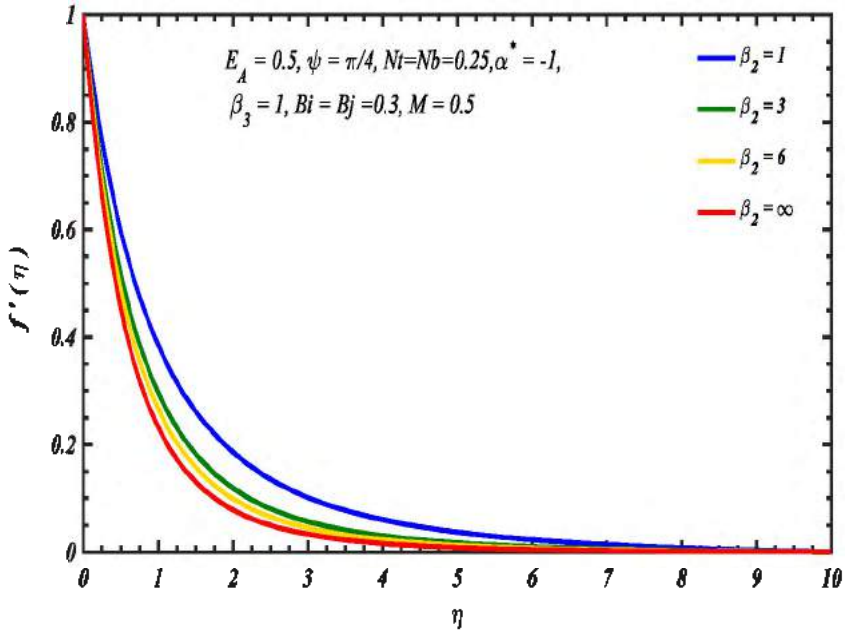

Figure 7.5: Impact of Casson fluid parameter β_2 on velocity distribution $f'(\eta)$.

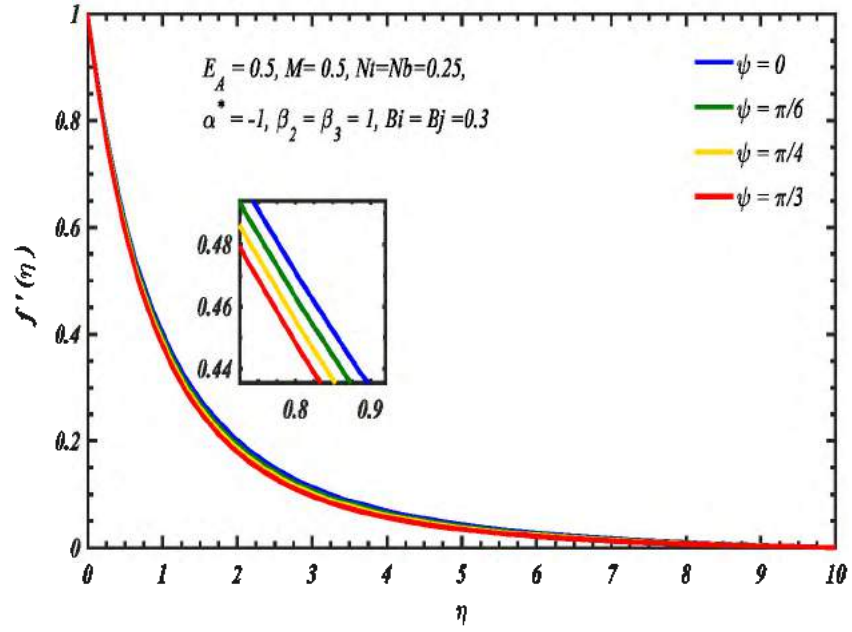

Figure 7.6: Impact of magnetic field inclination ψ on velocity distribution $f'(\eta)$.

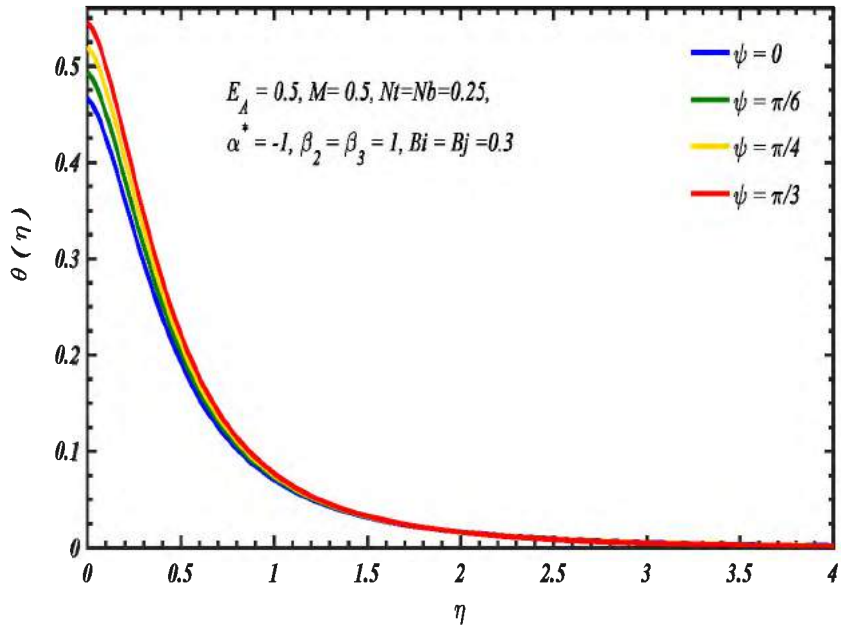

Figure 7.7: Impact of magnetic field inclination ψ on temperature distribution $\theta(\eta)$.

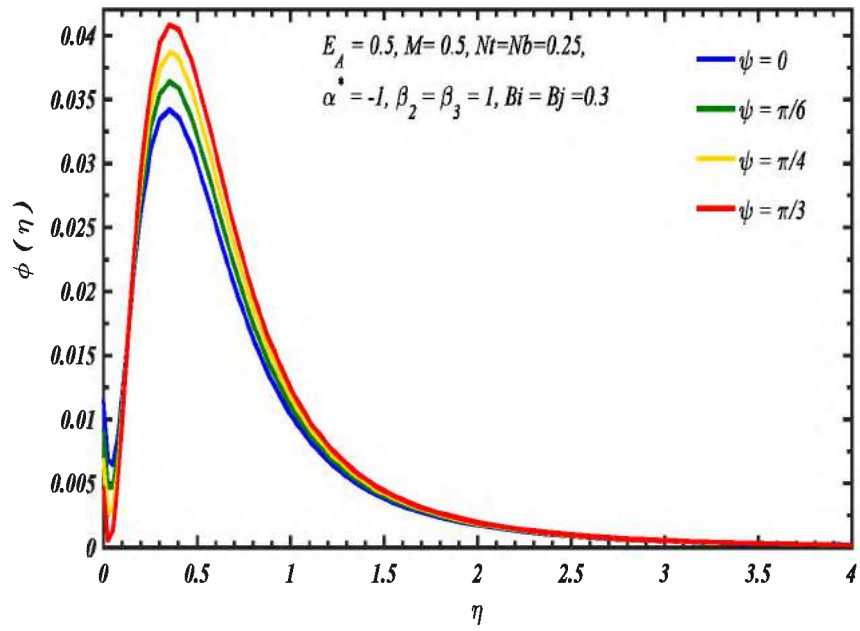

Figure 7.8: Impact of magnetic field inclination ψ on concentration distribution $\phi(\eta)$.

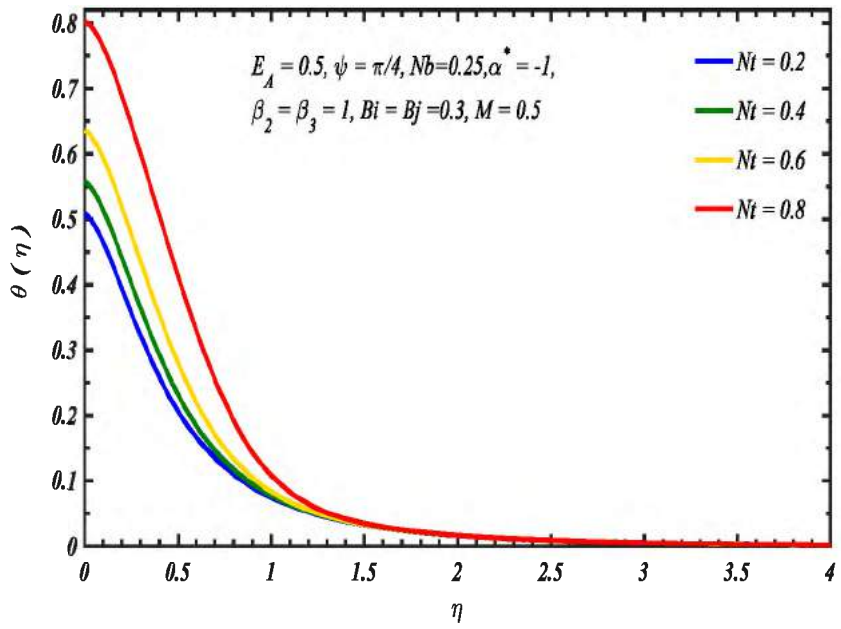

Figure 7.9: Impact of thermophoretic parameter Nt on temperature distribution $\theta(\eta)$.

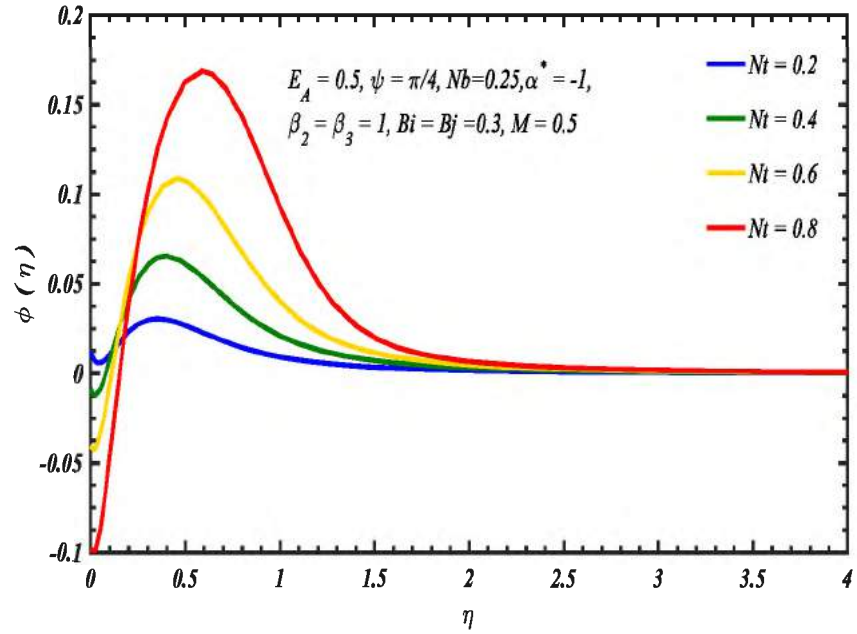

Figure 7.10: Impact of thermophoretic parameter Nt on concentration distribution $\phi(\eta)$.

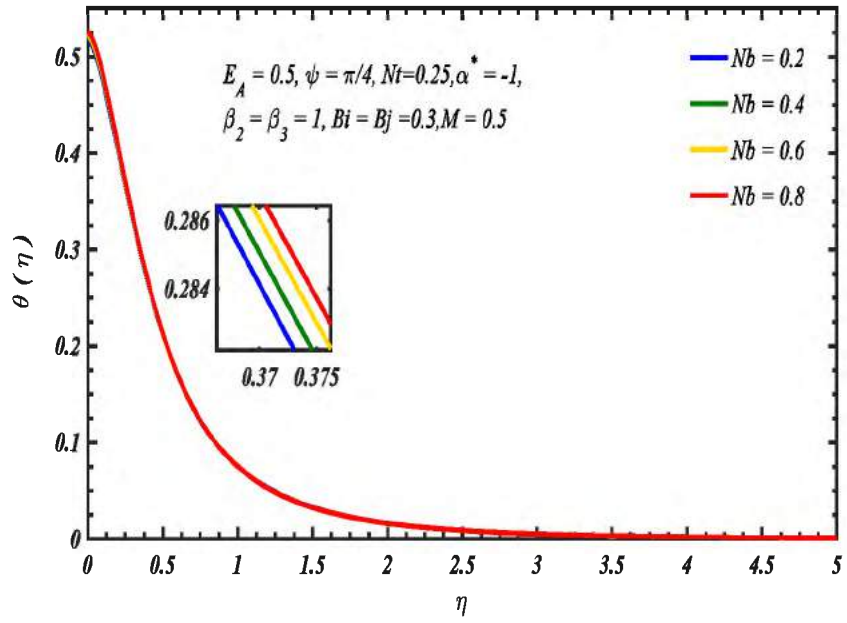

Figure 7.11: Impact of Brownian motion parameter on temperature distribution $\theta(\eta)$.

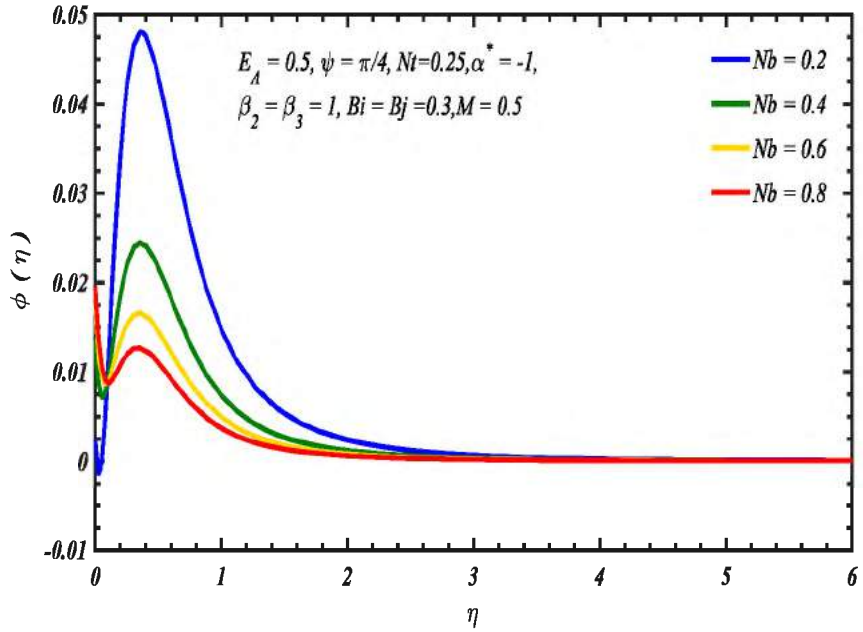

Figure 7.12: Impact of Brownian motion parameter on concentration distribution $\phi(\eta)$.

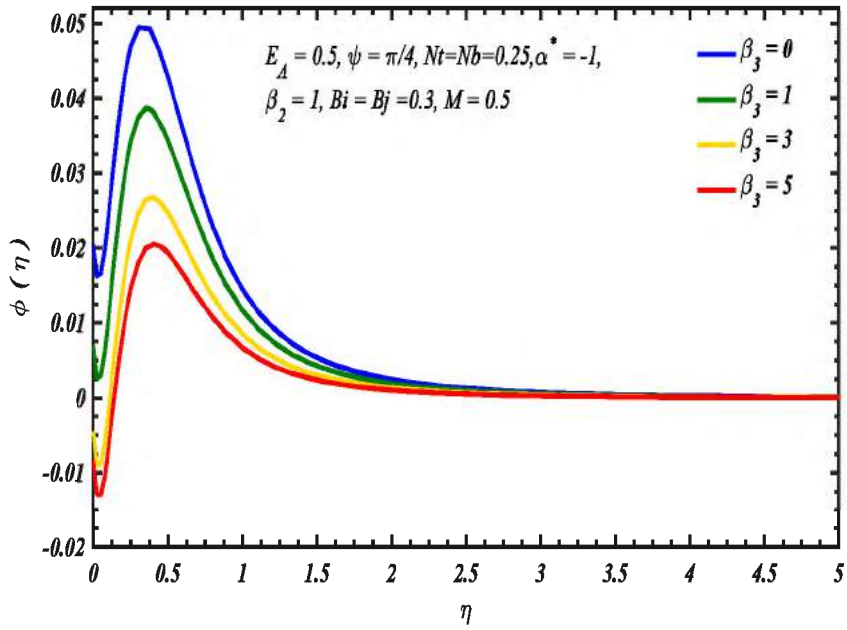

Figure 7.13: Impact of chemical reaction parameter on concentration distribution $\phi(\eta)$.

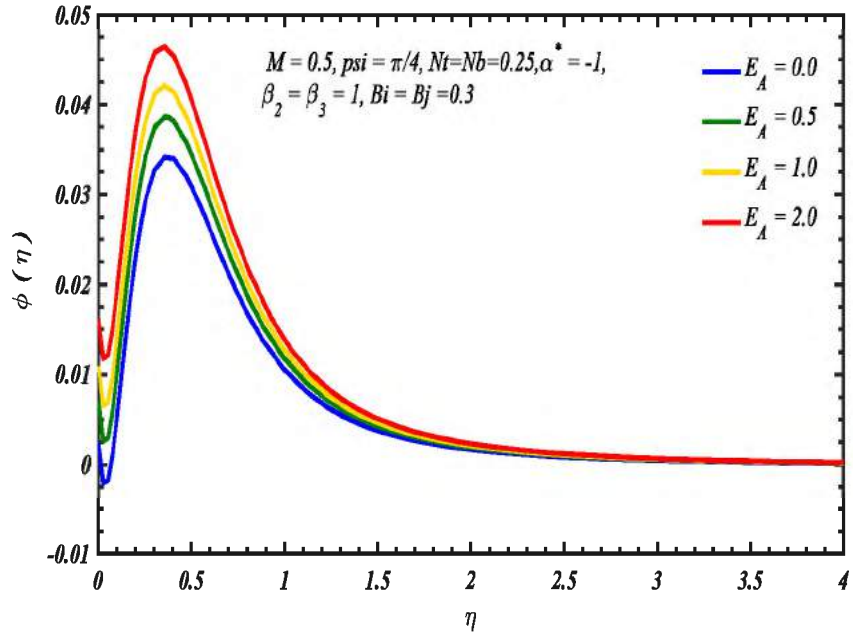

Figure 7.14: Impact of activation energy parameter on concentration distribution $\phi(\eta)$.

The variations in skin friction coefficient, Nusselt number and Sherwood number verses numerous parameters are computed in table 7.2 to table 7.4. In table 7.2 the numerical values of skin friction coefficient are calculated for several distinct parameters like Casson fluid parameter, magnetic parameter, curvature parameter, suction parameter and magnetic field inclination. We perceived that the skin friction coefficient decreases by increasing the Casson fluid parameter and the opposite trend can be seen for the case of magnetic parameter, curvature parameter, suction parameter and magnetic field inclination.

Table-7.2: Numerical values of skin friction coefficient at fixed values of $Pr = 7, Sc = 10, \tilde{\delta} = \beta_3 = E_A = n = Ec = 0.5, Bi = Bj = 0.3, Nt = Nb = 0.25$

β_2	M	γ	α^*	ψ	$-\left(1+1/\beta_2\right) f''(0)$
0.5	0.5	0.25	-1	$\pi/4$	2.6751
1					2.2480
1.5					2.0917
1	0				2.1584
	0.4				2.2164
	1				2.4880
1	0.5	0.0			2.0812
		0.2			2.2134
		0.5			2.4253
1	0.5	0.25	0		1.6963
			-0.5		1.9556
			-1		2.2480
1	0.5	0.25	-0.75	0.0	2.0073
				$\pi/6$	2.0533
				$\pi/3$	2.1409

In table 7.3 the numerical values of Sherwood number are computed for the parameter like chemical reaction parameter, temperature difference parameter, activation energy

parameter and diffusion Biot number. Calculations show that by increasing chemical reaction parameter and temperature difference parameter the Sherwood number increase while the reverse trend can be notice in case of increasing activation energy parameter and diffusion Biot number.

Table-7.3: Computational values of Sherwood number at fixed value

$Pr = 7, Sc = 10, n = M = \beta_2 = Ec = 0.5, \gamma = Nt = Nb = 0.25, \psi = \pi/4, \alpha^* = -1, Bi = 0.3$

β_3	$\tilde{\delta}$	E_A	Bj	$-\phi'(0)$
0	0.5	0.5	0.3	0.2957
1				0.2998
2				0.3019
1	0			0.2994
	0.4			0.2997
	1			0.3001
1	0.5	0.0		0.3011
		0.2		0.3006
		0.5		0.2998
1	0.5	0.25	0.1	0.3019
			0.2	0.3012
			0.3	0.2997

In table 7.4 the Nusselt number and Sherwood number are computed numerically for the parameter like Casson fluid parameter, magnetic parameter, curvature parameter, Eckert number, thermophoretic parameter, Brownian parameter, magnetic field inclination, suction parameter and thermal Biot number. From results we perceived that by raising Casson fluid parameter, Suction parameter and thermal Biot number the Nusselt number increases while Sherwood number declines. By increasing magnetic field parameter, Curvature parameter, Eckert number, thermophoretic parameter and magnetic field inclination the Nusselt number decreases while Sherwood number increases. By enhancing the Brownian parameter both the Nusselt number as well as Sherwood number depicts decreasing trend.

Table-7.4: Numerical computation of Nusselt number and Sherwood number at fixed values of $Pr = 7, Sc = 10, n = \tilde{\delta} = \beta_3 = E_A = 0.5, Bj = 0.3$

β_2	M	γ	Ec	Nt	Nb	ψ	Bi	α^*	$-\theta'(0)$	$-\phi'(0)$
0.5	0.5	0.25	0.5	0.25	0.25	$\pi/4$	0.3	-1	0.1228	0.2976
1									0.1440	0.2962
1.5									0.1517	0.2957
1	0								0.1599	0.2950
	0.4								0.1496	0.2958
	1								0.0994	0.2996
1	0.5	0.0							0.1601	0.2941
		0.2							0.1475	0.2957
		0.5							0.1254	0.2988
1	0.5	0.25	0						0.2881	0.2854
			0.25						0.2191	0.2906
			0.75						0.1119	0.2986
1	0.5	0.25	0.5	0.1					0.1529	0.2935
				0.2					0.1472	0.2952
				0.5					0.1221	0.3034
1	0.5	0.25	0.5	0.25	0.1				0.1446	0.3022
					0.2				0.1442	0.2972
					0.5				0.1429	0.2942
1	0.5	0.25	0.5	0.25	0.25	0.0			0.1599	0.2950
						$\pi/6$			0.1519	0.2956
						$\pi/3$			0.1363	0.2968
1	0.5	0.25	0.5	0.25	0.25	$\pi/4$	0.1		0.0497	0.2983
							0.3		0.1440	0.2962
							0.5		0.2320	0.2943
1	0.5	0.25	0.5	0.25	0.25	$\pi/4$	0.2	-0.2	0.0240	0.3132
								-0.5	0.0565	0.3046
								-1	0.0977	0.2972

Chapter 8

Hydromagnetic Solid-Liquid Pulsatile Flow through Concentric Cylinders in a Porous Medium

8.1 Introduction

The current chapter is reported about hydromagnetic solid-liquid flow in an annulus between two concentric circular cylinders in porous media. The impact of Joule heating is also account for. Unlike the usually applied constant pressure gradient, the pulsatile pressure gradient is employed. The flow problem is first modeled and then tackled by Runge-Kutta-Fehlberg fourth-fifth order (RKF45) numerical scheme along with shooting algorithm. The impacts of emerging parameters namely magnetic field parameter and porosity parameter on velocity and temperature distributions are displayed via graphs and briefly addressed.

8.2 Geometry of Problem

In current chapter, two-fluid mathematical model is adopted, which is used to deal with the solid particle phase as a continuum and the volume fraction of particle phase is above 10%. Solid phase and fluid phase are established with separate control equations. Let us assume that the annular gap between two coaxial circular cylinders of infinite length is packed with laminar, incompressible, viscous and electrically conducting fluid comprising a mixture of solid particles of spherical shaped and of radius r_p. The pulsatile pressure gradient is applied to generate the fluid motion. The external magnetic field B_0 is imposed in transverse radial direction. The induced magnetic field is supposed to be negligible for low magnetic Reynolds number. For the purpose of mathematical modeling, cylindrical coordinate system (r, x) is taken in which r represents the radial direction and x expresses the axial direction. The flow schematic of the current problem is displayed in figure 8.1.

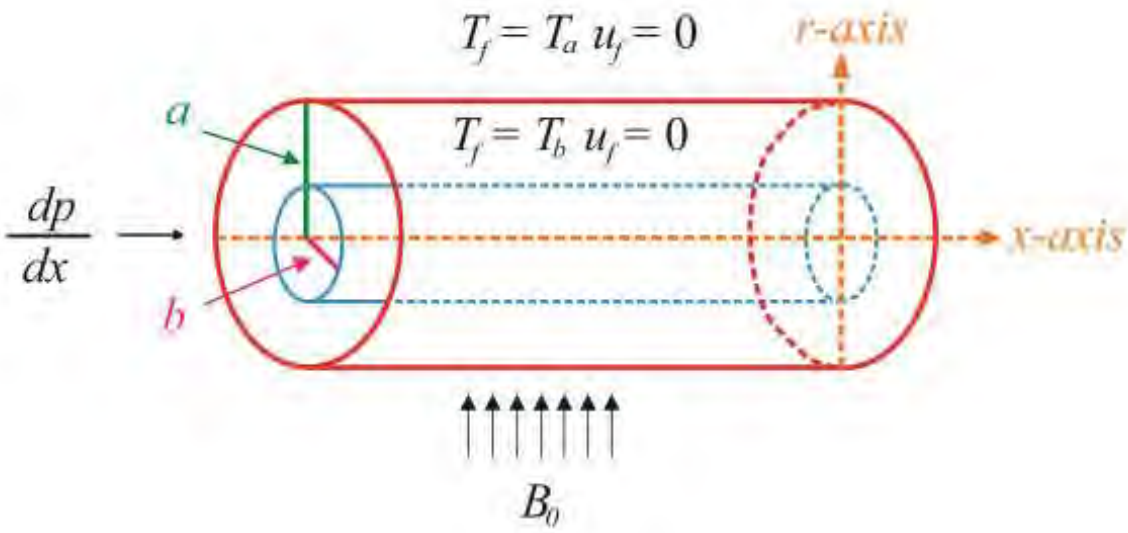

Figure 8.1: Flow schematic, coordinates and geometrical variables.

8.3 Mathematical Formulation

In current chapter, the following assumptions are made about dusty fluid flow.

- Solid particles are assumed of equal size and mass and are spherical in shape.
- The bulk concentration of the solid particles is very low such that the Reynolds number, which is based on relative particle-fluid motion is small as compared to unity, so the net influence of particles on fluid corresponds to only drag force given by Stokes.
- The gravitational force and interaction forces like Basset force etc. have been ignored.
- The low particles concentration has been chosen such that the interaction between particle-particle is minor but large enough for the particulate phase to form a pseudo-fluid.
- The solid-liquid flow may be considered as two-phase flow.
- The pressure related to particle cloud is negligible because of improbability in local particle motion.
- The viscosity of solid phase is taken zero.

Under the above stated suppositions the two-fluid model describing mass conservation, momentum conservation and energy conversion of fluid phase and particle phase are reduced in the subsequent form as follows:

$$\frac{\partial}{\partial t}\left[(1-C)\rho_f\right]+\frac{1}{r}\frac{\partial}{\partial r}\left[r(1-C)\rho_f u_f\right]=0, \tag{8.1}$$

$$\frac{\partial}{\partial t}\left[C\rho_p\right]+\frac{1}{r}\frac{\partial}{\partial r}\left[rC\rho_p u_p\right]=0, \tag{8.2}$$

$$\rho_f(1-C)\frac{\partial u_f}{\partial t}=(1-C)\left[-\frac{\partial p}{\partial x}+\mu_f\left(\frac{\partial^2 u_f}{\partial r^2}+\frac{1}{r}\frac{\partial u_f}{\partial r}\right)\right]+\frac{CS}{\tau_v}(u_p-u_f) -\frac{\mu_f}{k_1}u_f-\sigma B_0^2 u_f, \tag{8.3}$$

$$\rho_p C\frac{\partial u_p}{\partial t}=-\frac{CS}{\tau_v}(u_p-u_f), \tag{8.4}$$

$$\rho_f c_f(1-C)\frac{\partial T_f}{\partial t}=(1-C)\left[k_f\left(\frac{\partial^2 T_f}{\partial r^2}+\frac{1}{r}\frac{\partial T_f}{\partial r}\right)\right]+\frac{CS}{\tau_v}(u_p-u_f)^2 +\frac{C\rho_p c_p}{\tau_T}(T_p-T_f)+\sigma B_0^2 u_f^2, \tag{8.5}$$

$$\rho_p c_p C\frac{\partial T_p}{\partial t}=-\frac{\rho_p c_p C}{\tau_T}(T_p-T_f). \tag{8.6}$$

The set of applicable boundary conditions is given by:

$$u_f=0,\ T_f=T_a \quad \text{at } r=a, \tag{8.7}$$

$$u_f=0,\ T_f=T_b \quad \text{at } r=b. \tag{8.8}$$

The mathematical correlation for classical Stokes drag coefficient S is obtained by Tam [116] which is defined in subsequent Eq. (8.9:

Table 8.1: Physical properties of water and copper particles

Physical property	Symbol	SI Unit	Water H_2O	Copper Cu
Density	ρ	kgm^{-3}	999	3980
Thermal heat capacity	c_p	$Jkg^{-1}K^{-1}$	4187	840
Thermal conductivity	k	$Wm^{-1}K^{-1}$	0.60	33
Dynamic viscosity	μ	$Pa.s$	8.90×10^{-4}	-
Diameter of particle	d_p	mm	-	0.44

$$S=\frac{9\mu_f}{2r_p^2}\tilde{\lambda}(C) \quad \text{where} \quad \tilde{\lambda}(C)=\frac{4+3\sqrt{8C-3C^2}+3C}{(2-3C)^2}. \tag{8.9}$$

The similar form can be achieved by using following similarity transforms:

$$\eta=\frac{r}{a-b},\xi=\frac{x}{a-b},t^*=t\omega,u_{f,p}^*=\frac{u_{f,p}}{U},\theta_{f,p}=\frac{T_{f,p}-T_b}{T_a-T_b},p^*=\frac{p}{A(a-b)}, \tag{8.10}$$

The resulting momentum and energy conservation laws for both phases in dimensionless form can be written as follows:

$$\frac{\partial u_f}{\partial t}=-\hat{\beta}\frac{\partial p}{\partial \xi}+\hat{\beta}\left(\frac{\partial^2 u_f}{\partial \eta^2}+\frac{1}{\eta}\frac{\partial u_f}{\partial \eta}\right)+\frac{CN\hat{\beta}}{1-C}\left(u_p-u_f\right)-\frac{\left(M^2\hat{\beta}+K\right)}{\hat{\beta}(1-C)}u_f, \tag{8.11}$$

$$\frac{\partial \theta_f}{\partial t}=\frac{\hat{\beta}}{Pr}\left(\frac{\partial^2 \theta_f}{\partial \eta^2}+\frac{1}{\eta}\frac{\partial \theta_f}{\partial \eta}\right)+\frac{CNEc\hat{\beta}}{1-C}\left(u_p-u_f\right)^2+\frac{M^2\hat{\beta}Ec}{1-C}u_f^2 + \frac{2C\varsigma\tilde{\alpha}}{3Pr\delta(1-C)}\left(\theta_p-\theta_f\right), \tag{8.12}$$

$$\frac{\partial u_p}{\partial t}=-\frac{N\hat{\beta}}{\varsigma}\left(u_p-u_f\right), \tag{8.13}$$

$$\frac{\partial \theta_p}{\partial t}=-\frac{2\tilde{\alpha}}{3Pr\delta}\left(\theta_p-\theta_f\right). \tag{8.14}$$

For calculation convenience, asterisks are omitted. The non-dimensional form of boundary conditions is given as follows:

$$u_f=0,\ \ \theta_f=1 \ \text{ at } \ \eta=\eta_a, \tag{8.15}$$

$$u_f=0,\ \ \theta_f=0 \ \text{ at } \ \eta=\eta_b. \tag{8.16}$$

The dimensionless parameters appearing in Eq. (8.11) to Eq. (8.14) are expressed as:

$$\left.\begin{aligned}
&\hat{\beta}=\frac{\nu_f}{(a-b)^2\omega}=\frac{\beta_1}{(1-\chi)^2},\beta_1=\frac{\nu_f}{\omega a^2},Re=\frac{A(a-b)^3}{\rho_f {\nu_f}^2},U=\frac{A(a-b)^2}{\mu_f},\\
&\varsigma=\frac{\rho_s}{\rho_f},\tilde{\alpha}=\frac{1}{\omega\tau_v},N=\frac{S(a-b)^2}{\tau_v\mu_f},M=B_0(a-b)\sqrt{\frac{\sigma}{\mu_f}},K=\frac{\nu_f}{\omega k_1},\\
&\delta=\frac{c_s}{c_f},Pr=\frac{\mu_f c_f}{k_f},Ec=\frac{U^2}{c_f(T_a-T_b)},\chi=\frac{b}{a},\tau_v=\frac{2}{3Pr\delta}\tau_T
\end{aligned}\right\}, \tag{8.17}$$

The non-dimensional form of oscillating pressure gradient can be expressed as:

$$-\frac{\partial p}{\partial \xi} = 1 + \varepsilon \cos t, \tag{8.18}$$

8.4 Solution Procedure

For the sake of solution convenience, we have introduced complex variables so that its real parts represent the physical entities. Hence Eq. (8.18) can be rewritten as:

$$-\frac{\partial p}{\partial \xi} = 1 + \varepsilon e^{it}, \tag{8.19}$$

The assumed form of solution is given by:

$$\left.\begin{aligned} u_{f,p}(\eta,t) &= u_{f_0,p_0}(\eta) + \varepsilon u_{f_1,p_1}(\eta) e^{it} \\ \theta_{f,p}(\eta,t) &= \theta_{f_0,p_0}(\eta) + \varepsilon \theta_{f_1,p_1}(\eta) e^{it} + \varepsilon^2 \theta_{f_2,p_2}(\eta) e^{2it} \end{aligned}\right\}, \tag{8.20}$$

After substituting Eq. (8.20) in Eq. (8.11) to Eq. (8.14) and then separating the terms of orders $\varepsilon^0, \varepsilon^1, \varepsilon^2$, we get the resulting three sets of ordinary differential equations:

$$O(\varepsilon^0): \quad \left.\begin{aligned} &\frac{d^2 u_{f_0}}{d\eta^2} + \frac{1}{\eta}\frac{du_{f_0}}{d\eta} + \frac{CN}{(1-C)}\left(u_{p_0} - u_{f_0}\right) - \frac{M^2\hat{\beta} + K}{\hat{\beta}(1-C)} u_{f_0} + 1 = 0, \\ &\frac{N\hat{\beta}}{\varsigma}\left(u_{p_0} - u_{f_0}\right) = 0, \\ &\frac{d^2\theta_{f_0}}{d\eta^2} + \frac{1}{\eta}\frac{d\theta_{f_0}}{d\eta} + \frac{M^2\hat{\beta}Ec}{1-C} u_{f_0}^2 + \frac{NPrEcC}{1-C}\left(u_{p_0} - u_{f_0}\right)^2 \\ &\qquad + \frac{2\varsigma\tilde{\alpha}C}{3\hat{\beta}\delta(1-C)}\left(\theta_{p_0} - \theta_{f_0}\right) = 0, \\ &\frac{2\tilde{\alpha}}{3Pr\delta}\left(\theta_{p_0} - \theta_{f_0}\right) = 0. \end{aligned}\right\}, \tag{8.21}$$

$$O(\varepsilon^1):\quad \left.\begin{aligned} &\frac{d^2u_{f_1}}{d\eta^2}+\frac{1}{\eta}\frac{du_{f_1}}{d\eta}+\frac{CN}{1-C}\left(u_{p_1}-u_{f_1}\right)-\frac{M^2\bar{\beta}+K}{\hat{\beta}(1-C)}u_{f_1}\\ &\qquad\qquad -\frac{i}{\hat{\beta}}u_{f_1}+1=0,\\ &\frac{N\hat{\beta}}{\varsigma}\left(u_{p_1}-u_1\right)+iu_{p_1}=0,\\ &\frac{d^2\theta_{f_1}}{d\eta^2}+\frac{1}{\eta}\frac{d\theta_{f_1}}{d\eta}+\frac{2C}{1-C}NPrEc\left(u_{p_0}-u_{f_0}\right)\left(u_{p_1}-u_{f_1}\right)\\ &\quad+\frac{2M^2Ec}{1-C}u_{f_0}u_{f_1}+\frac{2C\varsigma\tilde{\alpha}}{3\hat{\beta}\delta(1-C)}\left(\theta_{p_1}-\theta_{f_1}\right)-i\theta_{f_1}=0,\\ &\frac{2\tilde{\alpha}}{3Pr\delta}\left(\theta_{p_1}-\theta_1\right)+i\theta_{p_1}=0. \end{aligned}\right\}, \tag{8.22}$$

$$O(\varepsilon^2):\quad \left.\begin{aligned} &\frac{d^2\theta_{f_2}}{d\eta^2}+\frac{1}{\eta}\frac{d\theta_{f_2}}{d\eta}+\frac{M^2Ec}{1-C}u_{f_1}^2+\frac{NEcPrC}{1-C}\left(u_{p_1}-u_{f_1}\right)^2\\ &\qquad+\frac{2C\varsigma\tilde{\alpha}}{3(1-C)\hat{\beta}\delta}\left(\theta_{p_2}-\theta_{f_2}\right)-i\frac{2Pr}{\hat{\beta}}\theta_{f_2}=0,\\ &\frac{2\tilde{\alpha}}{3Pr\delta}\left(\theta_{p_2}-\theta_{f_2}\right)+i\theta_{p_2}=0. \end{aligned}\right\}, \tag{8.23}$$

The corresponding set of boundary conditions is given in dimensionless form:

$$\left.\begin{aligned} &u_{f_0}=u_{f_1}=\theta_{f_1}=\theta_{f_2}=0,\theta_{f_0}=1 \text{ at } \eta=\eta_a\\ &u_{f_0}=u_{f_1}=\theta_{f_0}=\theta_{f_1}=\theta_{f_2}=0 \quad \text{at } \eta=\eta_b \end{aligned}\right\}, \tag{8.24}$$

The above three sets of equations from Eq. (8.21) to Eq. (8.23) along with boundary conditions Eq. (8.24) is handled by Runge-Kutta-Fehlberg technique (RKF45) along with shooting algorithm in Matlab software. Here ε is dimensionless small quantity shows magnitude of oscillating wave.

8.5 Illustration of Results

We have investigated the hydromagnetic solid-liquid flow through concentric circular cylinders inserted in a porous media under an oscillating pressure gradient. The spherical particles of copper Cu and water as carrier fluid are considered and their physical properties are mentioned in table 8.1. The influence of Joule heating is also taken. The resulting system of equations is handled by Runge-Kutta-Fehlberg numerical technique of order fourth-fifth (RKF45) with shooting algorithm and the

outcomes are displayed through graphs. In whole computation, some parameters are fixed $Pr = 6.2,\ \varsigma = 3.9,\ \delta = 0.2$. The graphs of velocity and temperature distributions versus numerous parameters are drawn through figures 8.2 to 8.12.

Figures 8.2 to 8.5 display the influence of magnetic field parameter M and porosity parameter *K* on steady-state velocity distribution for both fluid and solid phases. Magnetic field yields a force called "Lorentz force", which opposes the flow so that the velocity of fluid phase u_{f_0} as well as solid phase u_{p_0} decreases. Increasing porosity parameter *K* decreases the velocity distribution for both phases, as a consequence of growing damping force on fluid velocity which decreases u_{f_0} and consequently decreases particles phase velocity u_{p_0}. Figure 8.6 and 8.7 exhibits the impact of magnetic parameter M and porosity parameter *K* on unsteady velocity distribution for both phases. By enhancing the strength of magnetic field and porosity parameter, the velocity distribution of fluid phase u_{f_1} as well as solid phase u_{p_1} decreases. It is seen that the amplitude of solid phase velocity u_{f_1} is less than fluid phase velocity distribution u_{p_1}. Figure 8.8 depicts the steady-state temperature profile for various values of porosity parameter *K*. It is observed that no significant variation for various values of parameter *K*.

Figures 8.9 and 8.10 represent the impact of porosity parameter *K* and magnetic field parameter *M* on first unsteady part of temperature distribution $\theta_1(\eta)$ for both fluid and solid phase. From figure 8.9, we found that by increasing porosity parameter *K* the temperature distribution $\theta_1(\eta)$ for both phases decreases because of increasing damping force. And from figure 8.10, we have observed that by enhancing magnetic field strength the temperature distribution $\theta_1(\eta)$ of both phases is enhanced due to opposing Lorentz force. Figures 8.11 and 8.12 represent the impact of magnetic field parameter *M* and porosity parameter *K* on second unsteady part of temperature distribution $\theta_2(\eta)$ for both fluid and solid phase. From figure 8.11, we have realized that temperature distribution $\theta_2(\eta)$ for both phases increases by increasing magnetic field strength. In figure 8.12, we have seen that the temperature distribution $\theta_2(\eta)$

decreases by increasing porosity parameter K for both fluid and solid phases. We observed that the magnitude of fluid temperature is higher than that of solid particles.

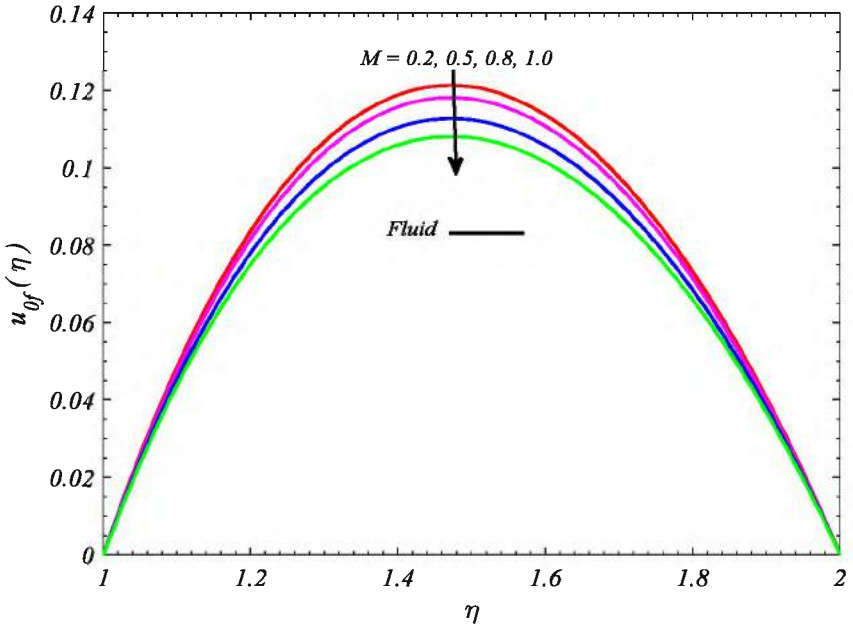

Figure 8.2: Impact of magnetic parameter on steady-state velocity of fluid phase.

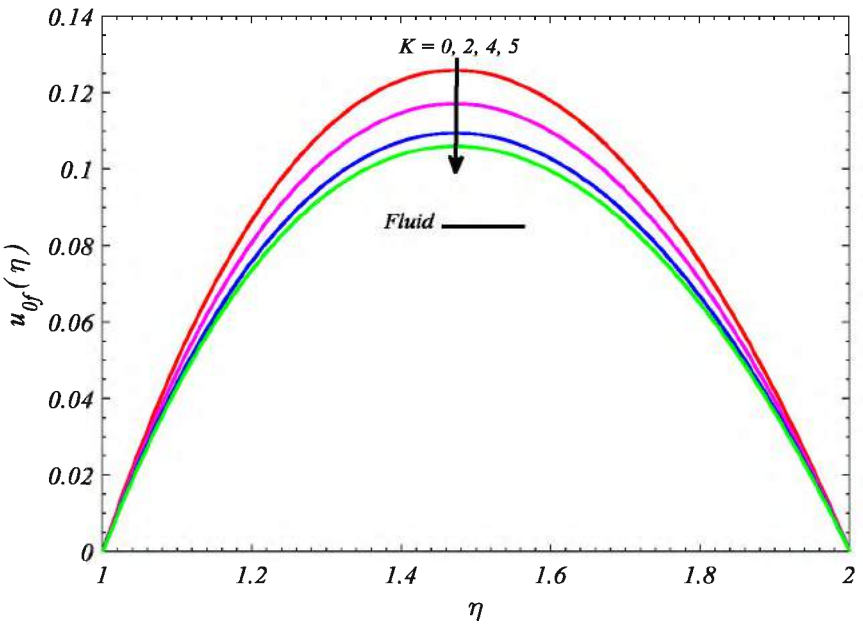

Figure 8.3: Impact of porosity parameter on steady-state velocity of fluid phase.

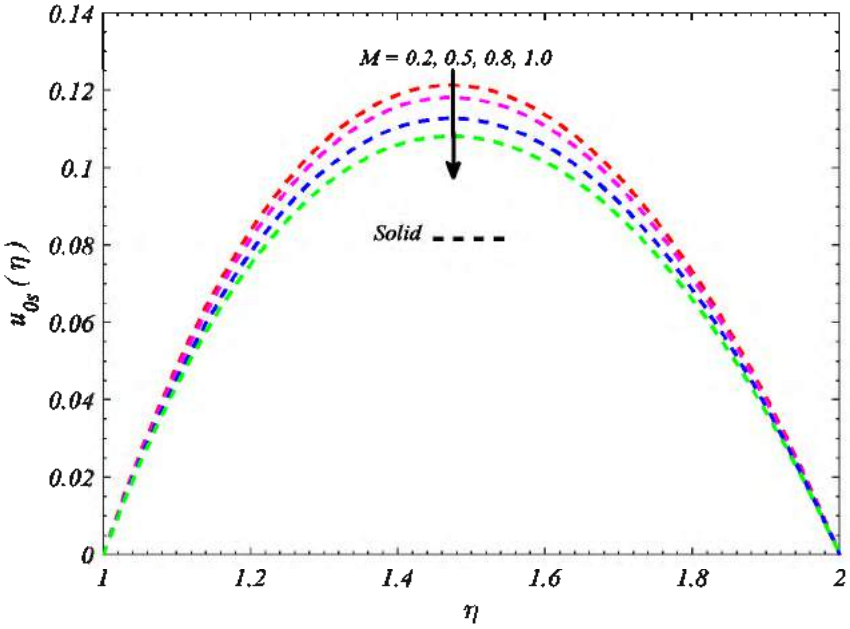

Figure 8.4: Impact of magnetic parameter on steady-state velocity of solid phase.

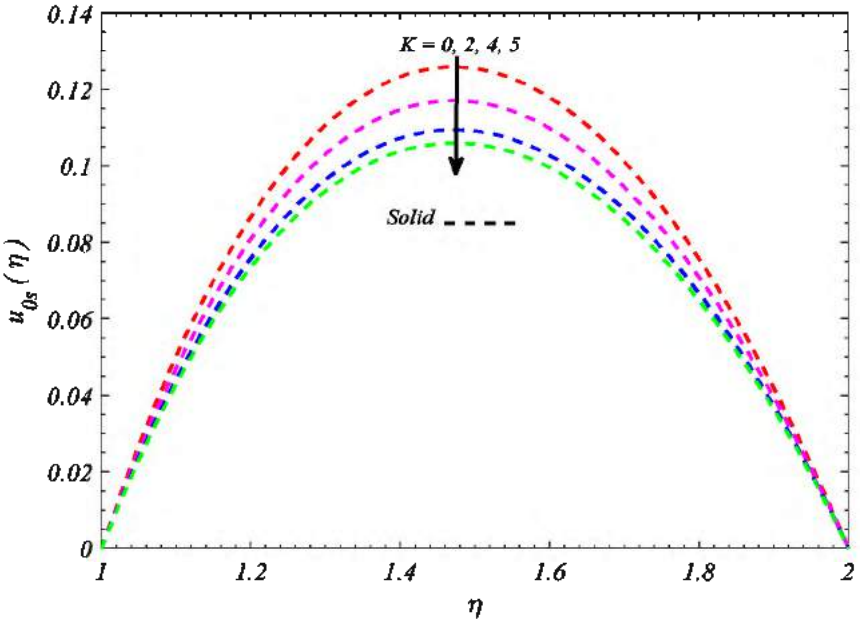

Figure 8.5: Impact of porosity parameter on steady-state velocity of solid phase.

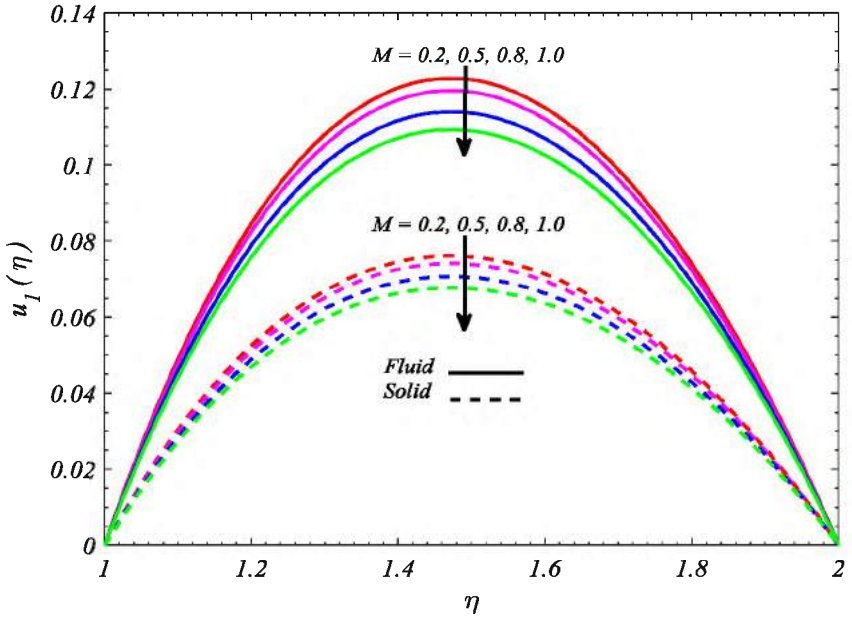

Figure 8.6: Impact of magnetic parameter on first unsteady velocity of both phases.

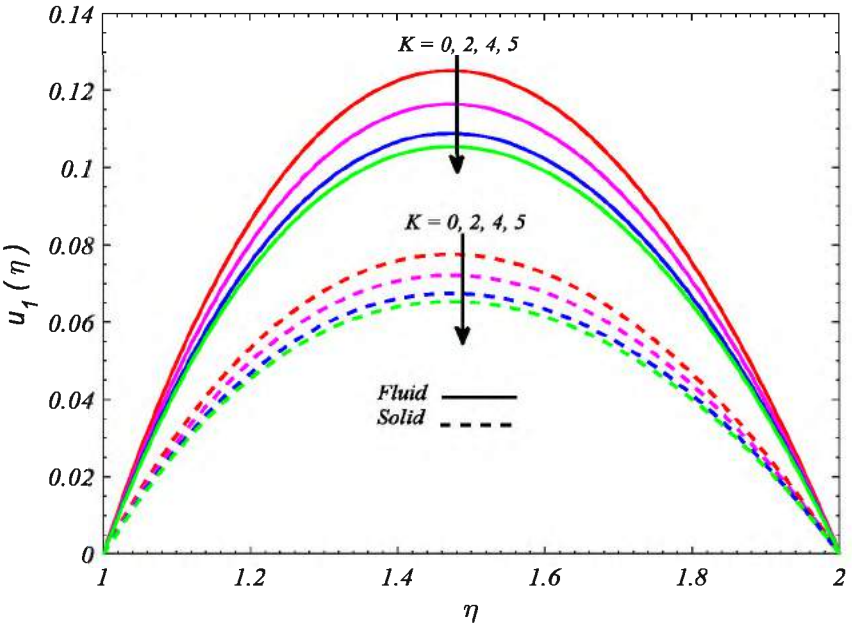

Figure 8.7: Impact of porosity parameter on first unsteady velocity of both phases.

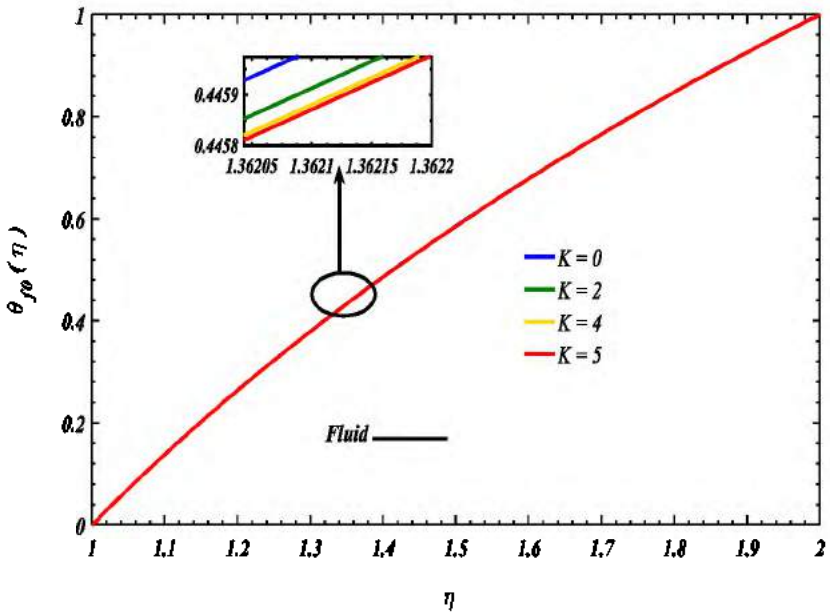

Figure 8.8: Impact of porosity parameter on steady-state temperature of fluid phase.

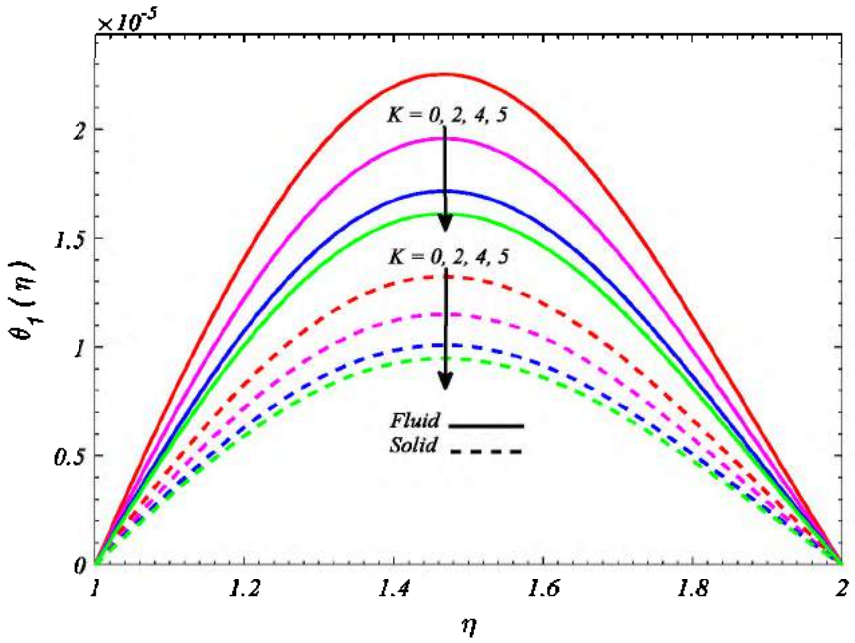

Figure 8.9: Impact of porosity parameter on first unsteady temperature of both phases.

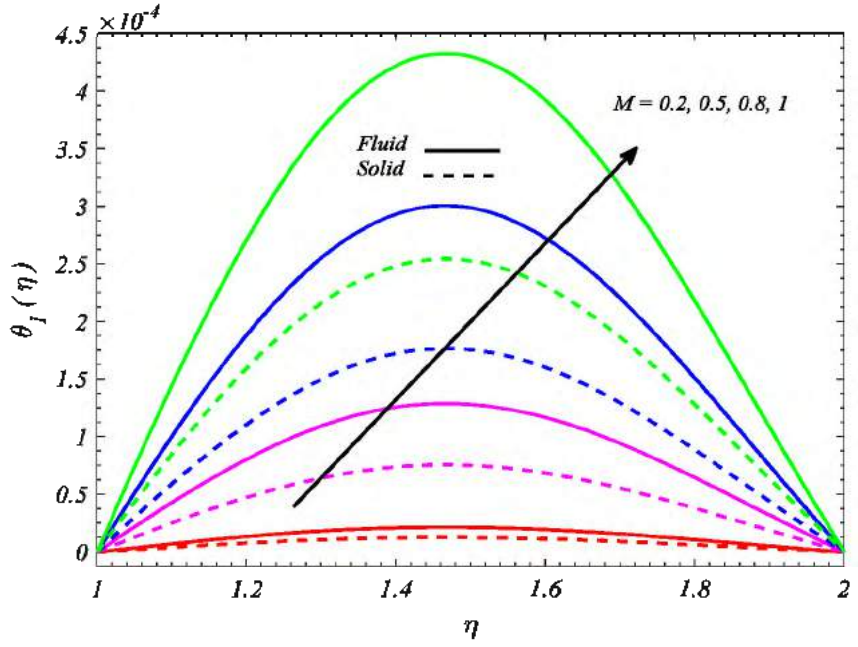

Figure 8.10: Impact of magnetic parameter on first unsteady temperature of both phases.

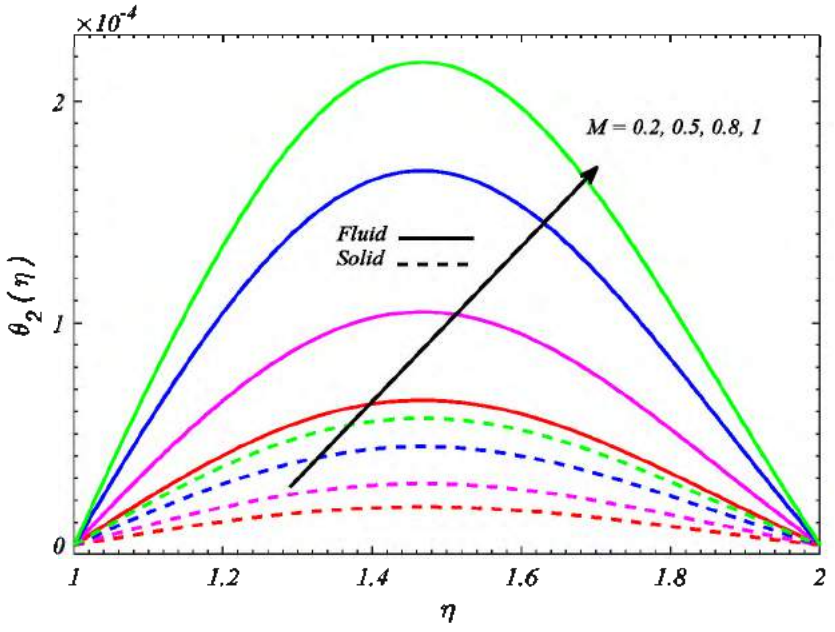

Figure 8.11: Impact of magnetic parameter on second unsteady temperature of both phases.

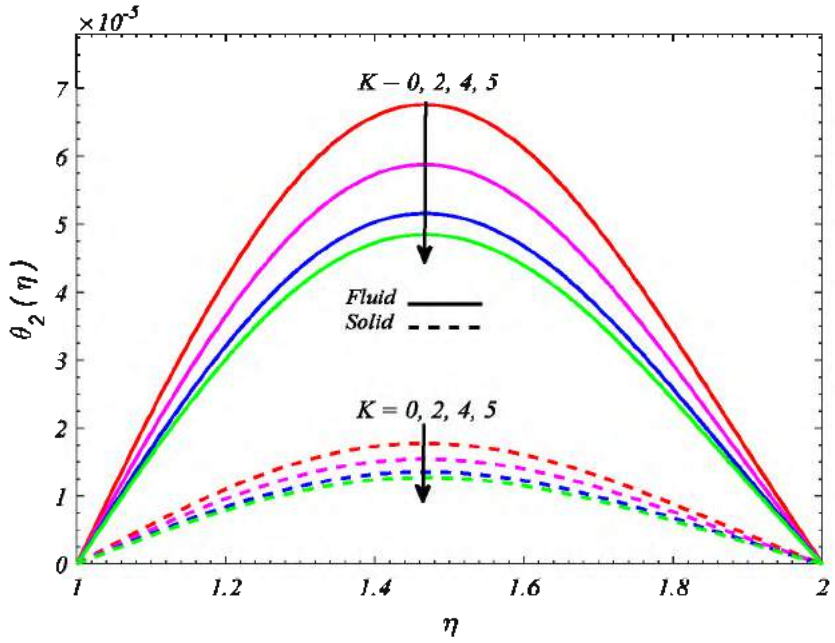

Figure 8.12: Impact of porosity parameter on second unsteady temperature of both phases.

Chapter 9

Hydromagnetic Transport of Dust Particles in Optically Thick Gas Flow over an Inclined Plane with Thermal Radiation

9.1 Introduction

In present chapter, hydromagnetic transport of dust particles in gas flow over an inclined plane is examined under the influence of viscous dissipation and thermal radiation. The Rosseland diffusion flux model is utilized for thermal radiation effects. The resulting non-linear ordinary differential equations are reduced into similar form via suitable similarity transforms and then tackled numerically by Runge-Kutta-Fehlberg method with shooting algorithm. Influences of numerous emergent parameters on flow features like velocities, temperature distributions and Nusselt number are reflected graphically and discussed in detail.

9.2 Geometry of Problem

Let us assume a two dimensional, steady, laminar, incompressible and boundary layer viscous gas flow over an inclined plane. The plane is inclined at an angle α as displayed in figure. 9.1.

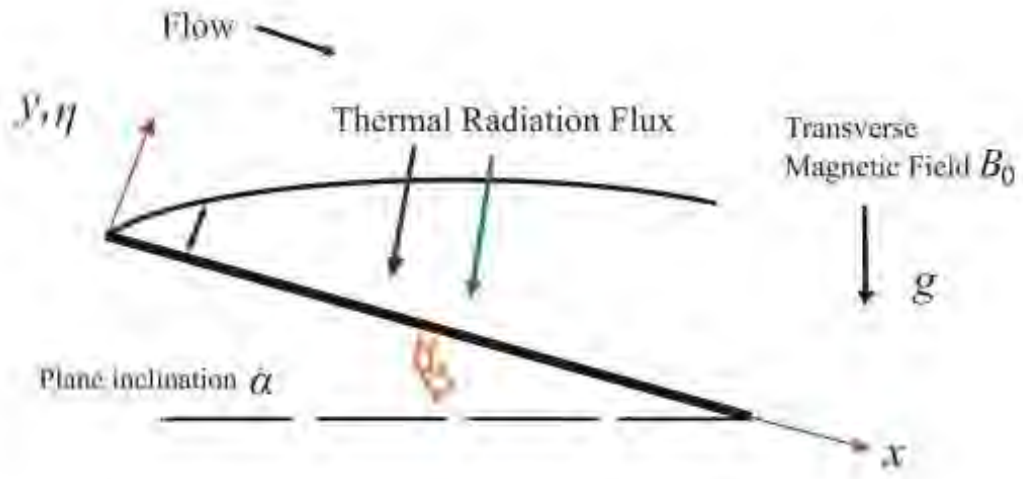

Figure 9.1: Flow schematic, coordinates and geometrical variables.

The gas is considered to be electrically conducting, optically-thick, absorbing-emitting and non-scattering. The transverse magnetic field $\mathbf{B} = B_0 \hat{j}$ is taken. The spherical dust particles of uniform size are considered and particles number density is fixed throughout the problem.

9.3 Mathematical Formulation

Under above-mentioned assumptions with Boussinesq's approximation, the governing equations can be expressed as below:

For gas phase

$$\frac{\partial u}{\partial x} + \frac{\partial v}{\partial y} = 0, \tag{9.1}$$

$$\rho\left(u\frac{\partial u}{\partial x} + v\frac{\partial v}{\partial y} \right) = \mu\frac{\partial^2 u}{\partial y^2} + SN\left[u_p - u \right] + \rho g\beta\left(T - T_\infty \right)\cos\alpha - \sigma B_0^2 u, \tag{9.2}$$

$$\rho c_p\left(u\frac{\partial T}{\partial x} + v\frac{\partial T}{\partial y} \right) = k\frac{\partial^2 T}{\partial y^2} + \frac{Nc_p}{\tau_T}\left(T_p - T \right) - \frac{\partial Q_r}{\partial y} + \mu\left(\frac{\partial u}{\partial y} \right)^2 + Q_0. \tag{9.3}$$

For dust particle phase

$$\frac{\partial(\rho_p u_p)}{\partial x} + \frac{\partial\left(\rho_p v_p\right)}{\partial y} = 0, \tag{9.4}$$

$$u_p\frac{\partial u_p}{\partial x} + v_p\frac{\partial u_p}{\partial y} = \frac{S}{m}\left(u - u_p \right), \tag{9.5}$$

$$u_p\frac{\partial v_p}{\partial x} + v_p\frac{\partial v_p}{\partial y} = \frac{S}{m}\left(v - v_p \right), \tag{9.6}$$

$$u_p\frac{\partial T_p}{\partial x} + v_p\frac{\partial T_p}{\partial y} = -\frac{c_p}{c_m\tau_T}\left(T_p - T \right). \tag{9.7}$$

The radiative heat flux Q_r via Rosseland model [101] is given as follows:

$$Q_r = -\frac{4\sigma^*}{3k^*}\frac{\partial T^4}{\partial y}, \tag{9.8}$$

We have considered sufficiently small temperature differences within the flow. Taylor series expansion of T^4 about T_∞ after ignoring non-linear terms, we got:

$$T^4 \cong 4T_\infty^3 T - 3T_\infty^4, \tag{9.9}$$

Using Eq. (9.9) in Eq. (9.8), the radiative flux Q_r takes the following form:

$$Q_r = -\frac{16T_\infty^3\sigma^*}{3k^*}\frac{\partial T}{\partial y}, \tag{9.10}$$

The mathematical form of heat sink Q_0 is given as follows:

$$Q_0 = \frac{kU_0^2}{\nu^2}\left[A\left(T_w - T_\infty\right)e^{-\eta} + B\left(T - T_\infty\right)\right], \tag{9.11}$$

The appropriate set of boundary conditions for the flow phenomenon is given as follows:

$$\begin{aligned} u = u_p = U_0, v = v_p = 0, T = T_p = T_w \quad \text{at} \quad y = 0, \\ u = 0,\ T \to T_\infty \ \text{as} \ y \to \infty, \end{aligned} \tag{9.12}$$

To reduce the flow problem in similar form the following similarity transformations are employed:

$$\bar{u} = \frac{u}{U_0},\ \bar{u}_p = \frac{u_p}{U_0},\ \eta = \frac{U_0}{\nu}y,\ \theta = \frac{T - T_\infty}{T_w - T_\infty},\ \theta_p = \frac{T_p - T_\infty}{T_w - T_\infty}, \tag{9.13}$$

The governing equations in dimensionless form are given as:

$$u'' + R\left(u_p - u\right) + \cos\alpha Gr\theta - Mu = 0, \tag{9.14}$$

$$\left(1 + Rd\right)\theta'' + c_1 NPrl^2\left(\theta_p - \theta\right) + Ae^{-\eta} + B\theta + PrEcu'^2 = 0, \tag{9.15}$$

$$u_p' + c_2(u_p - u) = 0, \tag{9.16}$$

$$\theta_p' + c_3(\theta_p - \theta) = 0. \tag{9.17}$$

The boundary conditions in non-dimensional are:

$$u = 1,\ u_p = 1,\ \theta = 1,\ \theta_p = 1 \quad \text{at} \quad \eta = 0, \tag{9.18}$$

$$u = 0,\ \theta = 0 \ \ as \qquad \eta \to \infty. \tag{9.19}$$

The bars are omitted for the sake of convenience. The various dimensionless parameters are appearing in the Eq. (9.14) to (9.17) are expressed as follows:

$$\left.\begin{aligned} &Rd=\frac{16\sigma^{*}T_{\infty}^{3}}{3kk^{*}},Pr=\frac{\mu c_p}{k},Ec=\frac{U_0^2}{c_p\Delta T},Gr=\frac{g\beta\Delta Tl^3}{\nu^2},\tau_T=\frac{m}{S},l=\frac{\nu}{U_0}\\ &,Re_x=\frac{xU_0}{\nu},M=\frac{\sigma B_0^2 l}{\rho U_0},R=\frac{lKN}{\rho U_0},c_1=\frac{1}{\mu\tau_T},c_2=\frac{l}{\tau_T},c_3=\frac{lc_p}{c_m\tau_T}\end{aligned}\right\}. \tag{9.20}$$

9.3.1 Physical Parameters of Interest

The Nusselt number for the current flow problem can be formulated as follows:

$$Nu=\frac{xQ_w}{k(T_w-T_\infty)},\qquad \text{where } Q_w=-\left[\left(k+\frac{16\sigma^{*}T_{\infty}^{3}}{3k^{*}}\right)\frac{\partial T}{\partial y}\right]_{y=0}, \tag{9.21}$$

using similarity transformations defined by Eq. (9.13) in Eq. (9.21), the Nusselt number in dimensionless form is written as follows:

$$Nu\left(Re_x\right)^{-1}=-\left(1+Rd\right)\theta'(0). \tag{9.22}$$

9.4 Solution Procedure

The system of Eq. (9.14) to Eq. (9.17) along with boundary conditions Eq. (9.18) and Eq. (9.19) are handled by Runge-Kutta-Fehlberg fourth-fifth order (RKF45) numerical scheme with shooting algorithm in Matlab software. For this purpose, at first the governing equations are reduced to set of 1st order ordinary differential equations. Let us assume that:

$$F_1=u,\ F_2=u',\ F_3=\theta,\ F_4=\theta',\ F_5=u_p,\ F_6=\theta_p\ , \tag{9.23}$$

the system of first-order equations is given as follows:

$$\begin{bmatrix}F_1'\\F_2'\\F_3'\\F_4'\\F_5'\\F_6'\end{bmatrix}=\begin{bmatrix}F_2\\MF_1-Gr\cos\alpha F_3-R\left(F_5-F_1\right)\\F_4\\\dfrac{-1}{1+Rd}\left\{c_1NPrl^2\left(F_6-F_3\right)+Ae^{-\eta}+BF_3+PrEcF_2^2\right\}\\-c_2\left(F_5-F_1\right)\\-c_3\left(F_6-F_3\right)\end{bmatrix}, \tag{9.24}$$

The boundary conditions can be written as follows:

$$F_1(0)=1,\ F_2(0)=s_2,\ F_3(0)=1,\ F_4(0)=s_4\ ,\ F_5(0)=1, F_6(0)=1. \qquad (9.25)$$

Where s_2, s_4 are initial guesses for missing initial conditions $F_2(0)$, $F_4(0)$. The missing initial conditions are achieved by using Newton's Raphson method and then we apply Runge-Kutta-Fehlberg numerical integrating scheme along with shooting algorithm to solve the governing equations.

9.5 Illustration of Results

In this chapter, the hydromagnetic transport of dust particles in gas flow over an inclined plane under the influence of thermal radiation is investigated. The gas is taken to be electrically conducting, optically-thick, absorbing emitting and non-scattering. The governing set of Eqs. (9.14) to Eq. (9.17) along with boundary conditions Eq. (9.18) to Eq. (9.19) is solved by Runge-Kutta-Fehlberg numerical technique along with shooting algorithm. Impact of numerous involving parameters on velocity and temperature profiles of both phases are displayed through figures.

In figure 9.2, the impact of fluid particle concentration parameter *R* on velocity profiles for gas and particles phases is presented. We observed that by increasing particle concentration parameter the flow profiles for both phases increases. Figure 9.3 depicts the flow response versus Grashof number. We found that increase of Grashof number accelerates the flow for both phases. Figure 9.4 shows behaviors of flow profiles of both phases for various values of magnetic parameter. The findings show that by increasing magnetic number the flow pattern decay progressively. Figure 9.5 demonstrates the variation of flow profiles for both phases versus plane inclination. The flow profile decelerates by increasing the plane inclination from horizontal to vertical. Figure 9.6 describes the response of temperature profiles of both phases for numerous values of radiation number. We have seen that radiation number enhances the temperature profiles for both phases.

Figure 9.7 illustrates the variation of temperature profiles for several values of Eckert number and results show an increase in temperature profiles for both phases. Figure 9.8 illustrates the impact of Prandtl number on temperature distributions for both phases. We have observed that by the increase of Prandtl number there is significant increase in temperature profiles for both phases. In figure 9.9 the impact of particles number density *N* on temperature profiles for both phases is presented. We

found that by increasing number density the temperature profiles for both phases increases. Figure 9.10 shows variation of local Nusselt number against various values of Prandtl number. The graph depicts that by enhancing radiation number the local Nusselt number decreases.

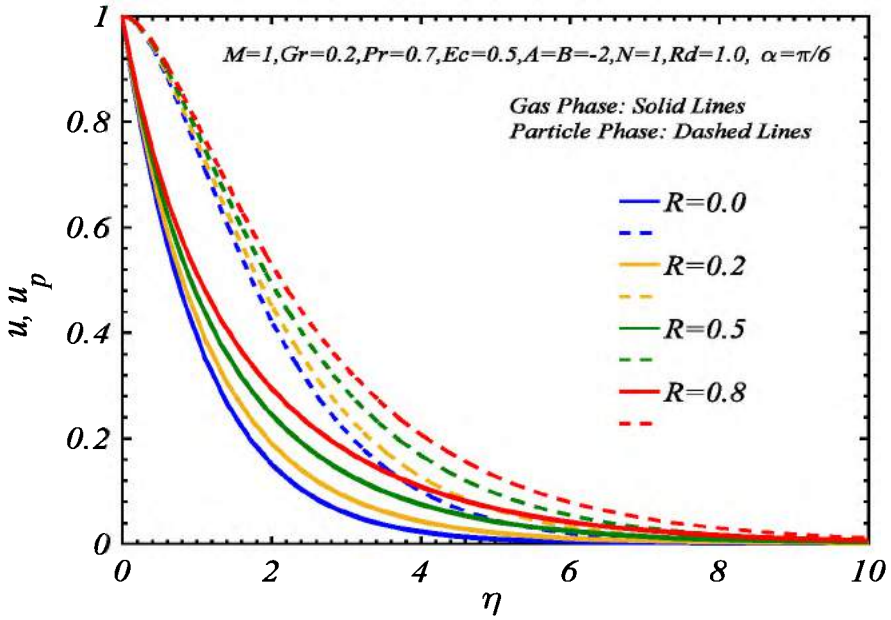

Figure 9.2: Variation of u, u_p versus *R*.

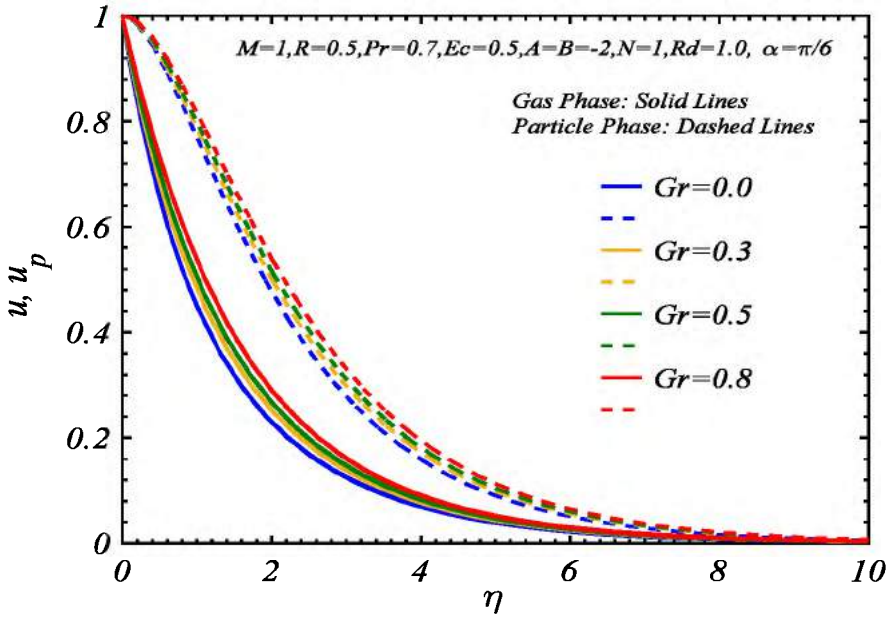

Figure 9.3: Variation of u, u_p versus *Gr*.

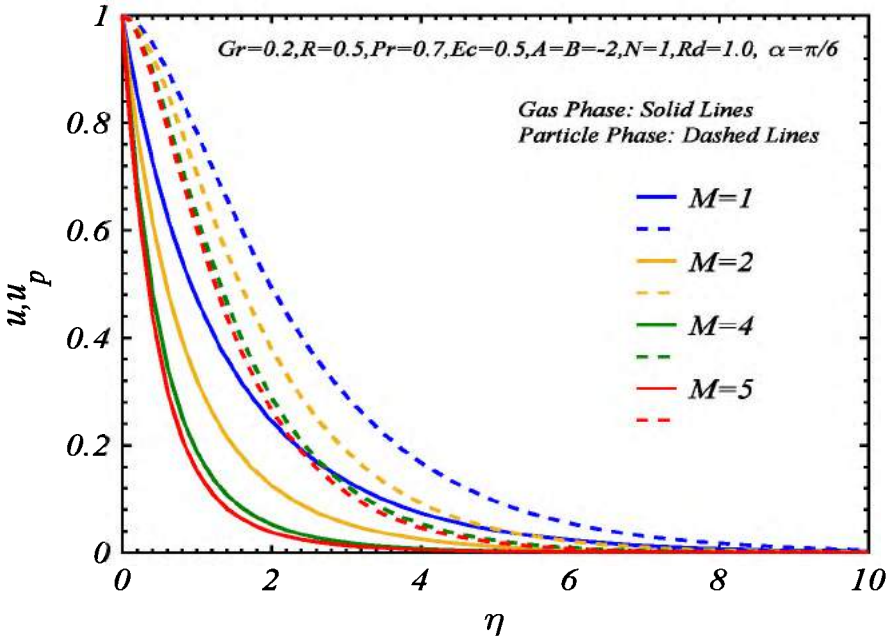

Figure 9.4: Variation of u, u_p versus *M*.

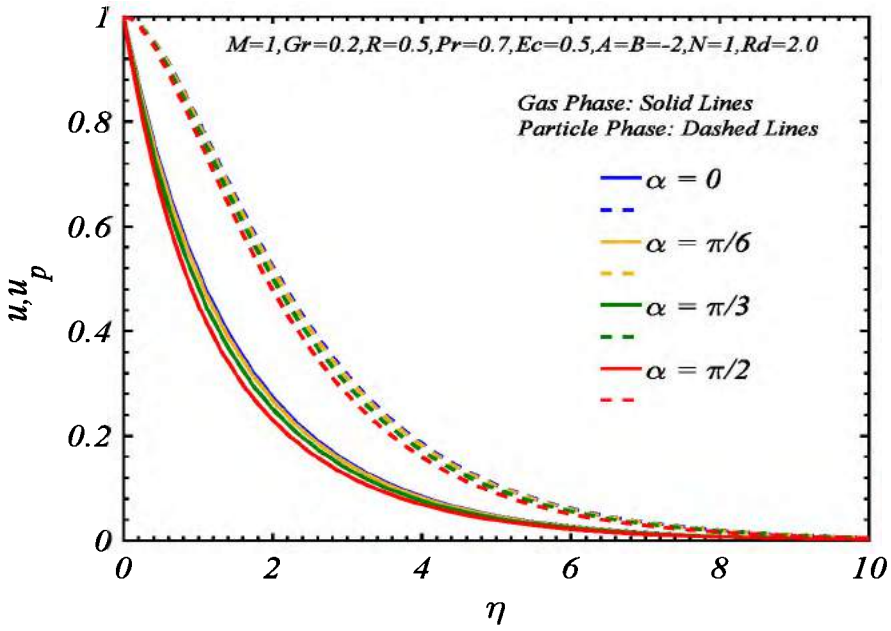

Figure 9.5: Variation of u, u_p versus α.

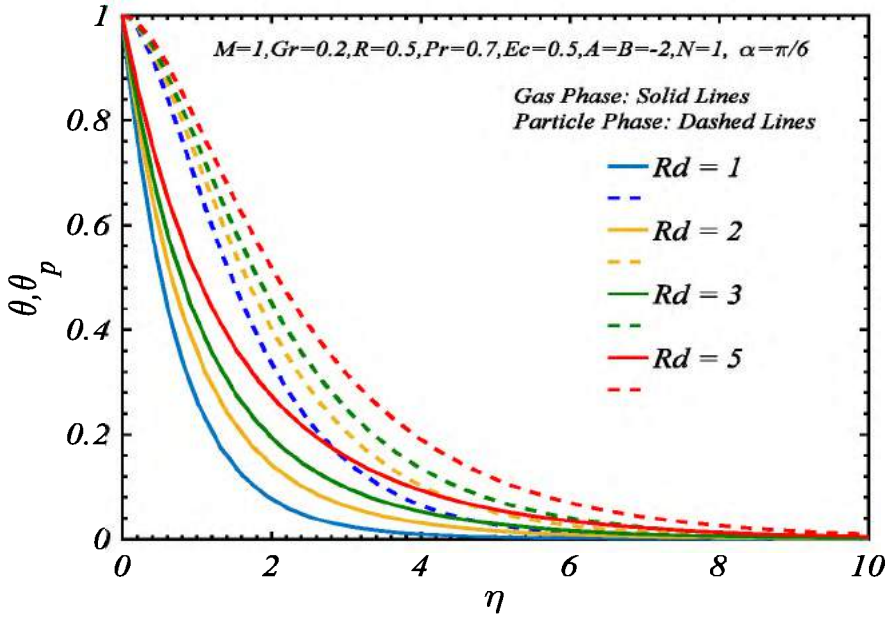

Figure 9.6: Variation of θ, θ_p versus *Rd*.

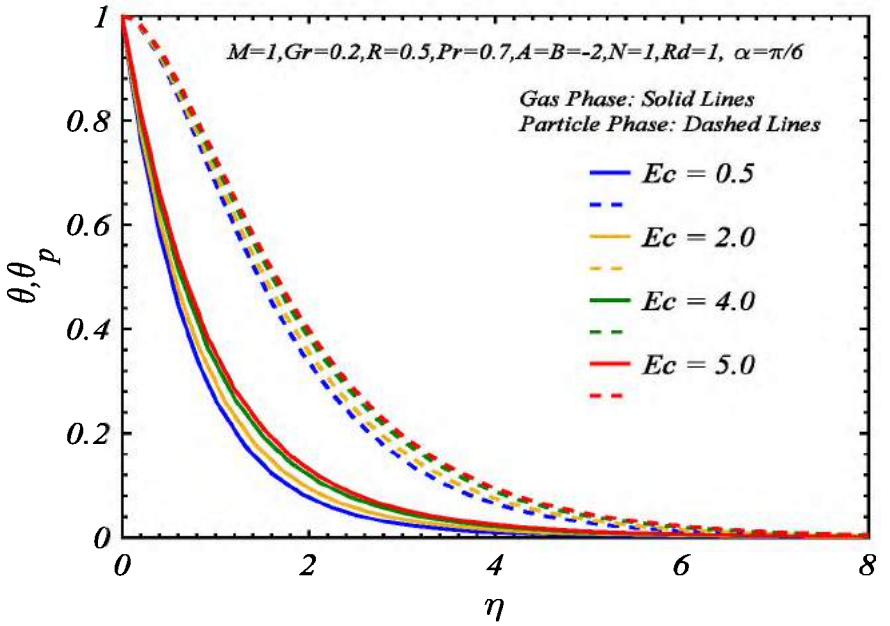

Figure 9.7: Variation of θ, θ_p versus *Ec*.

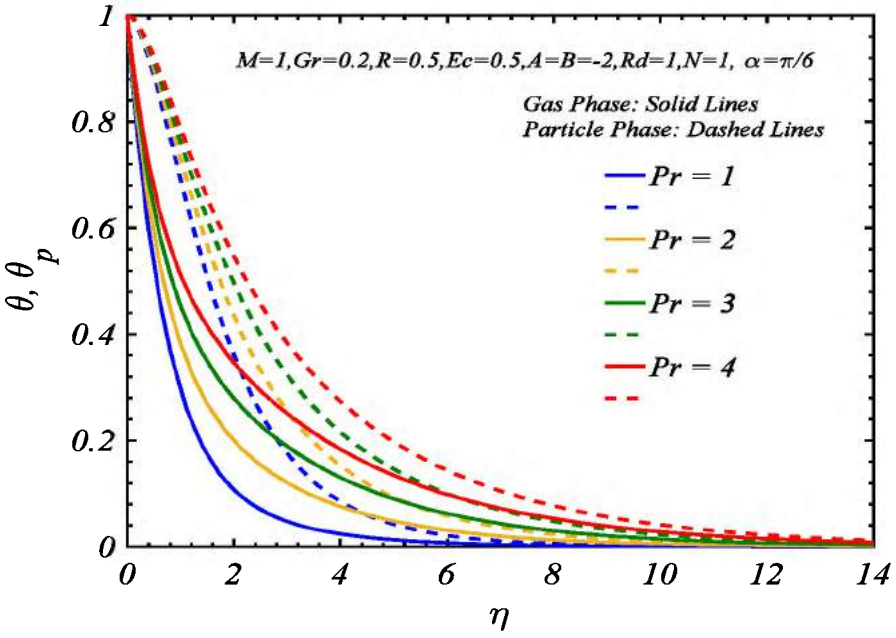

Figure 9.8: Variation of θ, θ_p versus *Pr*.

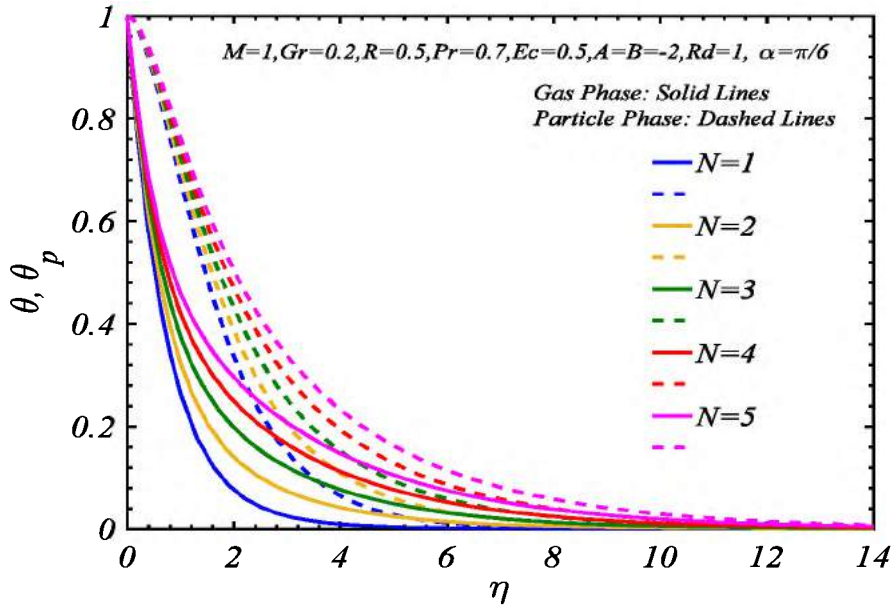

Figure 9.9: Variation of θ, θ_p versus *N*.

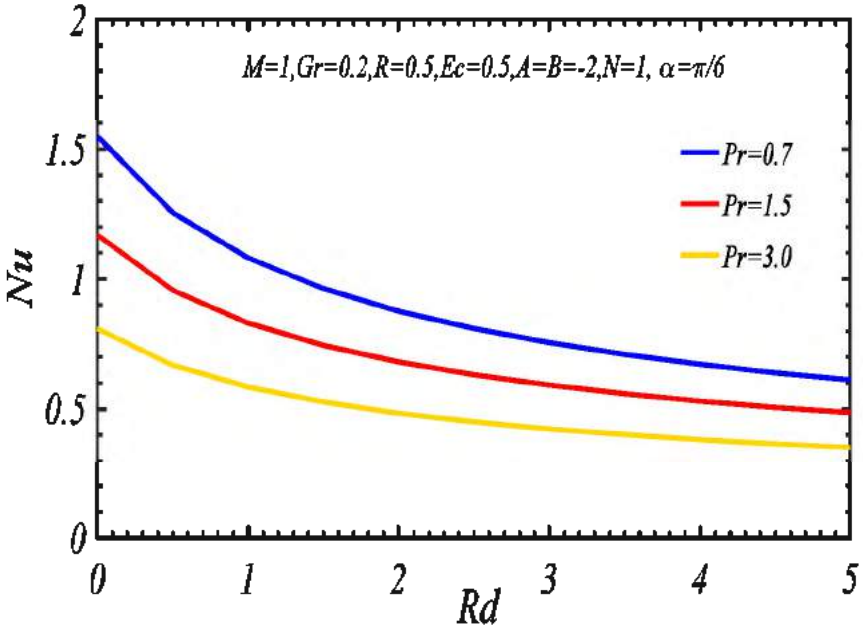

Figure 9.10: Influence of *Rd* on *Nu* for several values of *Pr*.

Chapter 10

Conclusion and Future Work

10.1 Introduction

This chapter recapitulates the key findings of current thesis. Also, we outline some expected directions for future research work.

10.2 Conclusion

The ambition of research work explained in the thesis is to provide the mathematical modeling and numerical computation of hydromagnetic transport of single material nanoparticles, hybrid nanoparticles and solid particles in viscous fluids. For mathematical formulation of nanofluid Buongiorno's model, Tiwari-Das model and two phase model have been incorporated. Fluid flow takes place through various realistic configurations like stretching cylinder, concentric cylinders and inclined plane. Several flow and heat transfer features like mixed convection, thermal radiation, viscous dissipation, Joule heating and porosity are considered. The reduced set of nonlinear equations are converted to system of first order equations which are tackled by employing Runge-Kutta-Fehlberg fourth-fifth order (RKF45) numerical integration scheme along with shooting algorithm and "Bvph 2.0" homotopy based Mathematica package. As the first two chapters are preliminary study, which focused on the introduction, research background, motivation, methodology, outlines, literature review, governing equations and dimensionless numbers. From chapter three and onward the main published and submitted work is reported. The chapter wise conclusion is written as follows:

Chapter 3 presents the influence of thermal radiation and convective heating on hydromagnetic transport of Alumina nanoparticles in ethylene glycol base fluid over linearly stretching cylinder. Flux model proposed by Rosseland is employed to examine effects of thermal radiation. Effect of electric field is also incorporated. The key findings of this study show that for extremely large Biot number, the convective condition becomes the isothermal condition. By enhancing the Biot number the Nusselt number rises for several values of electric parameter. Skin friction coefficient

enhanced as we increase electric parameter and magnetic parameter. By increasing magnetic parameter the flow profiles fall down while thermal boundary layer grown up. Both the flow and thermal profiles are boosted with the increase in electric parameter.

Chapter 4 is associated with the study of convective-radiative heat transfer and flow analysis of hydromagnetic Alumina-copper/water hybrid nanofluid flow with joule heating and viscous dissipations. Boussinesq's and boundary layer approximations are utilized to formulate governing equations. The main outcomes of this research depict some fantastic impacts. By increasing the impact of magnetic parameter, the velocity profile of hybrid nanofluid reduces while the temperature profile is enhanced. By enhancing convection parameter and curvature parameter both velocity and temperature distributions are enhanced. By increasing curvature parameter, the skin friction coefficients are rises, while opposite trend is seen versus increasing convection parameter. The value of shear stress at wall is found maximum in case of copper/water nanofluid and reduced through hybrid nanoparticles. By enhancing the radiation parameter, convection parameter then the Nusselt number is enhanced, while the reverse behavior is seen by increasing curvature parameter and Eckert number. Convective heat transfer is lowest in case of copper/water nanofluid and is improved by inclusion of hybrid material.

Chapter 5 explores the flow of iron nanoparticles aggregation in water base fluid over a stretching cylinder such that the influences of mixed convection and Joule heating are also account for. The obtained results explain that by enhancing the nanoparticles concentration the velocity profiles are reduced while temperature profiles are enhanced. By improving the backbone length and number of particles in back bone the convective heat transfer rate is improved. When dead end particles are increased, wall shear stress is improved but heat transfer rate is decreased. By enlarging radius of gyration both the skin friction coefficient and heat transfer rate are enhanced.

Chapter 6 deals with the nanofluid flow past stretching cylinder in non-Darcian Forchheimer porous media using Buongiorno's mathematical model. The influences of MHD, Joule heating and thermal radiation are also reflected. The prescribed heat flux (PHF) and prescribed concentration flux (PCF) boundary conditions are incorporated. The main outcomes of the study demonstrate that the velocity field,

temperature field and nanoparticles concentration is increasing function of curvature parameter. The thermal distribution and concentration distribution are boosted when we increase magnetic parameter but velocity field show decreasing trends. The higher values of thermophoretic parameter correspond to higher temperature. The existence of nanoparticles enhances the thermal conductivity of fluid due to which higher values of temperature are achieved. Temperature field and its related boundary layer are increased when we raise the radiation parameter and Eckert number. Here we also observed that the temperature improves rapidly for large radiation parameter as compared to Eckert number. Brownian motion parameter leads to reduce the nanoparticles concentration distribution because nanoparticles concentration is inversely correlated to Brownian motion parameter. The skin-friction coefficients corresponding to increasing magnetic parameter are larger.

Chapter 7 is devoted to the influence of chemical reaction and Arrhenius activation energy on hydromagnetic transport of Non-Newtonian Casson nanofluid flow over a permeable stretching cylinder. The impacts of inclined magnetic field, viscous dissipation, joule heating, suction, Thermophoresis, Brownian motion, are also accounted for. The results shows that by enhancing magnetic parameter, Casson fluid parameter and magnetic field inclination the velocity distribution decreases while temperature and concentration distributions are enhanced. Both temperature and concentration distributions are raised by increasing thermophoretic parameter. By enhancing Brownian motion parameter the temperature distribution increases while concentration distribution is decreased. By raising chemical reaction parameter the nanoparticles concentration distributions declines while the contrasting trend is perceived for activation energy parameter. By enhancing Casson fluid parameter the skin friction coefficient and Sherwood number are decreased while Nusselt number is increased. By increasing magnetic field inclination the skin friction coefficient and Sherwood number are improved while Nusselt number is reduced. By increasing chemical reaction parameter the Sherwood number increases while reverse trend can be visualized for increasing activation energy parameter.

Chapter 8 is reported about the hydromagnetic solid-liquid pulsatile flow through an annulus region between two concentric circular cylinders in porous media. The impact of Joule heating is also taken. The core consequences of this chapter illustrates that the steady and unsteady parts of the velocity distribution of fluid phase and solid

phase decrease by increasing the magnetic parameter as well as porosity parameter. The first and second unsteady parts of temperature distribution of fluid and solid phases increase by increasing magnetic parameter. By increasing porosity parameter the first and second unsteady parts of temperature distribution decrease.

Chapter 9 focuses on the impacts of thermal radiation and magnetic field on boundary layer optically thick dusty gas flow over an inclined plane. The influence of viscous dissipation is also. The main results of current study addresses that by increasing gas-particles interaction parameter and Grashof number the velocity profile for gas phase and dust phase enhances. By enhancing magnetic number and inclination of plane the velocity profile for gas phase and dust phase decreases. The temperature profiles for gas phase and dust phase are enhanced when we increase radiation number, Eckert number and Prandtl number.

10.3 Future Work

The flow phenomenon studied in this thesis provides useful information's. The characteristics and advantages of current exploration have been evidently illustrated by its applications to altered practical situations. However, there are still many issues to resolve. In order to get complete prophetic competency for particle transport, we suggest performing research with more complex simulation models and more accurate measurements. Here we present some notions and directions for future work.

Non-Spherical Particles: The investigations in current thesis focused on transport of spherical particles. Our future plane is to extend our work for case of non-spherical particles because particle shape in numerous industrial processes, like catalysis and pyrolysis, is often non-spherical.

Microchannel and Microtube: The realistic configurations incorporated in current study are stretching cylinder, concentric cylinders and inclined plane. Our future plane is to extend our research to microchannel and micro tubes geometries due to their widespread engineering and industrial applications.

Magnetic Particles: In current study, we have considered non-magnetic particles in conducting base fluids. Our future proposal is to extend our work for magnetic

particles due to their attracting medical applications like drug delivery, heat mediators for cancer therapy, magnetic resonance imaging (MRI), hyperthermia and tissue engineering.

Random distribution of particles: In current study, we have chosen uniform distribution of particles dispersed in base fluid. Our future proposal is to extend this work for random distribution of particles which may bring up the Stochastic modeling.

References

[1] Choi, S. U., and Eastman, J. A. (1995). Enhancing thermal conductivity of fluids with nanoparticles (No. ANL/MSD/CP-84938; CONF-951135-29). *Argonne National Lab., IL (United States).*

[2] Tiwari, R. K., and Das, M. K. (2007). Heat transfer augmentation in a two-sided lid-driven differentially heated square cavity utilizing nanofluids. *International Journal of Heat and Mass Transfer*, 50(9-10), 2002-2018.

[3] Buongiorno, J. (2006). Convective transport in nanofluids. *Journal of heat transfer*, 128(3), 240-250.

[4] Eastman, J. A., Choi, U. S., Li, S., Thompson, L. J., and Lee, S. (1996). Enhanced thermal conductivity through the development of nanofluids. *MRS Online Proceedings Library Archive*, 457.

[5] Eastman, J. A., Phillpot, S. R., Choi, S. U. S., and Keblinski, P. (2004). Thermal transport in nanofluids. *Annu. Rev. Mater. Res.*, 34, 219-246.

[6] Das, S. K., Putra, N., Thiesen, P., and Roetzel, W. (2003). Temperature dependence of thermal conductivity enhancement for nanofluids. *Journal of heat transfer*, 125(4), 567-574.

[7] Xuan, Y., and Li, Q. (2003). Investigation on convective heat transfer and flow features of nanofluids. *Journal of Heat transfer*, 125(1), 151-155.

[8] Sundar, L. S., Sharma, K. V., Singh, M. K., and Sousa, A. C. M. (2017). Hybrid nanofluids preparation, thermal properties, heat transfer and friction factor–a review. *Renewable and Sustainable Energy Reviews*, 68, 185-198.

[9] Suresh, S., Venkitaraj, K. P., Selvakumar, P., and Chandrasekar, M. (2011). Synthesis of Al_2O_3–Cu/water hybrid nanofluids using two step method and its thermo physical properties. *Colloids and Surfaces A: Physicochemical and Engineering Aspects*, 388(1-3), 41-48.

[10] Suresh, S., Venkitaraj, K. P., Selvakumar, P., and Chandrasekar, M. (2012). Effect of Al_2O_3–Cu/water hybrid nanofluid in heat transfer. *Experimental Thermal and Fluid Science*, 38, 54-60.

[11] Suresh, S., Venkitaraj, K. P., Hameed, M. S., and Sarangan, J. (2014). Turbulent heat transfer and pressure drop characteristics of dilute water based

Al_2O_3–Cu hybrid nanofluids. *Journal of nanoscience and nanotechnology*, 14(3), 2563-2572.

[12] Prakash, M., and Devi, S. (2016). Hydromagnetic hybrid Al_2O_3-Cu/water nanofluid flow over a slendering stretching sheet with prescribed surface temperature. *Asian Journal of Research in Social Sciences and Humanities*, 6(9), 1921-1936.

[13] Takabi, B., and Shokouhmand, H. (2015). Effects of Al_2O_3–Cu/water hybrid nanofluid on heat transfer and flow characteristics in turbulent regime. *International Journal of Modern Physics C*, 26(04), 1550047.

[14] Esfe, M. H., Alirezaie, A., and Rejvani, M. (2017). An applicable study on the thermal conductivity of SWCNT-MgO hybrid nanofluid and price-performance analysis for energy management. *Applied Thermal Engineering*, 111, 1202-1210.

[15] Minea, A. A. (2017). Hybrid nanofluids based on Al_2O_3, TiO_2 and SiO_2: numerical evaluation of different approaches. *International Journal of Heat and Mass Transfer*, 104, 852-860.

[16] Taylor-Pashow, K. M., Della Rocca, J., Huxford, R. C., and Lin, W. (2010). Hybrid nanomaterials for biomedical applications. *Chemical Communications*, 46(32), 5832-5849.

[17] Zareie, A., and Akbari, M. (2017). Hybrid nanoparticles effects on rheological behavior of water-EG coolant under different temperatures: an experimental study. *Journal of Molecular Liquids*, 230, 408-414.

[18] Rostamian, S. H., Biglari, M., Saedodin, S., and Esfe, M. H. (2017). An inspection of thermal conductivity of CuO-SWCNTs hybrid nanofluid versus temperature and concentration using experimental data, ANN modeling and new correlation. *Journal of Molecular Liquids*, 231, 364-369.

[19] Gregory, J. O. H. N. (1996). Particle aggregation: modeling and measurement. *Nanoparticles in Solids and Solutions*, 18, 203.

[20] Meakin, P. (1987). Fractal aggregates. *Advances in Colloid and Interface science*, 28, 249-331.

[21] Jullien, R., and Botet, R. (1987). Aggregation and fractal aggregates. *Ann. Telecomm*, 41, 343-short.

[22] Saffman, P. G. (1962). On the stability of laminar flow of a dusty gas. *Journal of fluid mechanics*, 13(1), 120-128.

[23] Marble, F. E. (1963). Dynamics of a gas containing small solid particles. *Proceedings of the 5th AGARD combustion and propulsion colloquium Pergamon press Oxford*, 175-215.

[24] Michael, D. H., and Miller, D. A. (1966). Plane parallel flow of a dusty gas. *Mathematika*, 13(1), 97-109.

[25] Michael, D. H., and Norey, P. W. (1968). The laminar flow of a dusty gas between two rotating cylinders. *The Quarterly Journal of Mechanics and Applied Mathematics*, 21(3), 375-388.

[26] Rao, P. S. S. (1969). Unsteady flow of a dusty viscous liquid through circular cylinder. *Defence Science Journal*, 19(2), 135-138.

[27] Soo, S. L. (1965). Dynamics of multiphase flow systems. *Industrial and Engineering Chemistry Fundamentals*, 4(4), 426-433.

[28] Otterman, B., and Lee, S. L. (1969). Particle migrations in laminar mixing of a suspension with a clean fluid. *Zeitschrift für angewandte Mathematik und Physik ZAMP*, 20(5), 730-749.

[29] Baral, M. C. (1968). Plane parallel flow of a conducting dusty gas. *Journal of the Physical Society of Japan*, *25*(6), 1701-1702.

[30] Peddieson, J. (1976). Some unsteady parallel flows of particulate suspensions. *Applied Scientific Research*, 32(3), 239-268.

[31] Healy, J. V., & Yang, H. T. (1970). Oscillating two-phase channel flows. *Zeitschrift fur angewandte Mathematik und Physik ZAMP*, *21*(3), 454-467.

[32] Kumar, S. K., and Sarma, L. V. K. V. (1991). Fluid-particle suspension flow past a stretching sheet. *International Journal of Engineering Science*, 29(1), 123-132.

[33] Shampine, L. F., Gladwell, I., Shampine, L., and Thompson, S. (2003). Solving ODEs with matlab. *Cambridge university press*.

[34] Shampine, L. F., Kierzenka, J., and Reichelt, M. W. (2000). Solving boundary value problems for ordinary differential equations in MATLAB with bvp4c. *Tutorial notes*, 2000, 1-27.

[35] S. J. Liao, Proposed homotopy analysis techniques for the solution of nonlinear problem, PhD dissertation, Shanghai Jiao Tong University, (1992).

[36] S. Sen, Topology and geometry for physicists, Florida: Academic Press, (1983).

[37] S. J. Liao, An approximate solution technique which does not depend upon small parameters (Part2): an application in fluid mechanics, *International Journal of Non-Linear Mechanics*, 32 (1997) 815–22.

[38] Liao, S. (2013). Advances in the homotopy analysis method. *World Scientific.*

[39] Lee, S., Choi, S. S., Li, S. A., and Eastman, J. A. (1999). Measuring thermal conductivity of fluids containing oxide nanoparticles. *Journal of Heat transfer*, 121(2), 280-289.

[40] Keblinski, P., Phillpot, S. R., Choi, S. U. S., and Eastman, J. A. (2002). Mechanisms of heat flow in suspensions of nano-sized particles (nanofluids). *International journal of heat and mass transfer*, 45(4), 855-863.

[41] Khaled, A. R., and Vafai, K. (2005). Heat transfer enhancement through control of thermal dispersion effects. *International Journal of Heat and Mass Transfer*, 48(11), 2172-2185.

[42] Khanafer, K., Vafai, K., and Lightstone, M. (2003). Buoyancy-driven heat transfer enhancement in a two-dimensional enclosure utilizing nanofluids. *International journal of heat and mass transfer*, 46(19), 3639-3653.

[43] Kim, J., Kang, Y. T., and Choi, C. K. (2004). Analysis of convective instability and heat transfer characteristics of nanofluids. *Physics of fluids*, 16(7), 2395-2401.

[44] Koo, J., and Kleinstreuer, C. (2004). A new thermal conductivity model for nanofluids. *Journal of Nanoparticle Research*, 6(6), 577-588.

[45] Koo, J., and Kleinstreuer, C. (2005). Laminar nanofluid flow in microheat-sinks. *International Journal of Heat and Mass Transfer*, 48(13), 2652-2661.

[46] Turkyilmazoglu, M. (2014). Nanofluid flow and heat transfer due to a rotating disk. *Computers and Fluids*, 94, 139-146.

[47] Sheikholeslami, M., Bandpy, M. G., Ellahi, R., Hassan, M., and Soleimani, S. (2014). Effects of MHD on Cu–water nanofluid flow and heat transfer by means of CVFEM. *Journal of Magnetism and Magnetic Materials*, 349, 188-200.

[48] Mabood, F., Khan, W. A., and Ismail, A. M. (2015). MHD boundary layer flow and heat transfer of nanofluids over a nonlinear stretching sheet: a numerical study. *Journal of Magnetism and Magnetic Materials*, 374, 569-576.

[49] Rashidi, M. M., Abelman, S., and Mehr, N. F. (2013). Entropy generation in steady MHD flow due to a rotating porous disk in a nanofluid. *International Journal of Heat and Mass Transfer*, 62, 515-525.

[50] Hussain, T., Shehzad, S. A., Hayat, T., and Alsaedi, A. (2015). Hydromagnetic flow of third grade nanofluid with viscous dissipation and flux conditions. *AIP Advances*, 5(8), 087169.

[51] Makinde, O. D., and Aziz, A. (2011). Boundary layer flow of a nanofluid past a stretching sheet with a convective boundary condition. *International Journal of Thermal Sciences*, 50(7), 1326-1332.

[52] Mustafaa, M., Hayat, T., and Obaidat, S. (2013). Boundary layer flow of a nanofluid over an exponentially stretching sheet with convective boundary conditions. *International Journal of Numerical Methods for Heat and Fluid Flow*, 23(6), 945-959.

[53] Tien, C. L., and Vafai, K. (1989). Convective and radiative heat transfer in porous media. *In Advances in Applied Mechanics*, 27, 225-281.

[54] Hsu, C. T., and Cheng, P. (1990). Thermal dispersion in a porous medium. *International Journal of Heat and Mass Transfer*, 33(8), 1587-1597.

[55] Nithiarasu, P., Seetharamu, K. N., and Sundararajan, T. (1997). Natural convective heat transfer in a fluid saturated variable porosity medium. *International Journal of Heat and Mass Transfer*, 40(16), 3955-3967.

[56] Sheikholeslami, M. (2015). Effect of uniform suction on nanofluid flow and heat transfer over a cylinder. *Journal of the Brazilian Society of Mechanical Sciences and Engineering*, 37(6), 1623-1633.

[57] Ishak, A., Nazar, R., and Pop, I. (2008). Magnetohydrodynamic (MHD) flow and heat transfer due to a stretching cylinder. *Energy Conversion and Management*, 49(11), 3265-3269.

[58] Si, X., Li, H., Zheng, L., Shen, Y., and Zhang, X. (2017). A mixed convection flow and heat transfer of pseudo-plastic power law nanofluids past a stretching vertical plate. *International Journal of Heat and Mass Transfer*, 105, 350-358.

[59] Sheikholeslami, M. (2017). Numerical simulation of magnetic nanofluid natural convection in porous media. *Physics Letters A*, 381(5), 494-503.

[60] Sheikholeslami, M., and Chamkha, A. J. (2017). Influence of Lorentz forces on nanofluid forced convection considering Marangoni convection. *Journal of Molecular Liquids*, 225, 750-757.

[61] Sheikholeslami, M., and Chamkha, A. J. (2016). Electrohydrodynamic free convection heat transfer of a nanofluid in a semi-annulus enclosure with a sinusoidal wall. *Numerical Heat Transfer, Part A: Applications*, 69(7), 781-793.

[62] Shirvan, K. M., Mamourian, M., Mirzakhanlari, S., Ellahi, R., and Vafai, K. (2017). Numerical investigation and sensitivity analysis of effective parameters on combined heat transfer performance in a porous solar cavity receiver by response surface methodology. *International Journal of Heat and Mass Transfer*, 105, 811-825.

[63] Rashidi, M. M., Abelman, S., and Mehr, N. F. (2013). Entropy generation in steady MHD flow due to a rotating porous disk in a nanofluid. *International Journal of Heat and Mass Transfer*, 62, 515-525.

[64] Umavathi, J. C., Ojjela, O., and Vajravelu, K. (2017). Numerical analysis of natural convective flow and heat transfer of nanofluids in a vertical rectangular duct using Darcy-Forchheimer-Brinkman model. *International Journal of Thermal Sciences*, 111, 511-524.

[65] Beg, O. A., Khan, M. S., Karim, I., Alam, M. M., and Ferdows, M. (2014). Explicit numerical study of unsteady hydromagnetic mixed convective nanofluid flow from an exponentially stretching sheet in porous media. *Applied Nanoscience*, 4(8), 943-957.

[66] Ibanez, G., Lopez, A., Pantoja, J., and Moreira, J. (2016). Entropy generation analysis of a nanofluid flow in MHD porous microchannel with hydrodynamic slip and thermal radiation. *International Journal of Heat and Mass Transfer*, 100, 89-97.

[67] Ellahi, R., Shivanian, E., Abbasbandy, S., and Hayat, T. (2015). Analysis of some magnetohydrodynamic flows of third-order fluid saturating porous space. *Journal of Porous Media*, 18(2).

[68] Shirvan, K. M., Ellahi, R., Mirzakhanlari, S., and Mamourian, M. (2016). Enhancement of heat transfer and heat exchanger effectiveness in a double pipe heat exchanger filled with porous media: numerical simulation and

sensitivity analysis of turbulent fluid flow. *Applied Thermal Engineering*, 109, 761-774.

[69] Momin, G. G. (2013). Experimental investigation of mixed convection with water-Al_2O_3 and hybrid nanofluid in inclined tube for laminar flow. *Int. J. Sci. Technol. Res*, 2, 195-202.

[70] Askari, S., Koolivand, H., Pourkhalil, M., Lotfi, R., and Rashidi, A. (2017). Investigation of Fe_3O_4/Graphene nanohybrid heat transfer properties: *Experimental approach. International Communications in Heat and Mass Transfer*, 87, 30-39.

[71] Mehryan, S. A. M., Kashkooli, F. M., Ghalambaz, M., and Chamkha, A. J. (2017). Free convection of hybrid Al_2O_3-Cu water nanofluid in a differentially heated porous cavity. *Advanced Powder Technology*, 28(9), 2295-2305.

[72] Shahsavar, A., Moradi, M., and Bahiraei, M. (2018). Heat transfer and entropy generation optimization for flow of a non-Newtonian hybrid nanofluid containing coated CNT/Fe_3O_4 nanoparticles in a concentric annulus. *Journal of the Taiwan Institute of Chemical Engineers*, 84, 28-40.

[73] Labib, M. N., Nine, M. J., Afrianto, H., Chung, H., and Jeong, H. (2013). Numerical investigation on effect of base fluids and hybrid nanofluid in forced convective heat transfer. *International Journal of Thermal Sciences*, 71, 163-171.

[74] Yarmand, H., Zulkifli, N. W. B. M., Gharehkhani, S., Shirazi, S. F. S., Alrashed, A. A., Ali, M. A. B., and Kazi, S. N. (2017). Convective heat transfer enhancement with graphene nanoplatelet/platinum hybrid nanofluid. *International Communications in Heat and Mass Transfer*, 88, 120-125.

[75] Das, P. K. (2017). A review based on the effect and mechanism of thermal conductivity of normal nanofluids and hybrid nanofluids. *Journal of Molecular Liquids*, 240, 420-446.

[76] Hussein, A. M. (2017). Thermal performance and thermal properties of hybrid nanofluid laminar flow in a double pipe heat exchanger. *Experimental Thermal and Fluid Science*, 88, 37-45.

[77] Evans, W., Prasher, R., Fish, J., Meakin, P., Phelan, P., and Keblinski, P. (2008). Effect of aggregation and interfacial thermal resistance on thermal

conductivity of nanocomposites and colloidal nanofluids. *International Journal of Heat and Mass Transfer*, 51(5-6), 1431-1438.

[78] Kendall, K., and Kosseva, M. R. (2006). Nanoparticle aggregation influenced by magnetic fields. *Colloids and Surfaces A: Physicochemical and Engineering Aspects*, 286(1-3), 112-116.

[79] Mendelev, V. S., and Ivanov, A. O. (2004). Ferrofluid aggregation in chains under the influence of a magnetic field. *Physical Review E*, 70(5), 051502.

[80] Song, D., Jing, D., Geng, J., and Ren, Y. (2015). A modified aggregation based model for the accurate prediction of particle distribution and viscosity in magnetic nanofluids. *Powder technology*, 283, 561-569.

[81] Wang, B. X., Zhou, L. P., and Peng, X. F. (2003). A fractal model for predicting the effective thermal conductivity of liquid with suspension of nanoparticles. *International Journal of Heat and Mass Transfer*, 46(14), 2665-2672.

[82] Nkurikiyimfura, I., Wang, Y., and Pan, Z. (2013). Effect of chain-like magnetite nanoparticle aggregates on thermal conductivity of magnetic nanofluid in magnetic field. *Experimental Thermal and Fluid Science*, 44, 607-612.

[83] Philip, J., Shima, P. D., and Raj, B. (2007). Enhancement of thermal conductivity in magnetite based nanofluid due to chainlike structures. *Applied physics letters*, 91(20), 203108.

[84] Gharagozloo, P. E., and Goodson, K. E. (2011). Temperature-dependent aggregation and diffusion in nanofluids. *International Journal of Heat and Mass Transfer*, 54(4), 797-806.

[85] Chakrabarti, K. M. (1974). Note on boundary layer in a dusty gas. *AIAA Journal*, 12(8), 1136-1137.1136–1137.

[86] Asmolov, E. S., and Manuilovich, S. V. (1998). Stability of a dusty-gas laminar boundary layer on a flat plate. *Journal of Fluid Mechanics*, 365, 137-170.

[87] Datta, N., and Mishra, S. K. (1982). Boundary layer flow of a dusty fluid over a semi-infinite flat plate. *Acta Mechanica*, 42(1-2), 71-83.

[88] Xie, M. L., Lin, J. Z., and Xing, F. T. (2007). On the hydrodynamic stability of a particle-laden flow in growing flat plate boundary layer. *Journal of Zhejiang University-Science A*, 8(2), 275-284.

[89] Agranat, V. M. (1988). Effect of pressure gradient of friction and heat transfer in a dusty boundary layer. *Fluid Dynamics*, 23(5), 729-732.

[90] Khabazi, N. P., and Sadeghy, K. (2016). Peristaltic transport of solid particles suspended in a viscoplastic fluid: A numerical study. *Journal of Non-Newtonian Fluid Mechanics*, 236, 1-17.

[91] Gad, N. S. (2011). Effect of Hall currents on interaction of pulsatile and peristaltic transport induced flows of a particle–fluid suspension. *Applied Mathematics and Computation*, 217(9), 4313-4320.

[92] Gireesha, B. J., Mahanthesh, B., Manjunatha, P. T., and Gorla, R. S. R. (2015). Numerical solution for hydromagnetic boundary layer flow and heat transfer past a stretching surface embedded in non-Darcy porous medium with fluid-particle suspension. *Journal of the Nigerian Mathematical Society*, 34(3), 267-285.

[93] Fu, X., Yao, Z., and Zhang, X. (2017). Numerical simulation of polygonal particles moving in incompressible viscous fluids. *Particuology*, 31, 140-151.

[94] Agaliotis, E., and Bernal, C. (2017). Modeling and simulation of drag forces of non-spherical particles moving towards a surface in polymer melt flows. *Colloid and Interface Science Communications*, 19, 20-24.

[95] Abbas, Z., and Hasnain, J. (2017). Two-phase magnetoconvection flow of magnetite (Fe3O4) nanoparticles in a horizontal composite porous annulus. *Results in physics*, 7, 574-580.

[96] Bhatti, M. M., and Zeeshan, A. (2016). Study of variable magnetic field and endoscope on peristaltic blood flow of particle-fluid suspension through an annulus. *Biomedical Engineering Letters*, 6(4), 242-249.

[97] Saito, T. (2002). Numerical analysis of dusty-gas flows. *Journal of computational physics*, 176(1), 129-144.

[98] Ramadan, H. M., and Chamkha, A. J. (2000). Analytical solutions for hydromagnetic free convection of a participate suspension from an inclined plate with heat absorption. *International Journal of Fluid Mechanics Research*, 27(2-4).

[99] Chamkha, A. J. (2000). Hydromagnetic flow and heat transfer of a particulate suspension over a Non-Isothermal surface with variable properties. *International Journal of Fluid Mechanics Research*, 27(2-4).

[100] Palani, G., and Ganesan, P. (2007). Heat transfer effects on dusty gas flow past a semi-infinite inclined plate. *Forschung im Ingenieurwesen*, 71(3-4), 223-230.

[101] Khare, R. K., Singh, J. (2011). Magnetohydrodynamic flow of a dusty fluid between two inclined parallel plates. *Journal of International Academy of Physical Sciences*, 15, 7-15.

[102] Ramesh, G. K., Gireesha, B. J., and Bagewadi, C. S. (2012). Heat transfer in MHD dusty boundary layer flow over an inclined stretching sheet with non-uniform heat source/sink. *Advances in Mathematical Physics*, 2012.

[103] Siddiqa, S., Begum, N., and Hossain, M. A. (2017). Compressible dusty gas along a vertical wavy surface. *Applied Mathematics and Computation*, 293, 600-610.

[104] Gireesha, B. J., Mahanthesh, B., Gorla, R. S. R., and Manjunatha, P. T. (2016). Thermal radiation and Hall effects on boundary layer flow past a non-isothermal stretching surface embedded in porous medium with non-uniform heat source/sink and fluid-particle suspension. *Heat and Mass Transfer*, 52(4), 897-911.

[105] Sheikholeslami, M., Ganji, D. D., Javed, M. Y., and Ellahi, R. (2015). Effect of thermal radiation on magnetohydrodynamics nanofluid flow and heat transfer by means of two phase model. *Journal of Magnetism and Magnetic Materials*, 374, 36-43.

[106] Sheikholeslami, M., Ganji, D. D., and Rashidi, M. M. (2015). Ferrofluid flow and heat transfer in a semi annulus enclosure in the presence of magnetic source considering thermal radiation. *Journal of the Taiwan Institute of Chemical Engineers*, 47, 6-17.

[107] Michaelides, E. E. S. (2013). Heat and mass transfer in particulate suspensions. *Springer Science and Business Media*.

[108] Brinkman, H. C. (1952). The viscosity of concentrated suspensions and solutions. *The Journal of Chemical Physics*, 20(4), 571-571.

[109] Ishak, A., Nazar, R., and Pop, I. (2008). Uniform suction/blowing effect on flow and heat transfer due to a stretching cylinder. *Applied Mathematical Modeling*, 32(10), 2059-2066.

[110] Wang, C. Y. (1988). Fluid flow due to a stretching cylinder. *The Physics of fluids*, 31(3), 466-468.

[111] Pandey, A. K., and Kumar, M. (2017). Natural convection and thermal radiation influence on nanofluid flow over a stretching cylinder in a porous medium with viscous dissipation. *Alexandria Engineering Journal*, 56(1), 55-62.

[112] Prasher, R., Phelan, P. E., and Bhattacharya, P. (2006). Effect of aggregation kinetics on the thermal conductivity of nanoscale colloidal solutions (nanofluid). *Nano letters*, *6*(7), 1529-1534.

[113] Nan, C. W., Birringer, R., Clarke, D. R., and Gleiter, H. (1997). Effective thermal conductivity of particulate composites with interfacial thermal resistance. *Journal of Applied Physics*, 81(10), 6692-6699.

[114] Khan, W. A., & Pop, I. (2010). Boundary-layer flow of a nanofluid past a stretching sheet. *International journal of heat and mass transfer*, *53*(11-12), 2477-2483.

[115] Gorla, R. S. R., & Sidawi, I. (1994). Free convection on a vertical stretching surface with suction and blowing. *Applied Scientific Research*, *52*(3), 247-257.

[116] Tam, C. K. (1969). The drag on a cloud of spherical particles in low Reynolds number flow. *Journal of Fluid Mechanics*, 38(3), 537-546.